Department of Electrical and Information Engineering

Electrical and Information Engineering
Ph.D. Program
SSD: ING-INF/02–ELECTROMAGNETIC FIELDS

Final Dissertation

Design and fabrication of resonators to realize wireless, wearable and totally passive sensors

---

by
Niro Giovanni

Supervisors:

Prof. Marco Grande

Prof. Massimo De Vittorio

Dr. Francesco Rizzi

Coordinator of the Ph.D. Program:
Prof. Mario Carpentieri

Cycle XXXV, 01/11/2019-31/01/2023

Department of Electrical and Information Engineering
Electrical and Information Engineering
Ph.D. Program
SSD: ING-INF/02–ELECTROMAGNETIC FIELDS

Final Dissertation

Design and fabrication of resonators to realize wireless, wearable and totally passive sensors

by
Niro Giovanni

Referees:

Prof. Domenico de Ceglia

Prof. Vittorio Ferrari

Supervisors:

Prof. Marco Grande

_____

Prof. Massimo De Vittorio

Dr. Francesco Rizzi

Coordinator of Ph.D Program:

Prof. Mario Carpentieri

_____

Cycle XXXV, 01/11/2019-31/01/2023

![Politecnico di Bari logo] **Politecnico di Bari**

LIBERATORIA PER L'ARCHIVIAZIONE DELLA TESI DI DOTTORATO

Al Magnifico Rettore
del Politecnico di Bari

Il sottoscritto GIOVANNI NIRO nato a San Giovanni Rotondo il 16/10/1994

residente a BARI in via LONIGRO, N7 e-mail GIOVANNI.NIRO@POLIBA.IT

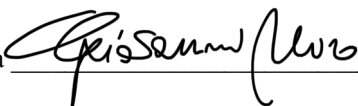iscritto al 3° anno di Corso di Dottorato di Ricerca in Ingegneria Elettrica e dell'informazione ciclo XXV

ed essendo stato ammesso a sostenere l'esame finale con la prevista discussione della tesi dal titolo:

DESIGN AND FABRICATION OF RESONATORS TO REALISE WIRELESS, WEARABLE AND TOTALLY PASSIVE SENSORS

DICHIARA

1) di essere consapevole che, ai sensi del D.P.R. n. 445 del 28.12.2000, le dichiarazioni mendaci, la falsità negli atti e l'uso di atti falsi sono puniti ai sensi del codice penale e delle Leggi speciali in materia, e che nel caso ricorressero dette ipotesi, decade fin dall'inizio e senza necessità di nessuna formalità dai benefici conseguenti al provvedimento emanato sulla base di tali dichiarazioni;
2) di essere iscritto al Corso di Dottorato di ricerca Ingegneria Elettrica e dell'informazione ciclo XXV , corso attivato ai sensi del "*Regolamento dei Corsi di Dottorato di ricerca del Politecnico di Bari*", emanato con D.R. n.286 del 01.07.2013;
3) di essere pienamente a conoscenza delle disposizioni contenute nel predetto Regolamento in merito alla procedura di deposito, pubblicazione e autoarchiviazione della tesi di dottorato nell'Archivio Istituzionale ad accesso aperto alla letteratura scientifica;
4) di essere consapevole che attraverso l'autoarchiviazione delle tesi nell'Archivio Istituzionale ad accesso aperto alla letteratura scientifica del Politecnico di Bari (IRIS-POLIBA), l'Ateneo archivierà e renderà consultabile in rete (nel rispetto della Policy di Ateneo di cui al D.R. 642 del 13.11.2015) il testo completo della tesi di dottorato, fatta salva la possibilità di sottoscrizione di apposite licenze per le relative condizioni di utilizzo (di cui al sito http://www.creativecommons.it/Licenze), e fatte salve, altresì, le eventuali esigenze di "embargo", legate a strette considerazioni sulla tutelabilità e sfruttamento industriale/commerciale dei contenuti della tesi, da rappresentarsi mediante compilazione e sottoscrizione del modulo in calce (Richiesta di embargo);
5) che la tesi da depositare in IRIS-POLIBA, in formato digitale (PDF/A) sarà del tutto identica a quelle **consegnate**/inviate/da inviarsi ai componenti della commissione per l'esame finale e a qualsiasi altra copia depositata presso gli Uffici del Politecnico di Bari in forma cartacea o digitale, ovvero a quella da discutere in sede di esame finale, a quella da depositare, a cura dell'Ateneo, presso le Biblioteche Nazionali Centrali di Roma e Firenze e presso tutti gli Uffici competenti per legge al momento del deposito stesso, e che di conseguenza va esclusa qualsiasi responsabilità del Politecnico di Bari per quanto riguarda eventuali errori, imprecisioni o omissioni nei contenuti della tesi;
6) che il contenuto e l'organizzazione della tesi è opera originale realizzata dal sottoscritto e non compromette in alcun modo i diritti di terzi, ivi compresi quelli relativi alla sicurezza dei dati personali; che pertanto il Politecnico di Bari ed i suoi funzionari sono in ogni caso esenti da responsabilità di qualsivoglia natura: civile, amministrativa e penale e saranno dal sottoscritto tenuti indenni da qualsiasi richiesta o rivendicazione da parte di terzi;
7) che il contenuto della tesi non infrange in alcun modo il diritto d'Autore né gli obblighi connessi alla salvaguardia di diritti morali od economici di altri autori o di altri aventi diritto, sia per testi, immagini, foto, tabelle, o altre parti di cui la tesi è composta.
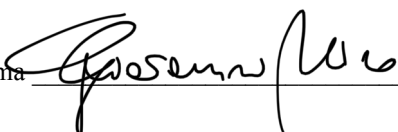
Luogo e data BARI, 20/03/2023   Firma _____

Il/La sottoscritto, con l'autoarchiviazione della propria tesi di dottorato nell'Archivio Istituzionale ad accesso aperto del Politecnico di Bari (POLIBA-IRIS), pur mantenendo su di essa tutti i diritti d'autore, morali ed economici, ai sensi della normativa vigente (Legge 633/1941 e ss.mm.ii.),

CONCEDE

- al Politecnico di Bari il permesso di trasferire l'opera su qualsiasi supporto e di convertirla in qualsiasi formato al fine di una corretta conservazione nel tempo. Il Politecnico di Bari garantisce che non verrà effettuata alcuna modifica al contenuto e alla struttura dell'opera.
- al Politecnico di Bari la possibilità di riprodurre l'opera in più di una copia per fini di sicurezza, back-up e conservazione.

Luogo e data _ BARI, 20/03/2023   Firma _____

Contents

List of Abbreviations

Ag: ....Silver
Al: ....Aluminium
AlN: ....Aluminium Nitride
Au: ....Gold
BAW: ....Bulk Acoustic Wave
BNC: ....Bayonet Neill–Concelman
BW: .... BandWidth
C-CSSR: ....Complementary Split Ring Resonator
Cu: ....Copper
CVD: ....Chemical Vapor Deposition
DC: .... Direct Current
DR: .... Dielectric Resonators
ECA: .... Equivalent Circuit Analysis
EM: .... ElectroMagnetic
ETCs: .... Electrochemical Twin Channels
FAPS: .... FluoroAlcohol PolySiloxanes
FBAR: ....thin-Film Bulk Acoustic wave Resonator
FDTD: .... Finite Difference Time Domain
FEA: .... Finite Element Analysis
FEM: .... Finite Element Method
FEs: ....Finite Elements
FoM: .... Figure of Merit
GA: .... Genetic Algorithm
GSG: ....Ground Signal Ground
HA: .... Hyaluronic Acid
Hg: ....Mercury
ICP-RIE: .... Inductive Coupled Plasma Reactive Ion Etching
IDTs: ....InterDigiTates
IoT: ....Internet of Things
IPA:...IsoPropAnole
ISF:.. Interstitial Fluids
LFE:.. Laterally Field Excited
LiTaO$_3$:.. Lithium Tantalate
LN:.. Lithium Niobate
LOR: ....Lift-Off Resist
LUT: ....Liquid Under Test
MA: .... Mask Aligner
MEMS: ....Micro-Electro-Mechanical System
MGrEs: .... Microconformal Graphene Electrodes
Mo: ....Molybdenum
MoM: ....Method of Momentum
NF: ....Near Field
OOB: .... Out Of Band

P.D.F.: ....Probability Density Function

PCBs: .... Printed Circui Boards

PDMS: .... PolyDiMethylSiloxane

PEC: .... PolyethilEne Carbontate

PEN: .... PolyethilenE Naphthalate

PET: .... PolyEthilene Terephthalate

PHM: .... PolyHydroxyethyl-Methacrylate

PI: .... PolyImide

PIFA: ....Planar Inverted-F Antenna

PMLs: .... Perfect Matched Layers

PMMA: ....Polymethylmethacrylate

PPI: ....Pulse Per Inch

Pt: ....Platinum

PVD: .... Physical Vapor Deposition

RF: ....Radio Frequencies

RFID: ....Radio Frequency Identification

SAR: ....Specific Absorption Rate

SAW: ....Surface Acoustic Wave

SEM: ....Scanning Electron Microscope

SiO$_2$: ....Silicon Oxide

SMA: .... SubMiniature version A

SMRs: .... Solid Mounted Resonators

SRR: ....Split Ring Resonator

S-SRR: ....Square Split Ring Resonator

TL: ....Transmission Line

UHF: .... Ultra High Frequency

UV: ....Ultra Violet

VNA: ....Vector Network Analyzer

ZnO: ....Zinc Oxide

Introduction

During the recent years, the technology behind sensors has taken enormous steps in developing new systems able to unobtrusively monitor our lives. Indeed, thanks to flexible electronics, the brittle and rigid chips can be replaced with a new generation of devices able to conformal adapt their shape to the human body and to improve comfort.

In parallel, the Internet of Things (IoT) has become one of the major markets; and the prevalence of traffic in telecommunication networks is now produced by the objects around us. Smart sensors are gaining interest even more in modern networks where a multitude of standards for their connection is expanding the umbrellas of 5G and 6G. In this scenario, a crucial step forward can be the use of wireless nodes. This trend has led to a new generation of devices and microsystems, composed by microprocessors and/or radio frequency circuitry, to send data remotely, at the cost of larger footprints and higher power consumption.

Flexible radiofrequency resonators present some key features necessary for the development of wearable, wireless, and low consuming non-invasive sensing platforms. These devices combine the advantages of flexibility and wearability with remote sensing capabilities. Indeed, working in the Radio Frequencies (RF), they can be directly interrogated by travelling electromagnetic fields emitted through antennas, avoiding additional circuitry for the transmission of data. Moreover, several resonators can be integrated into a single chip, enhancing the sensing capabilities and increasing the performance of the systems. In the literature, several flexible radiofrequency resonators are reported, with microstrip and Micro-Electro-Mechanical System (MEMS) technologies among the most suitable for integration on flexible materials.

MEMS are one of the most interesting categories of microwave resonators. In this kind of devices, the ElectroMagnetic (EM) wave perturbations are converted into mechanical perturbations. Shortening of mechanical wavelength leads to very small resonating areas working in the Ultra High Frequency (UHF) range, with footprints of the order of tens of micrometres. The main drawback of this strategy is related to its complicated fabrication processes, which are not compatible with standard microfabrication processes when flexible substrates are considered.

Differently, microstrip resonators can be fabricated in a very straightforward manner even on flexible materials with big yields and cost-effective processes, exploiting 3D printing techniques. The performance of microstrip resonators is comparable with MEMS at the cost of larger footprints; therefore, the working frequency of these resonators has to be high enough to be miniaturized and allow the development of small sensing platforms.

In a nutshell, flexible microwave resonators represent a disruptive technology in the quest for smart and wearable sensor nodes. Although their high potential, there are several challenges to be addressed. In this thesis, the design and the fabrication of flexible microwave resonators and antennas have been exploited and investigated. The theory and the fabrication techniques behind the development of a flexible RF-resonator are treated. The development of two classes of resonators has been reported. More in specific, thin-film flexible MEMS resonators have been designed through Finite Element Method (FEM) models and by an innovative approach exploiting calibration procedures. Experimental data and fabrication tolerances can be included in the estimation of the resonant frequency of the resonator using Monte Carlo simulations with a much lower computational cost than previous simulations. The design approach has been validated through the fabrication of a standard silicon thin-Film Bulk Acoustic wave Resonator (FBAR). Moreover, the same technique has been applied to the development of passband FBAR filters. This possibility has been validated through the reverse engineering of an existing device. Thanks to this design approach, two generations of MEMS resonators have been fabricated: the first by a more straightforward process, grown directly on a flexible polyimide substrate layer and tested as a gravimetric sensor; the second one, characterized by a suspended structure, exploiting a flexible Kapton substrate and suspended by a polymeric membrane. In this case, several resonators working in parallel have been integrated into a combined device.

After the development of MEMS resonators, a microstrip-based Combined Complementary Split Ring Resonator (C-CSRR) has been produced. The device is composed of two identical CSRRs and its design has been performed using the Finite Difference Time Domain (FDTD) method. Then the fabrication has been performed using a multi-material 3D printer on a 200 µm Kapton substrate. The sensor demonstrates high sensitivity to water droplets and temperature when

immersed in liquids and it can be exploited for skin sensing or ingestible applications.

Finally, the development of flexible antennas has been performed producing two different devices. The first is a patch multilayer antenna based on a polyethylene naphthalate substrate whose radiation properties have been enhanced through the integration with a Split Ring Resonator (SRR) in between the top and the ground planes. The second proposed antenna has been a Planar Inverted-F Antenna (PIFA) based on the same substrate, e.g. PolyethilenE Naphthalate (PEN), but characterised by a planar geometry and a shorting pin between the positive and the negative arms, which reduce its electrical length. Both the antennas have been designed using FDTD models and fabricated exploiting a multimaterial 3D printer.

Chapter 1- State of the art

Electronics are spreading deeply into our daily lives and moving from benchtop instruments to a multitude of portable objects, i.e., IoT nodes [1].

IoT nodes are characterized by sensing and communication capabilities. Since the maturity of these technologies, their number is exponentially growing.

Figures 1.1 and 1.2 illustrate a snapshot of the grown of the IoT industry. The number of IoT devices is forecast to increase from 13 to almost 30 billion in 2030 with a market value of 1110 billion dollars.
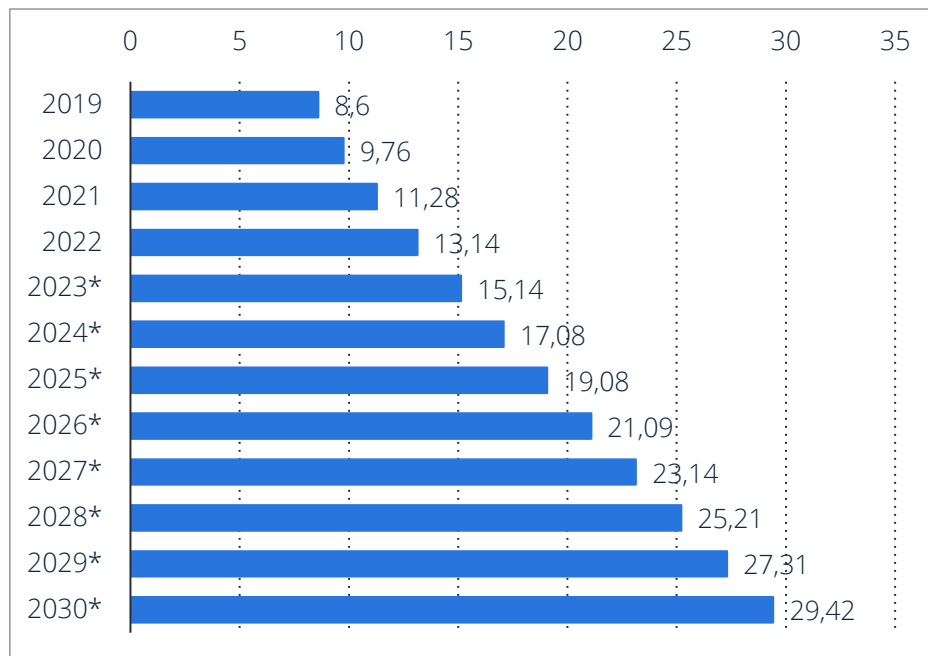
Figure 1.1: Number of IoT-connected devices worldwide from 2019 with forecasts to 2030.
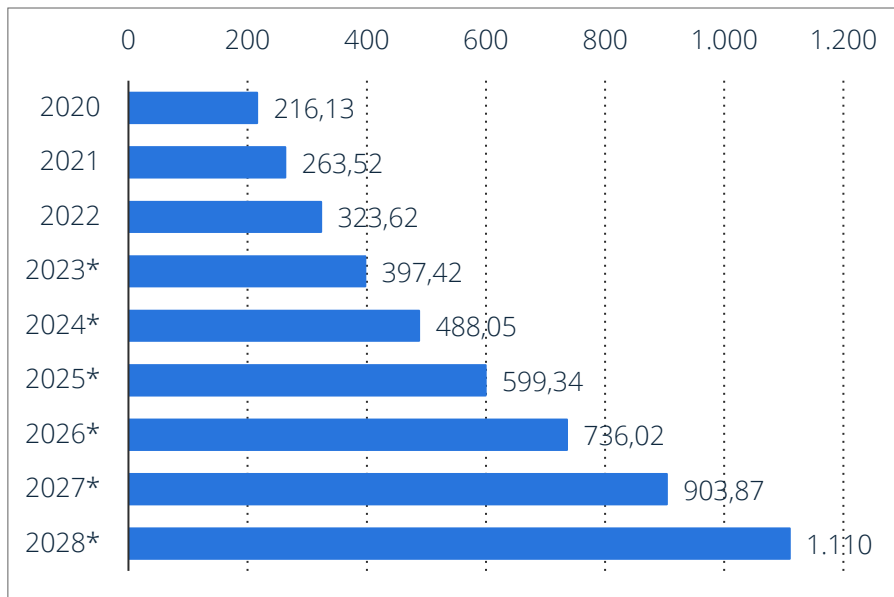
Figure 1.2: Market size of IoT worldwide from 2020 with forecast to 2028.

The massive profusion of IoT has reached new frontiers that move away from monitoring objects and onto our bodies with wearable and ingestible applications, realizing smart and connected healthcare systems.

1.1- Flexible sensors

The electronic based on flexible substrate is the new frontier regarding smart sensor nodes. Thanks to the use of stretchable and bendable materials, these devices can handle challenges not accomplishable using rigid and brittle materials such as silicon [2]–[4]. Firstly, these substrates are thinner and more lightweight than rigid ones, reducing the form factor and the footprints of the sensing nodes. Secondly, their bendability allows the devices to follow the curvature of the human body, increasing the wearability of the systems. Thirdly, their high stretchability ensures high robustness to external strains. In this scenario, the development of flexible IoT nodes can enable a new generation of sensing platforms with outlooks for continuous monitoring with high comfort and low invasiveness [4].

In the literature, several examples of flexible sensing nodes are reported. Reference [5] details a skin-like biosensor for non-invasive blood glucose monitoring. The working principle and the structure of the sensor are shown in Figure 1.3.
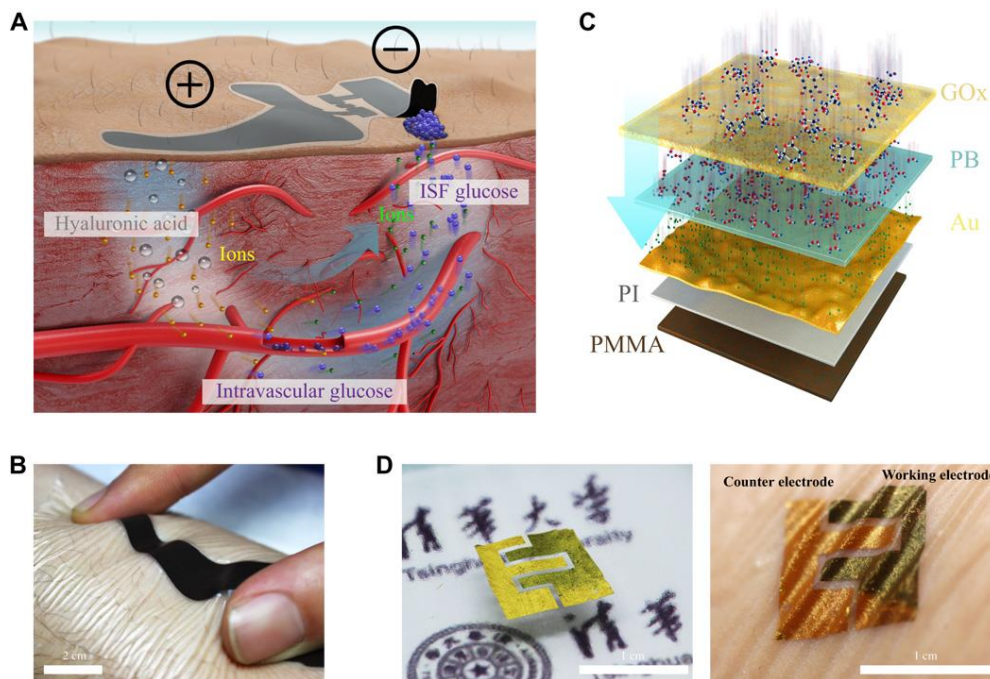
Figure 1.3: (a) Schematic of the ETCs, (b) stretching of the sensor attached to the skin, (c) breakdown of the ultrathin skin-like biosensor multilayers. (d) Paper battery in free-standing and attached to the skin configurations [5].

The system is powered by a biocompatible paper battery. The role of the battery is to generate subcutaneous Electrochemical Twin Channels (ETCs). The anode channel is established through Hyaluronic Acid (HA), while the cathode is generated by the glucose penetrations into the Interstitial Fluids (ISF). The HA molecules are pushed into the vessels from the positive potential of the battery. A higher concentration of the HA increases the pressure into the vessels, promoting intravascular blood glucose refiltration at the arterial ends and reducing the reabsorption at the venous ends. As a result, the concentration of intravascular blood glucose is increased at the skin surface and can be measured by the sensor. The use of a 1.6 μm-thick PolyImide (PI) substrate not only ensure a low impact factor of the sensor but enables the conformity of the device to the skin increasing the sensitivity (130.4 μA/mM).

Another example of a flexible sensor is detailed in Reference [6]. The system is a flexible, tunable, and ultrasensitive capacitive pressure sensor. The sensor is composed of Microconformal Graphene Electrodes (MGrEs) transferred to a PolyethilEne Carbonate (PEC) substrate through an Ultra Violet (UV)-A adhesion layer. By sandwiching a PolyDiMethylSiloxane (PDMS) dielectric layer between the top MGrE and the bottom electrode, the authors obtained a capacitive pressure

sensor with high sensitivity, fast response speed, ultralow detection limit, tunable sensitivity, high flexibility, and high stability.

Besides lightness and wearability of the substrate, the minimization of the footprint of the sensors assumes a crucial role. Smaller footprints allow the development of nodes formed of arrays of sensors able to monitor a multitude of physiological parameters. Moreover, the integration of these arrays with radio frequencies and wireless transmissions can have disruptive consequences making the data of these nodes available without cables and connectors [7], [8]. In the commonly adopted approach, the signal of the sensor is converted in the radiofrequency range for the wireless transmission to an external reader (up-conversion). In Reference [9], a fully integrated wearable and wireless sensor array for multiplexed *in-situ* perspiration analysis is detailed. The array is composed of several sensing technologies and can simultaneously and selectively measure sweat metabolites (such as glucose and lactate) and electrolytes (such as sodium and potassium ions), as well as the skin temperature (used also to calibrate the response of the sensors). As it can be noted from Figure 1.4, although the sensor shows a very light and unobtrusive profile (see Figure 1.4b), the electronic for the wireless transmission is still bulky (see Figures 1.4a and 1.4c).
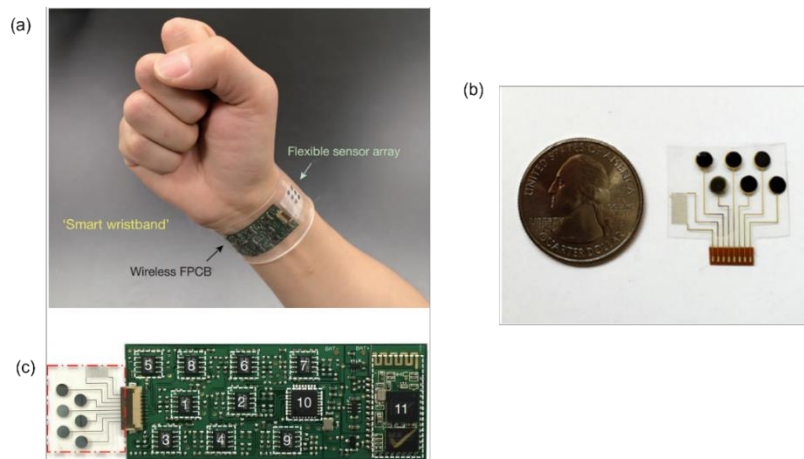
Figure 1.4: a) Wearable sensing system, b) wearable and flexible sensor array, c) array with integrated electronics for wireless transmission [9].

RF sensors produce as output a radio frequency signal which can be easily sent to the reader without further operations through the use of antennas. This strategy

drastically reduces the necessity of electronics at the sensor side enabling the shrinking of the footprint and weight of the whole sensing system [7].

1.2- Microwave resonators

The most exploited microwave devices to build RF sensors are resonators. A resonator is a device having a well-defined structure tailored to confine an electromagnetic signal (as a standing-wave) with a fixed frequency. Resonators are characterized by several parameters extrapolated by a scattering matrix description, expressing the amount of reflected and transmitted powers. The main parameter is the resonant frequency. The frequency of the standing wave changes accordingly to the geometry but also with the external condition of the resonating region. Therefore, important information can be extrapolated by resonant frequency changes. In the scattering matrix description of a one-port resonator, the exciting power is transferred to the load at the resonant frequency causing a dip in the scattering parameter S_{11}. While two-ports resonators, can be characterized through the S_{21} or S_{12} [10] analysis.

A further important parameter is the Q-factor, representing the efficiency of the confinement of the EM-wave. The Q-factor can be evaluated using the scattering matrix and Equation 1.1,

$$Q = \frac{f}{\Delta f} \tag{1.1}$$

where Δf is the 3dB bandwidth of the scattering parameters S_{11} or S_{21} in one- or two-ports resonators, respectively.

Differently, the Q-factor can be expressed as the ratio between the stored and the dissipated energy as in Equation 1.2.

$$Q = 2\pi \frac{energy\ stored}{energy\ dissipated\ per\ cycle} \tag{1.2}$$

1.2.1- Dielectric resonators

Microwave resonators can be classified by the way exploited to confine the electromagnetic waves. In Dielectric Resonators (DRs), the resonant

electromagnetic field is confined in a dielectric material layer. Thanks to their high-quality factors combined with small physical sizes, such resonators are widely used as the building block for narrowband filter applications. In addition, the resonant frequency changes accordingly to the dielectric conditions, thereby very sensitive sensors can be achieved. In Reference [11] a dielectric resonator used as a miniature gas sensor is proposed. The resonant frequency is set at 27 GHz and the sensitivity of the sensor has been enhanced through the deposition of two functional materials, PolyHydroxyethyl-Methacrylate (PHM) and FluoroAlcohol PolySiloxanes (FAPS). Reference [12] details a dielectric cylindrical cavity resonator equipped with a thin plastic liquid container for non-contact detection of the liquid solution concentration. The resonant frequency is tuned to around 11 GHz. The device presents a small volume of 21 cm^3 and a sensitivity of 0.4 kHz L/mg. Finally, Reference [13] presents a sensor based on a dielectric resonator fed by a slot-coupling mechanism in the ground plane of a microstrip. A small hole has been drilled on the DR surface to expose a Liquid Under Test (LUT) making the resonant frequency of the sensor dependent on its electromagnetic characteristics.

1.2.2- Microstrip resonators

Although their optimal properties, dielectric resonators are 3D structures made of rigid and bulky materials; therefore, they are not suitable for wearable applications. Instead, microstrip resonators are cheaper and suitable for flexible substrate integration. A microstrip Transmission Line (TL) is formed of a signal metal trace on a dielectric substrate and a ground plane. Depending on the application, the microstrip can be vertically oriented, e.g., the substrate is sandwiched between the signal layer and the ground plane; or planar, the signal and the ground traces are on the same face of the dielectric material. Because of their one-layer topology, which allows lower form factors and simpler fabrication processes, planar microstrips are more suitable for wearable and flexible applications.

The commonly used approach in microstrip sensors is related to the fabrication of planar antennas. In these devices, the sensor tag is composed of a radiating antenna excited by an interrogation signal. The sensing antenna collects the interrogation signals travelling through the air and, at the resonance, is received and then absorbed. Therefore, a dip in the received power can be observed at the working

frequency, which varies accordingly to antenna conditions [14]. In Reference [15] water and acid contaminations in oil contactless sensor are detailed. The device is composed of a square spiral antenna formed of a 250 μm-thick polyimide substrate and a gold metallic layer of 35 μm. The sensor operates in two frequency ranges, at 1 GHz analyses the acid content, while at 5.5 GHz detects the water quantity in oil. Another very popular category of microstrip devices are CSRRs which offer one of the highest Q-factors and smallest footprints. CSRR is formed by two concentrical slotted rings separated by a coupling gap. From an electrical point of view, the device can be viewed as an LC circuit whose resonant position f_r is given by equation 1.3:

$$f_r = \frac{1}{2\pi\sqrt{L_0 C_0}} \tag{1.3}$$

where L_0 and C_0 represent the static capacitance and inductance of the structure, respectively.

Any change to the dielectric constant (ε_r) of the material containing the CSRR translates into shifts of the resonant frequency (f_r) from the original value (f_0), therefore very sensitive sensors can be achieved.

The sensitivity of the resonator can be evaluated as reported in Equation 1.4:

$$S = \left(\frac{1}{f_0}\right)\frac{df_r}{d\varepsilon_r} \tag{1.4}$$

Reference [16] explains a low-cost multiple CSRR for the determination of the dielectric constant of liquid samples. The structure is formed of four rings to increase the Q-factor. The resonant frequency is at 2.4 GHz and the LUT flows in a capillary tube travelling into the centre of the resonator, making the system not suitable for wearables. A further approach is detailed in Reference [17] where the LUT is exposed using a microfluidic PDMS channel (see Figure 1.5). The use of this approach increases the interaction between the LUT and the CSRR resulting in a sensitivity of 0.98% on dielectric variations. However, the presence of a multilayer structure formed by the CSRR, and the microfluidic channel increases the complexity of the fabrication since alignment and bonding processes become necessary.
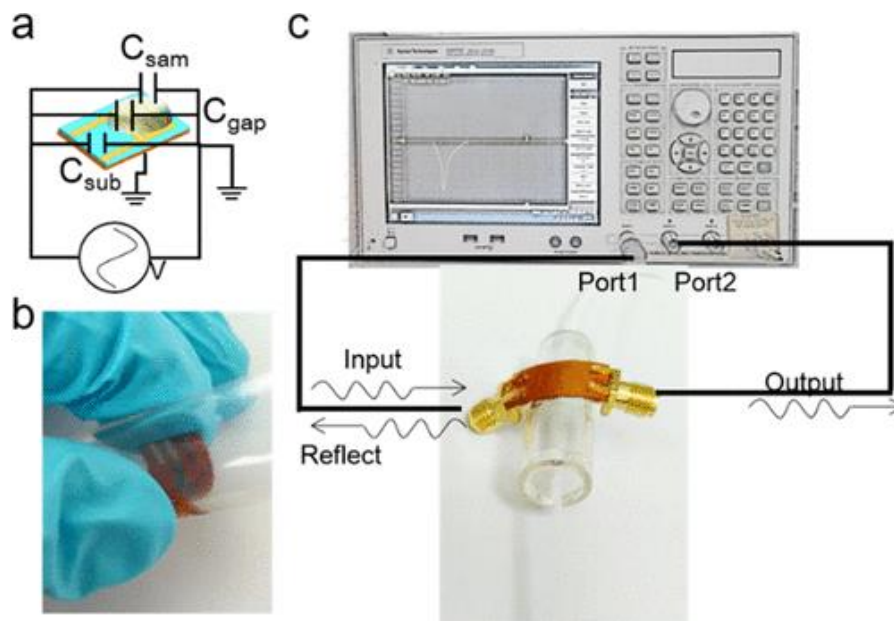
Figure 1.5: (a) Simplified equivalent circuit of the interdigital microstrip sensor loaded with the test sample. (b) Photograph of the flexible and square spiral-based microstrip sensor. (c) Sketch of the measurement setup [17].

Reference [18] proposes another strategy in which the CSRR is immersed in the LUT (see Figure 1.6). The working frequency of the resonator is 8.5 GHz, and the declared air sensitivity is 8% to dielectric variations.

The main issue of microstrip devices regard their huge footprints. Flexible substrates are thin materials with low permittivity, and this demands for transmission lines with larger dimensions, a characteristic which is not matching the requirement of low invasiveness of the new generation of sensors.
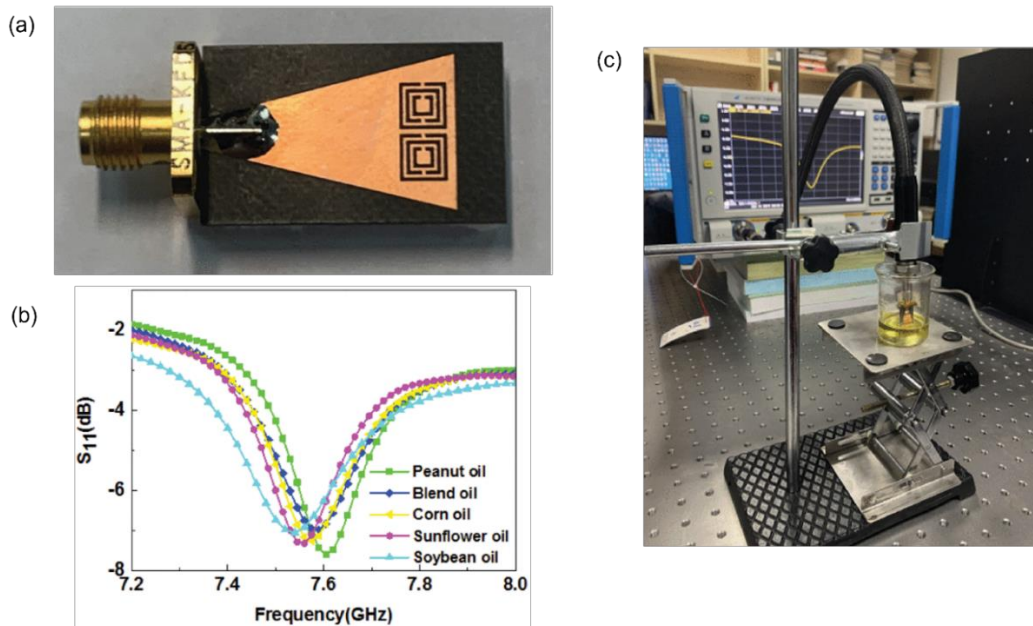
Figure 1.6: CSRR submersible sensor, a) top view of the device, b) Scattering parameter S11 of the resonator, when dipped in different oils, c) Experimental set-up [18].

1.3- Microelectromechanical systems for radio frequency resonators

MEMS have been explored by the sensors industry for decades. The most common MEMS devices are based on piezoelectric materials. Piezoelectricity represents the property of a material to convert electrical stimuli into mechanical deformations (i.e., acoustic waves) and *vice versa*. The transduction between electromagnetic and mechanical domains, becomes extremely interesting if applied to microwave resonators [19]. When in the acoustic domain, the travelling waves become much shorter, with respect the electromagnetic fields. As an example, the electromagnetic wavelength corresponding to 1 GHz is of 30 cm, while in the mechanical domain, considering a phase velocity of 11000 m/s the same frequency presents a wavelength of 11 μm. Indeed, micrometric scaled devices operating in the UHF frequency range can be achieved. Moreover, differently to electromagnetic, acoustic waves can be used for sensing as they are highly sensitive to the medium conditions.

The core of such resonators is the piezoelectric material, which can be analysed in terms of several factors of merit. The electromechanical coupling factor (k_{eff}^2) determines the inter domain energy conversion ratio of the transduction of electromagnetic power to the mechanical domain and *vice versa*. The value of this

parameter is linked to the distance between resonant (f_r) and antiresonant (f_a) frequencies as detailed in Equation 1.5:

$$k_{eff}^2 = \frac{\left(\frac{\pi}{2}\right)^2 (f_a - f_r)}{f_a} \tag{1.5}$$

Higher values are required for wideband applications [20].

The phase velocity of the acoustic wave determines the dimensions of the resonators. In particular, the higher the phase velocity of the acoustic wave, the bigger the mechanical wavelength as detailed in Equation 1.6 [21].

$$f_r = \frac{v_p}{\lambda} \tag{1.6}$$

The quality factor of the material is linked to the losses introduced by the materials. For RF applications. This parameter assumes a crucial role as the losses increase dramatically with the frequency and can be evaluated for the resonant (f_r) and antiresonant (f_a) frequencies considering the derivative of the phase of the impedance with respect to the frequency as shown in Equation 1.7.

$$Q(r|a) = \frac{f}{2}\left\{\frac{d[\angle S_{21}]}{df}\right\}\Big|_{f=f_r|f_a} \tag{1.7}$$

In the literature, several materials have been reported for the scope. Lithium Niobate (LN) has been gaining interest because of its optimal characteristics including very large coupling factors [22] but the deposition of this material with high quality on flexible substrates has not been proven yet. Another interesting material is Zinc Oxide (ZnO). Different from LN, in several works it has been shown that ZnO has been grown efficiently on flexible materials [23]–[25]. This piezoelectric crystal shows a decent electromechanical coupling factor combined with one of the highest piezoelectric coefficients. However, because of its high losses and low phase velocities is not an optimal choice for RF.

Among other piezoelectric materials, Aluminium Nitride (AlN) represents the best choice to combine piezoelectricity and radio frequencies as it presents the highest phase velocities [26], [27]. The growth of AlN thin films on flexible substrates has been demonstrated in several scientific articles [28], [29]. As a consequence, there

is a multitude of works exploiting this material for the fabrication of flexible sensors [28], [30], [31].

Besides the piezoelectric material, another important parameter in the description of RF-MEMS resonators is the nature of the mechanical standing wave. Depending on the kind of acoustic waves there are three main kinds of piezoelectric RF resonators: Surface Acoustic Wave (SAW) [32], Bulk Acoustic Wave (BAW) [33], and FBARs [34], [35].

1.3.1- SAW resonators

SAW resonators exploit the propagation of waves travelling through the surface of the piezoelectric material when its dimensions make it considerable as a semi-infinite medium. The SAW resonator is formed by a piezoelectric material with a couple of InterDigiTates (IDTs) metal electrodes.

The application of an electromagnetic field generates a mechanical wave whose frequency (f_r) depends on the phase velocity of the mechanical wave into the piezoelectric material (v_p) and the pitch of the IDTs (d) [21]. The relationship expressing the working frequency of the resonator is given in Equation 1.8:

$$f_r = \frac{v_p}{2d} \tag{1.8}$$

In the literature, several SAW resonators have been used as sensors having optimal performance [24], [36]–[43]. Moreover, the planar topology of SAWs allows their integration with flexible substrates with optimal results. In Reference [24] a humidity sensor based on a ZnO/glass surface acoustic wave device is presented. The working principle of the sensor is illustrated in Figure 1.7. The glass substrate is a 100 μm-thick Corning Willow. The pitch of the IDTs varies between 20 μm to 12 μm, with working frequencies starting from 130 MHz to 230 MHz. The role of the ZnO is twofold as acting as piezoelectric material and as a sensitive layer since its ability to absorb water molecules. The sensing capabilities have been applied to the breath monitoring with optimal results.
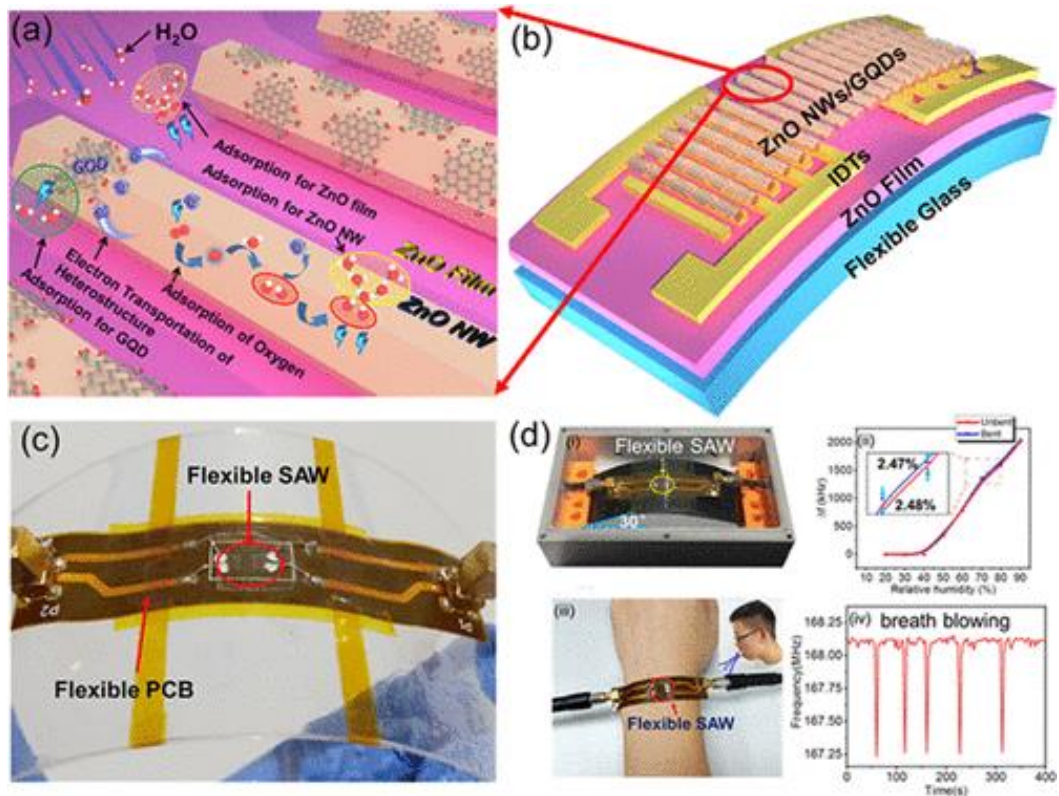
Figure 1.7: (a) Schematic illustration of the adsorption mechanism of H_2O molecules on the composite sensing layer. (b) Top view of the SAW resonator. (c) The device packaged on polyimide flexible printed circuit board and mounted on 1 mm thick poly(ethylene terephthalate) (PET). (d) Monitoring of the breath blowing [24].

In Reference [41] a SAW resonator has been fabricated on a 125 µm-thick PEN substrate and with an AlN piezoelectric layer of 4.5 µm (see Figure 1.8).
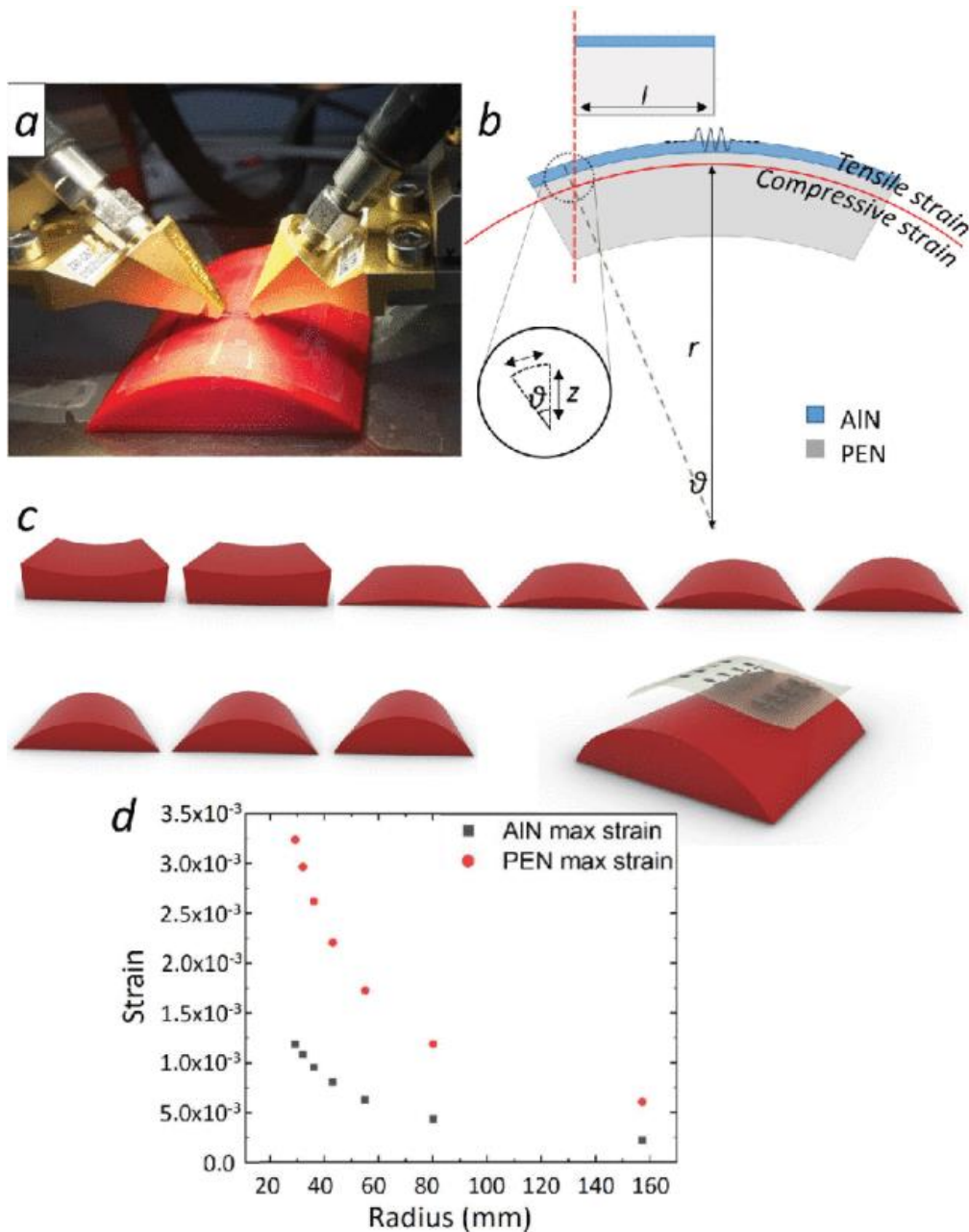
Figure 1.8: (a) Experimental set-up for the tests of the electroacoustic flexion; (b) Sketch of the flexible SAW resonator structure subjected to bending. (c) Sketch of the 3D printed support structures; (d) Trend of the maximum tensile strain in the AlN and PEN materials to the radius of curvature [41].

The resonator works at 180 MHz and 510 MHz, showing a very compact and lightweight profile and high sensitivity to strain deformations.

The main challenge in SAW resonator is represented in the IDTs fabrication. Indeed, the higher the frequency, the smaller the pitch has to be therefore, the climbing of Gigahertz frequencies becomes extremely difficult.

1.3.2- BAW resonators

Different from SAWs, in BAW resonators the piezoelectric layer is sandwiched between metal electrodes. Under the bottom electrode there is a strong acoustic discontinuity, usually obtained by using air-cavities in air-gap [44]–[46], back trench structures [47]–[49], or Bragg Gratings in Solid Mounted Resonators (SMR) [50], [51]. The excited standing wave travels back and forth in the vertical direction of the piezoelectric substrate, where the thinner the piezoelectric layer the higher becomes the working frequency [52].

The design equation of BAW resonators can be reduced to equation 1.3, where d in this case, represents the thickness of the piezoelectric region. It comes that, using thin piezoelectric layers the frequency can be scaled up in a very straightforward way.

BAW resonators have been used for sensing applications in several works [53]–[56]; however, the presence of bulk piezoelectric layers limits the flexibility of the device and makes this choice not optimal in wearable and flexible applications.

Instead, FBARs combine the advantages of SAWs in terms of flexibility and of the BAWs concerning operative frequency range.

1.3.3- Thin Film Bulk Acoustic Wave resonators

FBARs are characterized by a structure like BAWs but exploiting thinner piezoelectric layers allowing the device to work at the Gigahertz range and to be more flexible. Moreover, the thin resonator could be suspended, as a membrane, improving the Q-factor of the resonator. FBARs offer big opportunities for the development of non-invasive and wearable monitoring systems. Although their exceptional features, such as small footprints, high sensitivities, and wireless interrogation protocols, there are several challenges to overcome regarding their design and fabrication.

The material specifications commonly used by simulation methods for the design of these resonators, such as the Equivalent Circuit Analysis (ECA) [57] and the Finite Element Analysis (FEA) [58] can be quite different from the experimental ones. Indeed, they depend on the equipment technology and status, the deposition recipes, environmental conditions, and so on. Furthermore, there is a degree of

uncertainty on the thickness of the thin layers composing the stack because of the fabrication tolerances. This last feature becomes a crucial challenge to overcome as even small variations of the top electrode thickness take to a drift of the resonant frequency because of the mass-loading effect [59]. Moreover, the design equations of these resonators need a specific piezoelectric thickness, and the design procedure loses validity if this value changes. All these drawbacks, if included in the commonly used models, increase the computational time [60].

Besides design issues, the integration of FBARs on flexible substrates is critical because of their suspended structure. This challenge can be addressed by exploiting the flexible substrates as reflecting surfaces for the confinement of the standing waves, avoiding the necessity of membranes. In Reference [61], an FBAR on a PolyEthilene Terephthalate (PET) substrate is presented. The device is formed of a ZnO piezoelectric layer and exploits the PET layer as a reflecting surface to confine the standing wave. The resonator presents a weak resonance at 1.14 GHz and an antiresonant frequency at 1.26 GHz. Another option is detailed in reference [25], where a flexible FBAR on a 9 μm-thick PI polymeric support layer is proposed. The use of polyimide shows an additional benefit. The low acoustic impedance of the polyimide ensures good confinement of the acoustic wave without air gaps in a very straightforward manner. The thicker the polyimide, the better the confinement of the acoustic wave. For a sufficiently thick PI support layer, the resonators can be integrated with optimal results on any substrate. Although showing very straightforward fabrication processes, these approaches ([61],[25]) suffer from very weak resonances and do not apply to sensing applications.

In references [62], [63] a different approach is proposed. In these cases, the FBARs are fabricated on a silicon donor wafer, while, at the same time, the cavities have been patterned on a flexible PET by means of hot embossing. After, the FBARs are detached from the donor wafer using a PDMS doom and are attached to the PET substrate. The obtained resonators show better confinements of the standing waves at the cost of a tricker fabrication protocol requiring two processes and alignment and bonding procedures.
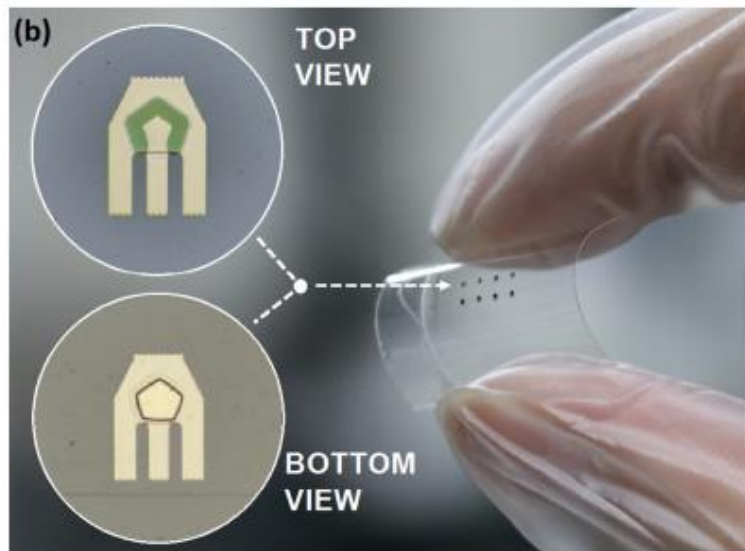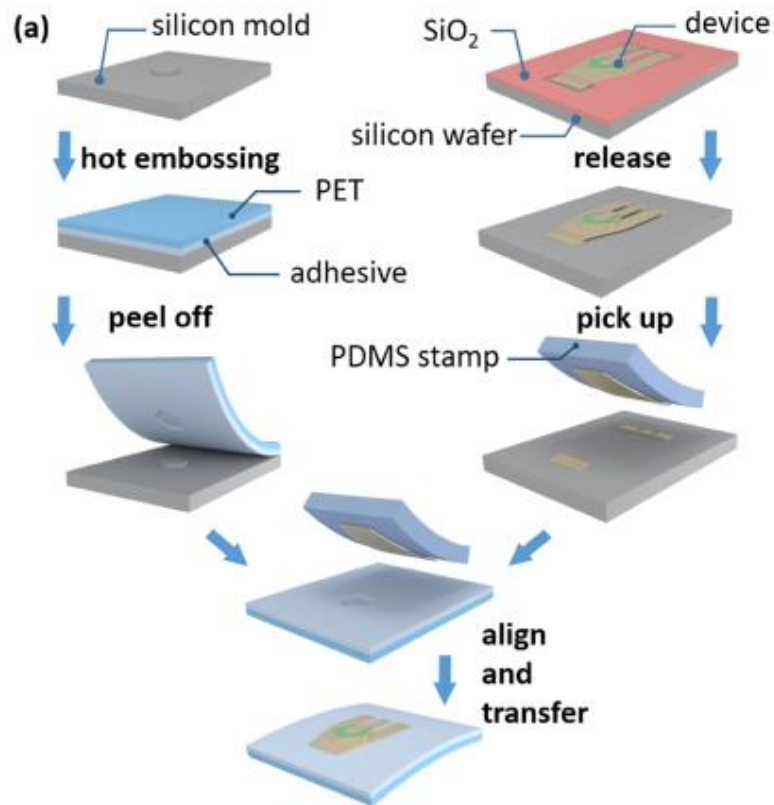
Figure 1.9: (a) Fabrication process of the flexible FBAR, (b) obtained devices [62].

Another strategy for the achievement of optimal performance despite the use of flexible substrates and limiting the fabrication costs is proposed in Reference [64], where a Laterally Field Excited (LFE) resonator is proposed. The device is composed of a Lithium Tantalate (LiTaO$_3$) piezoelectric layer attached to a 150 µm-thick PI substrate.
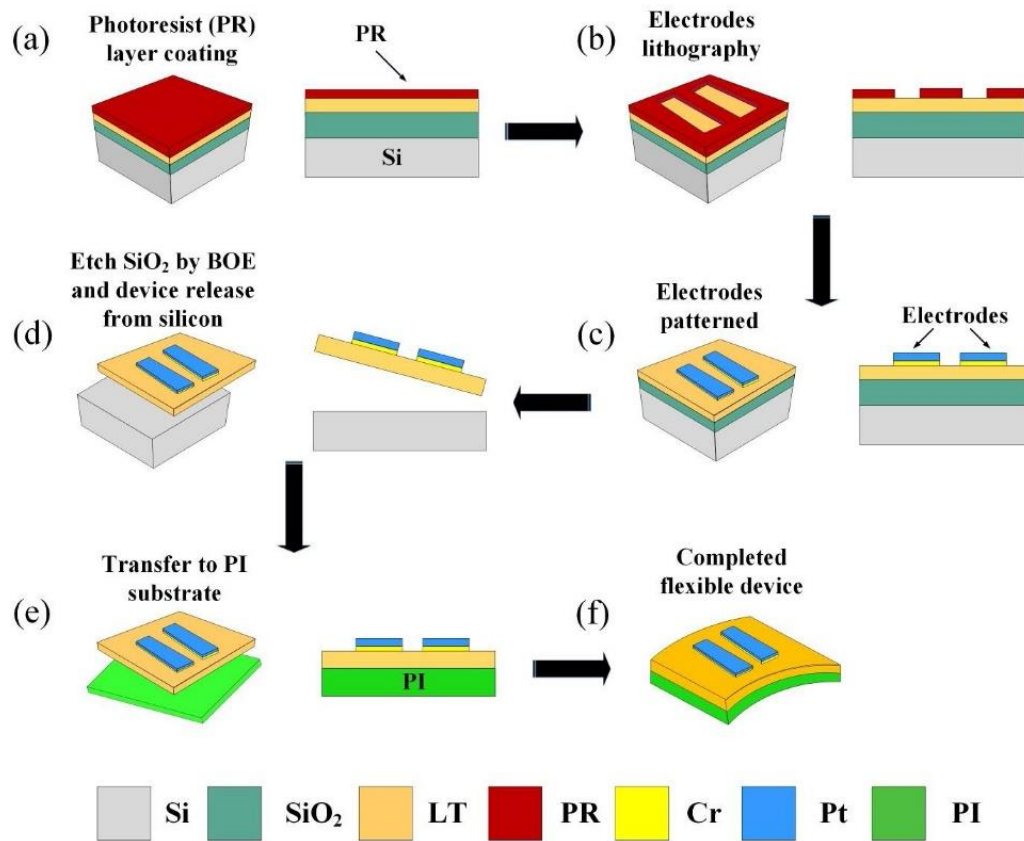
Figure 1.10: Fabrication protocol of the Lateral Field Excited flexible resonator [64]*.*

In this case, the mechanical wave is generated using a lateral exciting configuration in which the electrodes are patterned on the same face of the piezoelectric crystal. This configuration is not suitable for all piezoelectric materials because a strong interaction between the horizontal and vertical crystallographic axis becomes crucial.

The device has been fabricated on a wafer formed of a silicon material, an LT piezoelectric layer and a Silicon Oxide (SiO_2) sacrificial layer in between. The platinum (Pt) electrodes have been patterned using standard optical lithography, then the device has been detached from the silicon with the etching of the SiO_2 layer and attached to the final PI substrate.

The world of radio sensors is very diverse. Given the possibility of their integration on flexible substrates, microstrip resonators and MEMS are the most effective in wearable scenarios.

In chapter 2 the theory for the developing of these devices is detailed. In chapter 3 the techniques for their fabrication processes are explained in depth. In chapter 4 a new algorithm for the design of FBARs suitable for rapid prototyping flexible devices is presented. The advantage of the algorithm is optimal precision despite very low computational costs. The approach has been used for the design of an FBAR working at 2.55 GHz including fabrication tolerances through Monte Carlo simulations. The device has been fabricated and characterized proving the validity of the approach and reporting a very low relative error of 0.2%. Thanks to its optimal precision, in chapter 5 the algorithm has been used for the fine-tuning of the single-stage resonators of pass-band ladder filters. The procedure has been validated through the inverse-engineering of an existing filter with optimal results and a new sub-6GHz working at 5G filter has been designed. The stack designed by the algorithm has been fabricated on flexible substrates exploiting two different techniques. The first, detailed in chapter 6, concerns the fabrication of an FBAR on a polymeric substrate, without the releasing of the structure. Indeed, the reflection at the bottom surface is obtained through a molybdenum/polyimide acoustic interface. This approach has allowed the reduction of fabrication costs and enhanced the robustness of the resonator. In addition to the design algorithm, the stack has been simulated using a FEM model, to prove the effectiveness of the reflective interface. The device has led to optimal performance reporting the highest Figure of Merit (FoM) as regards flexible FBARs and has been tested as a gravimetric sensor. The main issue of the device is the non-optimal confinement of the mechanical wave, which end-ups in a low Q-factor. Therefore, the second generation of resonators, treated in chapter 7, has been developed on polymeric airgaps and on a 35 μm-thick Kapton substrate. The use of a suspended structure has led to a higher Q-factor and the flexible membrane support layer has helped the stability of the membranes. In the last part of this chapter, the combination of nine resonators has been tested through electrodes having an innovative shape able to excite all the forming resonators in parallel. The combination of the resonators has taken to a higher Q-factor of one order of magnitude with respect to the single device and after further optimizations of the common electrodes, this result can be

even improved. MEMS resonators offer optimal performance, micrometric footprints combined with high Q-Factors, at the cost of expensive fabrication processes. For this reason, a cost-effective solution is proposed in chapter 8 which involves the development of a microstrip multiple CSRR. The device has been exploited as a water volume sensor with optimal results, proving its suitability for skin applications such as sweat analysis. In addition, the resonator works when dipped in water as a temperature sensor, enabling its use also inside the body, for instance, as an ingestible sensor.

Finally, the design and fabrication of flexible antennas has been presented in chapter 9. A Patch and a PIFA antennas have been developed on a PEN substrate with optimal results. The future development of this activity can be the integration with the previously cited RF-resonators, e.g., MEMS and microstrip, to pave the way to a new class of wearable and wireless sensors.

Chapter 2- Theory for the design of radiofrequency resonators

The design of microwave resonators presents several critical issues. Firstly, the appropriate kind of resonator has to be chosen depending on the application. In general, MEMS and microstrip resonators are two technologies easily applicable on flexible substrates and they can be implemented with optimal results on the development of wearable wireless sensors.

The design of MEMS resonators needs to optimise the coupling of electromagnetic and mechanical physics. For this purpose, there are several analytical models, but a closed-form description becomes very difficult when considering complex systems; therefore, FEM comes to the aid.

Differently, microstrip resonators can be designed by considering only Maxwell's equations describing the propagation of electromagnetic fields into the resonating area. Although the presence of a single physic simplifies the model, the description of complex geometries becomes ineffective, and several numeric models have been developed through the years. FEM has been applied efficiently, but also FDTD and the Method of Momentum (MoM) can be used for the scope.

In this chapter, the theoretical background for the design of microwave resonators on flexible substrates is exposed. In the first part the theory behind the MEMS resonators, the piezoelectric effect and mechanical propagations are detailed. Then, the numerical methods for the estimation of the resonators are explained.

2.1- Piezoelectric Effect

Direct piezoelectricity is the property of a material to convert applied mechanical stress (T) into electric field (**D**, electric displacement). On the contrary, the inverse piezoelectric effect represents the capability of the material to convert applied electric fields (**E**) into mechanical strain (**S**). The direct and inverse piezoelectric effects can be expressed as reported in equation 2.1.

$$D_i = d_{ikl}T_{kl} + \epsilon_{ik}^T E_k \qquad (2.1)$$

$$S_{i,j} = s_{ijkl}^E T_{kl} + d_{kij} E_k \tag{2.2}$$

where d_{ikj} is the matrix for the direct piezoelectric effect, ϵ_{ik}^T is the electrical permittivity at constant stress **T** and s_{ijkl}^E is the mechanical elasticity matrix related to the Hook's law for elastic material at constant applied electric field **E**.

The direct piezoelectric effect (Equation 2.1) has been deeply used for the development of pressure, deformation, or acoustic/ultrasonic sensors.

Equations 2.1 and 2.2 can be expressed in matrix form as detailed in Equation 2.3, considering just the XY plane, as the symmetric behaviour of the piezoelectric materials versus the z-axis and the superscript t stands for the transpose [65], [66]:

$$\begin{bmatrix} S \\ D \end{bmatrix} = \begin{bmatrix} s^E & d^t \\ d & \epsilon^T \end{bmatrix} \begin{bmatrix} T \\ E \end{bmatrix} \tag{2.3}$$

$$\begin{bmatrix} S_1 \\ S_2 \\ S_3 \\ S_4 \\ S_5 \\ S_6 \\ D_1 \\ D_2 \\ D_3 \end{bmatrix} = \begin{bmatrix} s_{11}^E & s_{12}^E & s_{13}^E & 0 & 0 & 0 & 0 & 0 & d_{31} \\ s_{21}^E & s_{22}^E & s_{23}^E & 0 & 0 & 0 & 0 & 0 & d_{32} \\ s_{31}^E & s_{32}^E & s_{33}^E & 0 & 0 & 0 & 0 & 0 & d_{33} \\ 0 & 0 & 0 & s_{55}^E & 0 & 0 & 0 & d_{15} & 0 \\ 0 & 0 & 0 & 0 & s_{55}^E & 0 & d_{15} & 0 & 0 \\ 0 & 0 & 0 & 0 & 0 & s_{66}^E & 0 & 0 & 0 \\ 0 & 0 & 0 & 0 & d_{15} & 0 & \epsilon_{11}^T & 0 & 0 \\ 0 & 0 & 0 & d_{15} & 0 & 0 & 0 & \epsilon_{11}^T & 0 \\ d_{31} & d_{31} & d_{33} & 0 & 0 & 0 & 0 & 0 & \epsilon_{33}^T \end{bmatrix} \cdot \begin{bmatrix} T_1 \\ T_2 \\ T_3 \\ T_4 \\ T_5 \\ T_6 \\ E_1 \\ E_2 \\ E_3 \end{bmatrix} \tag{2.4}$$

where Voigt's notation has been used, according to the relations in equations 2.5, 2.6, 2.7, and 2.8 .

$$S = [S_1, S_2, S_3, S_4, S_5, S_6] = [S_{11}, S_{22}, S_{33}, 2S_{23}, 2S_{13}, 2S_{12}] \tag{2.5}$$

$$T = [T_1, T_2, T_3, T_4, T_5, T_6] = [T_{11}, T_{22}, T_{33}, T_{23}, T_{13}, T_{12}] \tag{2.6}$$

$$D = [d_1, d_2, d_3] \tag{2.7}$$

$$E = [E_1, E_2, E_3] \tag{2.8}$$

2.1.1- Modelling of piezoelectric thin films

Equation 2.4 can be used to describe any piezoelectric material, however, in the case of piezoelectric thin films, an approximation can be applied. Indeed, when the structure to be modelled is a thin plate, the normal stress in the thickness directions and the shear stress components can be neglected leading to:

$$\boldsymbol{T} = [T_1, T_2, T_3, T_4, T_5, T_6] = [T_{11}, T_{22}, 0,0,0, T_{12}] \tag{2.9}$$

Therefore, substituting Equation 2.9 in the general Equation 2.4 the model of a piezoelectric thin film is given, as in Equation 2.10:

$$\begin{bmatrix} s_{11}^E & s_{12}^E & 0 & 0 \\ s_{12}^E & s_{11}^E & 0 & 0 \\ 0 & 0 & s_{66}^E & 0 \\ -d_{31} & -d_{31} & 0 & 1 \end{bmatrix} \cdot \begin{bmatrix} T_1 \\ T_2 \\ T_6 \\ D_3 \end{bmatrix} = \begin{bmatrix} 1 & 0 & 0 & -d_{31} \\ 0 & 1 & 0 & -d_{31} \\ 0 & 0 & 1 & 0 \\ 0 & 0 & 0 & \epsilon_{33}^T \end{bmatrix} \cdot \begin{bmatrix} S_1 \\ S_2 \\ S_6 \\ E_3 \end{bmatrix} \tag{2.10}$$

The applied electric filed versus displacement form is reported in 2.11:

$$\begin{bmatrix} c_{11}^E & c_{12}^E & 0 & -e_{31} \\ c_{12}^E & c_{11}^E & 0 & -e_{31} \\ 0 & 0 & c_{66}^E & 0 \\ e_{31} & e_{31} & 0 & \epsilon_{33}^S \end{bmatrix} = \boldsymbol{C} \tag{2.11}$$

And the reduced elastic, piezoelectric, and permittivity constants are:

$$c_{11}^E = \frac{s_{11}^E}{(s_{11}^E + s_{12}^E)(s_{11}^E - s_{12}^E)} \tag{2.12}$$

$$c_{11}^E = \frac{-s_{12}^E}{(s_{11}^E + s_{12}^E)(s_{11}^E - s_{12}^E)} \tag{2.13}$$

$$c_{66}^E = \frac{1}{s_{66}^E} \tag{2.14}$$

$$e_{31} = \frac{d_{31}}{s_{11}^E + s_{12}^E} \tag{2.15}$$

$$\epsilon_{33}^S = \epsilon_{33}^T - \frac{2d_{31}^2}{s_{11}^E + s_{12}^E} \tag{2.16}$$

2.2- Finite Element Models

Even if some approximation can be applied, the mathematical model of a piezoelectric thin film results in a complex system of equations. Alternatively, the

study of huge extended geometries is usually performed using numerical algorithms able to derive the response of a piezoelectric device by computers.

FEM analysis is one of the most popular numerical methods.

The method comprises four main steps:

- Discretising the space region of the system to be studied into unit elements, called Finite Elements (FEs).
- Deriving governing equations for each element.
- Assembling all elements.
- Solving the matrix system.

The advantage of solving the problem in the frequency domain is the possibility to express it in a linear form as in Equation 2.17.

$$F = Ku \qquad (2.17)$$

where F is the output, u is the input and K, called stiffness matrix, is the property of the structure. Equation 2.17 is derived for all the elements of the region of the solution and assembled in a unique system expressed in the forms of matrixes as in Equation 2.18.

$$\{F\} = [K]\{u\} \qquad (2.18)$$

The stiffness matrix [**K**], whose elements are called $k_{i,j}$ represents the effect on the i-th element due to the input applied to the j-th element. It is worth noting that the more the j-th input is near to the i-th element, the higher the reported effect is, therefore the matrix [**K**] is a diagonal sparse matrix and has a form as the one below:

$$[K] = \begin{pmatrix} k_{11} & k_{12} & 0 & 0 & ... & 0 & 0 & 0 \\ k_{21} & k_{22} & k_{23} & 0 & ... & 0 & 0 & 0 \\ ... & ... & ... & ... & ... & ... & ... & ... \\ 0 & 0 & 0 & 0 & ... & k_{n-1,n-2} & k_{n-1,n-1} & k_{n-1,n} \\ 0 & 0 & 0 & 0 & ... & 0 & k_{n,n-1} & k_{n,n} \end{pmatrix} \qquad (2.19)$$

This kind of matrix is invertible through well know algorithms so the $[K]^{-1}$ matrix can be given [67]. Finally, the solution to the problem can be found by inverting Equation 2.19.

$${u} = [K]^{-1}{F} \tag{2.20}$$

Given its peculiarity, FEM is more suitable for complex geometries. However, the complexity of the problem increases exponentially with the dimensions of the model. In addition, it is difficult to computationally parallelise the FEM operations as the execution requires the inversion of the stiffness matrix.

2.3- FDTD Method

A different approach to the numerical modelling of RF resonators is represented by the FDTD method. Although the method can be applied to a huge number of EM problems, the inclusion of piezoelectric materials becomes difficult using commercial software. However, FDTD has been successfully used for the design of a huge variety of RF resonators [68]–[74].

FDTD derives the EM field by solving of Maxwell's equations for a given geometry and arbitrary sources. As a first step, the geometry and the forming materials properties have to be specified. The material can be conductive or dielectrics. New materials can be inserted by the specification of their electromagnetic properties. Then, the sources have to be defined in terms of the position and characteristics of exciting signals.

The algorithm starts with the expression of the Maxwell's Equations in the time domain.

$$\frac{dE}{dt} = \frac{1}{\varepsilon_0} \nabla \times H \tag{2.21}$$

$$\frac{dH}{dt} = -\frac{1}{\mu_0} \nabla \times E \tag{2.22}$$

The problem is simplified in one dimension, considering the EM wave travelling through the z-axis direction.

$$\frac{dE_x}{dt} = -\frac{1}{\varepsilon_0} \frac{dH_y}{dz} \tag{2.23}$$

$$\frac{dH_y}{dt} = -\frac{1}{\mu_0} \frac{dE_x}{dz} \tag{2.24}$$

Then, the entire geometry is discretised in time and space and Equations 2.23 and 2.24 are solved for each single element instant by instant exploiting the central difference approximations following Yee's scheme [75].

More in specific the vectors E_x and H_y are considered shifted in time and space of one-half of a unit cell (see equations 2.25 and 2.26).

$$\frac{(E_x^{n+\frac{1}{2}}(k) - E_x^{n-\frac{1}{2}}(k))}{\Delta t} = -\frac{1}{\varepsilon_0}\frac{(H_y^n(k+1/2) - H_y^n(k-1/2))}{\Delta z} \tag{2.25}$$

$$\frac{(H_y^{n+1}\left(k+\frac{1}{2}\right) - H_x^n\left(k-\frac{1}{2}\right))}{\Delta t} = -\frac{1}{\mu_0}\frac{(E_x^{n+1/2}(k+1) - (E_x^{n-1/2}(k+1))}{\Delta z} \tag{2.26}$$

The formula used for the FDTD algorithm can be found in Equations 2.27 and 2.28.

$$(E_x^{n+\frac{1}{2}}(k) = E_x^{n-\frac{1}{2}}(k)) + \frac{\Delta t}{\varepsilon_0}\frac{(H_y^n(k+1/2) - H_y^n(k-1/2))}{\Delta z} \tag{2.27}$$

$$H_y^{n+1}\left(k+\frac{1}{2}\right) = H_x^n\left(k-\frac{1}{2}\right) + \frac{\Delta t}{\mu_0}\frac{(E_x^{n+1/2}(k+1) - (E_x^{n-1/2}(k+1))}{\Delta z} \tag{2.28}$$

The algorithm evaluates the E_x and H_y, for each time step and at each point k. The determination of the spatial and time resolutions is extremely important to correctly estimate the EM fields. In general, the minimum spatial resolution Δz can be taken as one-tenth of the smallest EM wavelength in the material. The time-step is determined starting from the spatial resolution Δz. For stability reasons, the waves cannot propagate more than one Δz in a single time step. This condition is expressed as the Courant condition.

$$\Delta t \leq \frac{\Delta z}{c_0\sqrt{d}} \tag{2.29}$$

where d is equal to 1,2,3 for one-, two- or three-dimensional problems, respectively. Commonly Δt is taken equal to [75]:

$$\Delta t \leq \frac{\Delta z}{2c_0} \tag{2.30}$$

The Finite Difference Time Domain (FDTD) method can be used to efficiently simulate the EM field generated in resonators. However, the grid in FDTD has to be finite, therefore the analysis domain has to be truncated at some point. The termination of the grids can cause reflections and then, influence the final result. To minimise this effect, FDTD uses boundary conditions.

In this case, the points at the end of the grid are treated as special absorbers able to absorb all the incoming waves [76].

Differently from FEM, FDTD can be easily computationally parallelised using cluster processors, reducing the computational times [77], [78].

Chapter 3 Fabrication techniques

Besides the design methods, the choice of the most appropriate fabrication process becomes essential to achieve big process yields and reduction of time and costs. In this regard, several techniques can be exploited, catalogable into two main approaches: additive and subtractive. In the subtractive approach, the structuring of the layers composing the device is obtained by depositing the material on the whole surface and by selective etching with the exploitation of a positive process mask. Instead, in the additive, the forming of the device is performed by selectively depositing the forming material on the substrate. The lift-off technique and 3D printing are the most popular fabrication methods exploiting this approach.

In this chapter the fabrication methods commonly exploited for the fabrication of flexible resonators are detailed.

In the first part, the deposition techniques for the forming materials and the optical lithography processes are exposed. Then, in the second part the two approaches, e.g., additive and subtracting, are explained.

3.1- Deposition Techniques

One of the basic building blocks of the manufacturing of RF resonators is the deposition of materials. Different kinds of deposition techniques can be subdivided into chemical reactions or physical mechanisms.

One of the most used chemical processes is Chemical Vapor Deposition (CVD). In CVD the materials to be deposited, or its chemical components, are converted into gas form and injected into a vacuum chamber containing the substrate. Atoms react and condensate after hitting the substrate producing high homogeneous and conformal thin films.

An example of a machine performing the CVD is the parylene coater, reported in Figure 3.1.
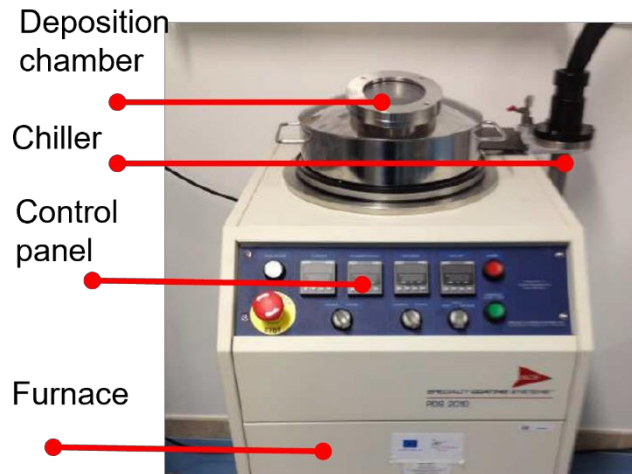
Figure 3.1: Parylene coater.

The deposition process consists of three main steps:

- vaporization, where pellets of solid-state parylene dimers are heated to a gaseous state.
- Pyrolysis, when the material is heated and cleaved into a monomer.
- Polymerization, the vapour molecules condensate onto the substrate at room temperature in a deposition chamber kept under vacuum.

A thermal trap block gas wastes from the deposition chamber. The parameter of the process, such as rotation of the substrate holder, pressure into the chamber, and temperature of the vaporiser and of the furnace can be set from the control panel. Parylene is a very popular material used in RF manufacturing because of its optimal properties such as electrical insulation, moisture barrier, and protection against corrosion or chemical attack. Moreover, it is biocompatible and highly suitable for wearable applications.

Another technique for material deposition is a physical deposition mechanism called Physical Vapor Deposition (PVD), exploited through sputtering systems. The sputtering is composed of:

Deposition chamber: large chamber containing the guns and the target materials.
Target material: source of the material to be deposited, contained in a specific location named gun.
Power generator: generator of the excitation applied to the gun of the target material, used to ionise the atoms of the gas and to obtain the plasma.

Figure 3.2 illustrates a typical sputtering deposition system. In Figure 3.2a. a view of the machine is shown where it can be noted the deposition chamber and the panel for the control of the system including the excitation frequency and power. The sputtering system contains two different generators depending on the particular application, a Direct Current (DC) generator and DC pulsed generator. The machine has recipe libraries for storing past process parameters. Figure 3.2b shows the inner of the deposition chamber. There are three guns relative to different target materials, in this case, Aluminium (Al), Molybdenum (Mo), and Ti. On the top surface, the substrate holder is placed. The holder of the substrate can be rotated on its central axis to enhance the homogeneity of the film.

Before the deposition starts, the gun corresponding to the desired material is rotated to be moved at a specific distance from the substrate.
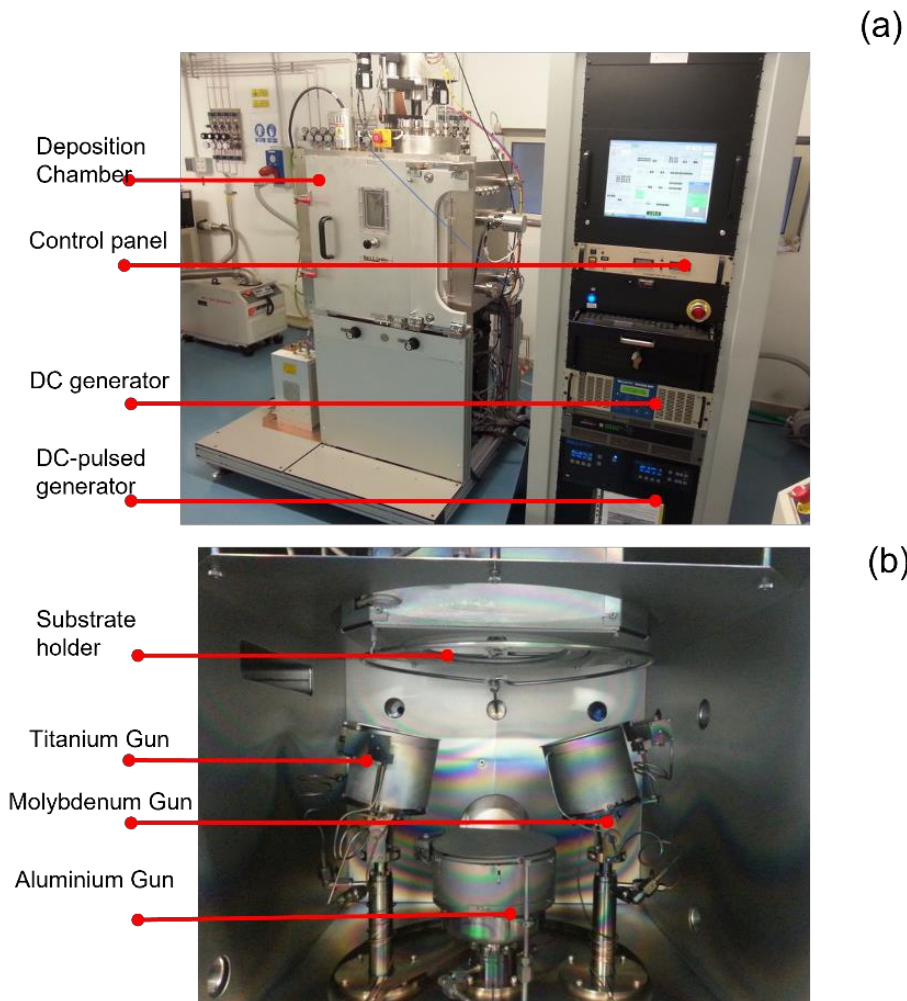
Figure 3.2: Sputtering deposition system, a) sputtering system, b) deposition chamber.

Then the deposition chamber is filled with an inert gas, usually Argon and the gas is converted into plasma by power excitation. A voltage is applied between the target (negative electrode, cathode) and the substrate (positive electrode, anode). The free atoms of the inert gas are excited by the power source and are accelerated through the chamber. The energy transfer ionizes them, and a cascading process is established until a plasma is developed. The starting condition of the process is named breakdown voltage and depends on some parameters such as the specific inert gas, the pressure in the chamber and the distance between the anode and the cathode. The electrical potential accelerates the plasma ions from the anode to the cathode against the target. This effect causes the ejection of atoms from the target that are deposited on the substrate.

In reactive sputtering, the chamber is filled with a combination of inert and non-inert gasses. In this case, the depositing material is obtained through a chemical reaction between the atoms from the target and the ones of the non-inert gas. This process is commonly used for the deposition of dielectric materials such as Zinc Oxide, Silicon Dioxide, or Aluminium Nitride.

Depending on the kind of signal driving the power source, sputtering can be classified as DC, DC Pulsed, or RF. DC sputtering is commonly used for the deposition of metals. In this case, the power source is set to a constant positive voltage during the deposition process. In the case of dielectric depositions, some atoms can agglomerate on the target causing a reduction of the applied voltage which translates into lower powers and deposition rates. Therefore, in the DC-pulsed technique, the voltage is switched between positive and negative periodically, to clean the target from any undesired deposition compound. The frequency of the switching is in the order of kilohertz. Finally, in RF sputtering, the frequency is in the megahertz (about 13 MHz) range. In general, the amount of exciting power drives the speed of the ions hitting the target: the higher the power, the higher is the number of collisions and the rate of the process. If the ions are restricted to move in the target region, the rate can be improved without increasing the excitation level. This operation is performed using magnetic fields in magnetron sputtering. Moreover, magnetic fields limit the interaction between the substrate and the bombarding particles and improve the quality of the deposition.

AlN is one of the most attractive among other piezoelectric thin films achievable through sputtering deposition. This material is commonly used in MEMS piezoelectric systems because of its advantages such as high phase velocities (up to 11000 m/s), decent electromechanical coupling factors (about 5%), and very low dielectric losses (0.0002) [26]. Given its peculiarity represents the best choice to combine piezoelectricity with radio frequencies. Moreover, its growth in flexible materials has been demonstrated in several works [28], [30], [31], [37].

AlN can be deposited utilizing DC-pulsed or RF reactive sputtering from Al targets in an Argon inert and nitrogen (N_2) non-inert gas environment. The crystal orientation and chemical composition of the films depend upon the sputtering power, pulse frequency, duty cycle, growth temperature, nitrogen/argon flow ratio, and sputtering pressure. In general, high nitrogen flow rates, high powers, and lower temperatures are preferred [79], [80].

3.2- Optical lithography

Optical lithography is a process that transfers a pattern to the substrate through the use of a photoresist. The photoresist is a resin whose molecules polymerise after the exposition to electromagnetic radiation and changes its solubility to a solution called "developer." In general, there are two kinds of photoresists: in the positive, the exposure to UV light breaks the polymeric bonds between the molecules. Consequently, the resist becomes soluble to the developer. In the negative resist, the UV light causes a cross-linking reaction which strengthens the bonds between molecules, making the resist soluble only in the unexposed regions.

Commonly, the pattern is impressed on the photosensitive layer utilizing a Mask Aligner (MA). This machine allows the fine control of the horizontal and vertical positions of the sample with respect to the mask and the exposure power. A typical MA exposure system is shown in Figure 3.3.

The components of the system are:

Mask holder: the site of the lithographic mask. The mask is held through a strong vacuum. The size of the holder can be varied accordingly to the dimensions of the mask.

Substrate holder: the plate containing the substrate under process. Usually, the substrate is kept in place by applying vacuum to the sample holder. The position of this holder can be varied in vertical and horizontal directions. The XY-plane is controlled through micrometric screws for fine alignment of the lithographic mask, while the distance between substrate and mask (Z-axis) is performed by air pistons. The higher the distance the lower the resolution. In general, the mask aligner allows different kinds of exposure: a) proximity: the substrate is placed at a certain distance to the mask customizable by the operator; this modality is preferred for low-resolution lithography and brittle substrates; b) soft contact: the substrate is placed on the mask surface but without the application of any force; c) hard-contact: the substrate is placed on the mask surface with the application of a force decided by the operator; d) vacuum contact: the adhesion between mask and substrate is strengthened under vacuum.

Microscope: The position of the substrate in the XY-plane is aligned using optical microscopes. Typically, there are two microscopes placed at the two extremities of the wafer.

Lamp: After the alignment between the substrate and mask, the exposure is performed through the emission of monochromatic UV radiation. The source of the UV is commonly Mercury (Hg) lamp, emitting a wavelength of 340 nm. The emitting dose can be controlled by varying the amount of power or the time of the exposure. The UV emission is focused on the exposing region through the use of an optical lens. Since the very high temperatures reached by the lamp a cooling system is always necessary, usually working through nitrogen flows.
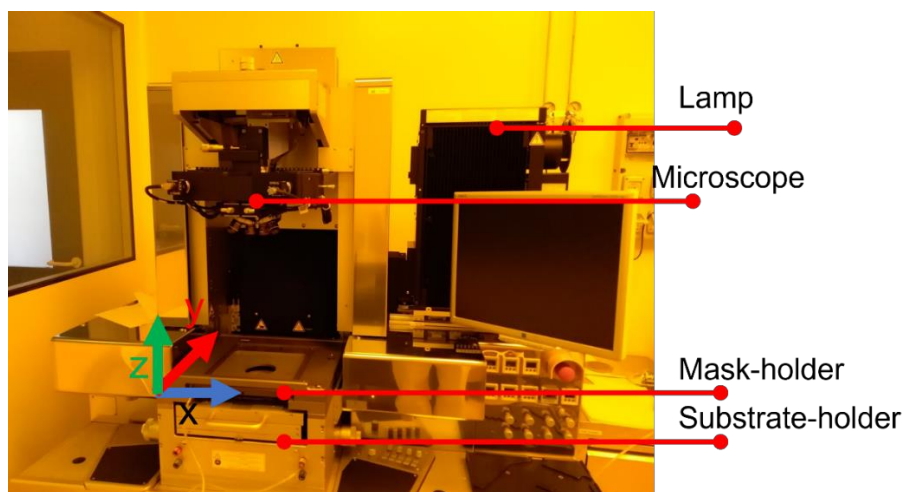
Figure 3.3: Mask-Aligner

3.3- Additive approach

The fabrication of devices can be performed by exploiting two complementary strategies.

In the additive approach the structuring is achieved starting with the deposition of the forming materials and the selective removal from the surface of the wafer of useless parts, with the application of a positive mask on a resist layer. Depending on the process, the photoresist can have different natures. The main requirement is its resistance to the etching process, ensuring an optimal patterning of the substrate.

3.3.1- Etching-mask fabrication

In general, masks can be obtained using positive lithography. It is a process used to pattern the photosensitive resist layer on the surface of the wafer. The process is performed through the following steps:

Spin coating of the resist: the wafer is covered with photosensitive material using a spin-coater. The speed of the spin-coating is an important parameter that determines the thickness of the resist and depends on its viscosity and the adhesion with the material of the substrate. It is important to stress that the thickness of the resist has to be higher enough to guarantee optimal protection during the patterning of the layers.

Pre-exposure bake: the resist is usually mixed with solvent molecules to help the spreading. It needs to be evaporated before the exposure on a heater. The time and the temperature of this phase strictly depend on the solution, the thickness, and the heat conductivity of the substrate.

Exposure: the pattern is impressed on the photosensitive layer by UV light exposition through the Mask.

Developing: the pattern is obtained through the dipping of the sample in the developer. The role of this solution is the solubilisation of the resist at the exposed areas. Lower pre-exposure bakes and high doses of exposure reduce the developing time at the cost of a lower resolution.

The resist mask can be used directly to pattern the substrate or can be exploited for the fabrication of hard masks made of more durable materials.

The best performance of the additive approach is when the resist has vertical sidewalls (see Figure 3.4a). This condition is achieved by tuning the emission dose. Too much light-dose exposes the bottom of the resist layer by diffraction from the substrate. This results in positive sidewalls of the resist which limits the maximum resolution (see Figure 3.4b).
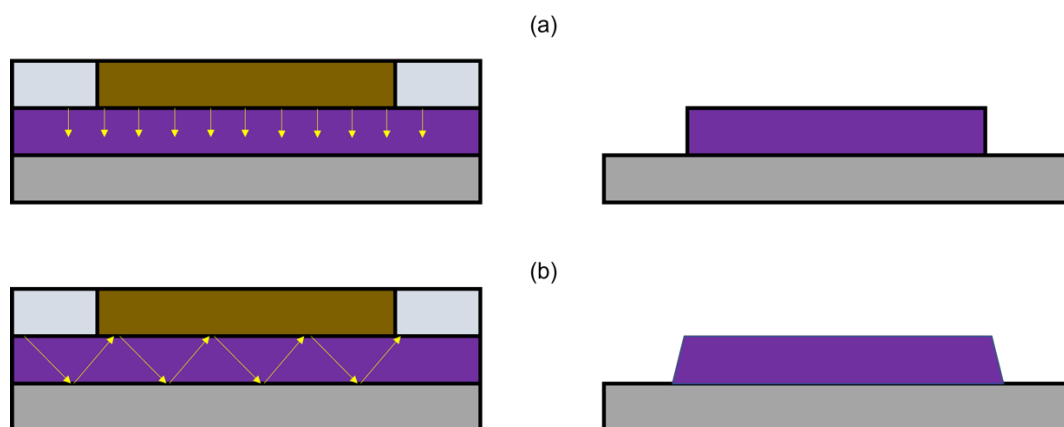
Figure 3.4: Resist exposure a) vertical profile, b) positive profile.

3.3.2- Etching of the material

After the fabrication of the positive mask, an etching process is performed. There are two kinds of etching: a) wet etching, exploited by dipping the wafer in chemical solutions, which erode the material; b) dry etching, performed by exposing the substrate to ionised gasses able to etch the surface. Wet etching is preferred for low resolutions and small thicknesses; indeed, dry etching is more directive and ensures higher resolutions.

The most used method for dry etching is the Inductive Coupled Plasma Reactive Ion Etching (ICP-RIE), where electric and magnetic fields are exploited to generate a gas plasma. The ICP is made by a vacuum chamber containing the wafer plate. Gasses can enter the chamber from the top through small inlets and are accelerated by RF power (usually set at 13.56 MHz) to form plasmas. ICP-RIE can be performed using fluorinated or chlorine-containing gasses for the chemical erosion; together with inert gasses, such as Argon, for the physical etching. Indeed, the combination of inert and reactive gas concentrations, together with the amount of RF power, drive the selectivity, the rate, and the anisotropy of the process.

At the end of the etching, the mask on the wafer has to be removed. When the protecting material is a photoresist, this operation is performed using a resist stripper, usually acetone and IsoPropAnol (IPA). Alternatively, reactive oxygen plasma can be used for the complete removal of any resist molecule from the surface.

3.4- Subtractive approach

In this strategy, the structuring is not obtained via the erosion of the surface, but by selective deposition of the material at sites that are not protected by a negative mask. In this case, the mask is obtained using inverse lithography.

The steps of the inverse lithography are the same as the positive but two additional steps are performed after the exposure:

Post-exposure bake completes the cross-linking reaction that occurred during the exposure. The parameters of this process have an enormous influence on the developing rate and the resolution of the pattern and have to be carefully optimised. Flood-exposure: the sample is exposed to UV radiation without any mask. This step helps the stabilization of the inverted resist and is performed at a dose at least five times higher than the first exposure.

The resist presents a cross-linked area, not soluble in the developer, corresponding to the exposed region. As a consequence, after developing a negative profile of the desired pattern is produced on the wafer. In inverse lithography, a negative profile of the sidewall of the resist is preferred. Indeed, in this case, the resist stripper can penetrate better under the deposited material (see Figure 3.5a). Indeed, in a positive profile (see Figure 3.5b), the stripper cannot reach the sidewalls of the resist making the delamination more difficult.

(a)

(b)
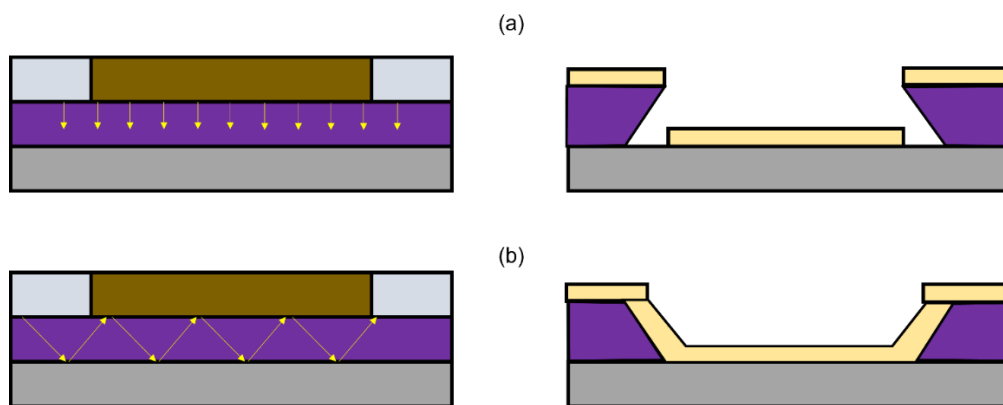
Figure 3.5: Inverse lithography, a) negative resist profile, b) positive resist profile.

The negative profile can be achieved by making the areas near the substrate unexposed. Therefore, the light emission dose has to be tuned so that the UV light cannot penetrate the entire resist profile.

Finally, the forming material is deposited on the wafer. The material attached to the resist delaminates after dipping the negative in a resist stripper, such as Acetone.

3.5- Multi-material 3D Printing

Multi-material 3D printers are very powerful machines commonly used in the manufacturing of Printed Circuit Boards (PCBs). This instrument can develop PCBs by directly printing the dielectric layer and conductive traces starting from the specification of the specific layer geometries in Gerber (.gbr) format. Besides the geometry definition, the machine also needs the specification of the material (dielectric or metal) and the thickness of each layer; together with the overall dimensions of the PCB (root). Then, the printer converts this information into layer-by-layer instructions for the depositions of the dielectric and conductive inks.

The Nano dimensions Dragonfly 3D multi-material ink-jet printer has been used for the fabrication of flexible circuitry with optimal results [81], [82]. The machine is based on dielectric proprietary and silver (Ag) nanoparticle-based conductive inks deposited through hundreds of nozzles present on the printing head. The curing and sintering of the Ag-based ink are carried out at a temperature of 140°; while the dielectric ink is polymerised with UV radiation.

Although their optimal properties, the use of 3D multi-material printed PCBs has some limitations if applied to flexible substrates. In particular, the printed dielectric material used by most printers is not flexible, therefore, metal traces need to be printed on different substrates able to guarantee the bendability of the device. However, the adhesion between the metal inks and the flexible substrates usually needs to be optimised. This can be done by plasma oxygen treatments of the substrates [83], or by depositing thin interlayers of dielectric inks before the metal traces.

Chapter 4- New approach for rapid prototyping FBARs

Commonly FBARs are designed using the Equivalent Circuit Analysis (ECA) [46], [84], [85] or the FEM [58], [85], [86]. These methods always require knowledge of the specifications of the materials composing the stack. These specifications depend on the equipment technology and status, the deposition recipes, environmental conditions, and so on. In addition, each deposition process introduces a degree of uncertainty on the thickness of each layer because of the fabrication tolerances. The correct estimation of the thicknesses of the layers forming the stack represents a crucial issue as even small variations of the top electrode or piezoelectric layer generates a drift of the resonant frequency because of the mass-loading effect. All these drawbacks, if included in the commonly used design models, increase the computational time [58]. In Reference [87] the FEM simulations are combined with a deep learning approach based on artificial neural networks; but thousands of simulated data are necessary, making the method not suitable for fast prototyping. Differently in Reference [88] this problem has been treated using FEM simulations whose parameters are refined with a closed feedback loop to minimize the error with respect the measured data; however, this approach requires a very high computational cost as exploits 3D FEM simulations.

Besides the design problems, the use of a back trench etching to obtain suspended membranes causes the fragility of the resonators. Moreover, the use of Solid Mounted Resonators (SMRs) avoids the release of the piezoelectric layer but lowers the performance compared to other solutions. The trade-off between the two approaches is represented by membranes on airgap, fabricated by employing a sacrificial layer [44]–[46], [89], [90], whereby the structure is suspended on. The presence of a membrane support layer ensures higher robustness, but also in this case the fragility of the suspended structure is an open issue in the case of FBARs working with very thin films. Moreover, the removal of the sacrificial layer always requires aggressive chemicals that can damage the other materials complicating their integration and increasing times and costs [26].

In this scenario, the fabrication of the first airgap FBAR based on a high-soluble organic sacrificial layer made of Lift-Off Resist (LOR) and suspended on a

polymeric flexible membrane is presented. The device exploits longitudinal propagation and is based on a c-axis oriented Aluminium Nitride piezoelectric thin-film vertical excited. Differently from other air-gap structures reported in the literature, with the proposed fabrication protocol the removal of the sacrificial material becomes very straightforward as does not require any aggressive chemicals. In addition, the presence of the flexible membrane support layer enhances the robustness of the structure by avoiding the formation of cracks and the collapse of the stack. The resonator has been designed by a new algorithm based on a proper material library comprising the most common metals used in the MEMS industry. The advantage of this approach is the possibility to include fabrication tolerances and experimental material properties at the design level, increasing the rapidity of prototyping. Moreover, the modularity of the algorithm allows including new materials using the systematic procedure detailed in the next sections without any modification of the code. The resonant frequency of the FBAR has been correctly estimated by the design algorithm at 2.55 GHz with a very low error of 0.005 GHz (about 0.2%). The fabrication protocol has led to a high-performance resonator having an electromechanical coupling factor of 4.7% and very high-quality factors of 1426 and 1477 for the resonance and antiresonance, respectively.

4.1- Design algorithm

The structure of the design algorithm is sketched in Figure 4.1. There are three main building blocks: the decision core, the random perturbator, and the shared dataset.
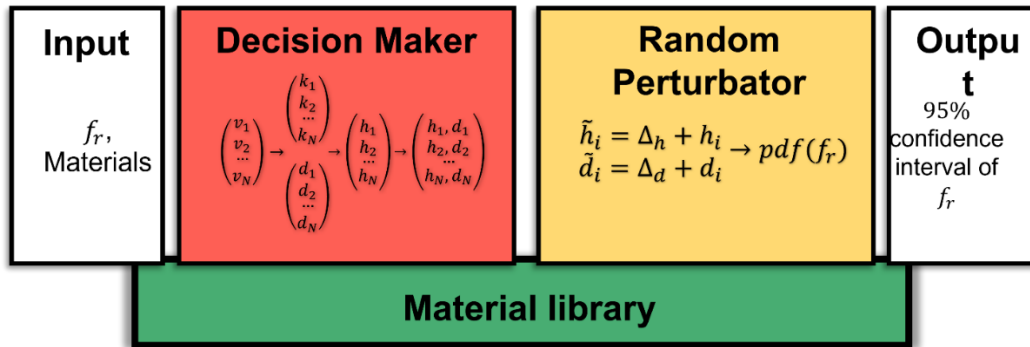
Figure 4.1: Structure of the design tool.

The decision maker takes as inputs the materials and the working frequency and returns the set of solutions. Each solution is characterized by a phase velocity (v_i), which corresponds to a specific metal (h) over piezoelectric (d) thickness ratio (j_i). The tool allows the user to select the best in terms of fabrication constraints and times. After choosing a single-stack solution, the random perturbator estimates the Probability Density Function (P.D.F.) of the resonance value considering the fabrication tolerances of the deposition processes. The decision maker and the random perturbator are based on a material library that can be easily expanded with new materials without any modification to the algorithm and using the systematic procedure to obtain a material calibration curve, as detailed in the next section.

4.1.1- Study for New Calibration Curves

To obtain a calibration curve, the thicknesses of the piezoelectric material and all the layers below need to be set. Indeed, variations of the mass deposited on the piezoelectric layer modify the phase velocity and change the resonance frequency value (f_r) according to Equation 1.3. This effect is highlighted in Figure 4.2 reporting a parametric sweep considering a 1 μm-thick AlN piezoelectric layer and 180 nm-thick Molybdenum bottom electrode (see Figure 4.2a) and varying the aluminium top electrode (h) between 50 nm and 300 nm.

As can be seen from Figures 4.2b and 4.2d, the thicker the electrode, the lower is the resonant frequency and the phase velocity. The corresponding value of the phase velocity is taken from Equation 1.3 for each resonator having a different height of the top electrode (h). Finally, the calibration curve of the phase velocity is expressed as a function of the ratio h/d in Figure 4.2c.
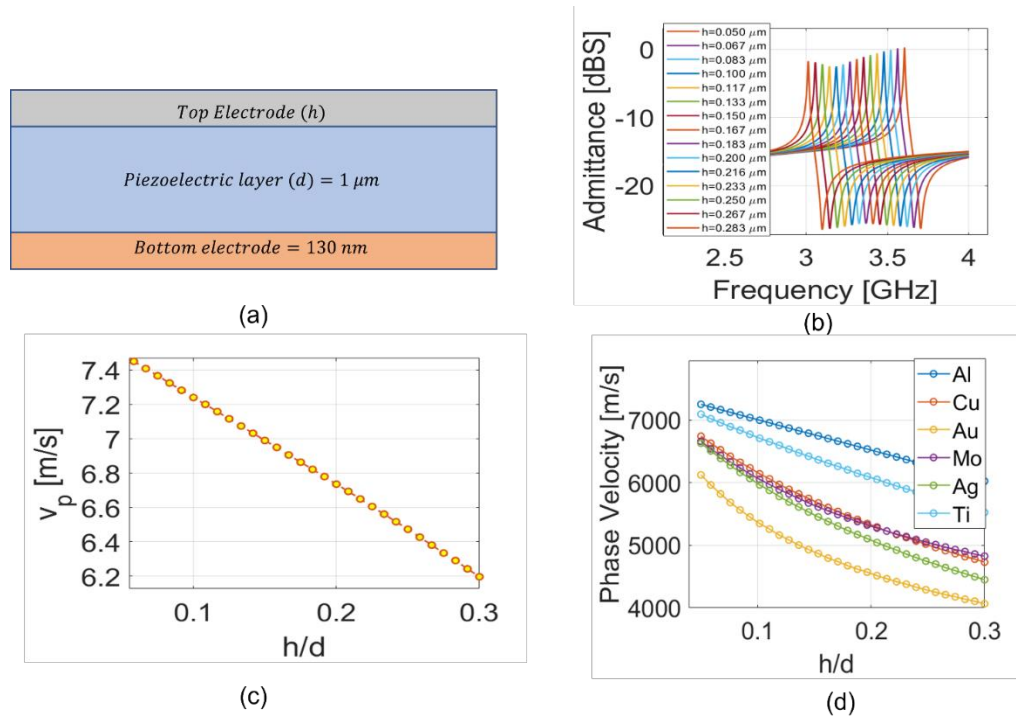
Figure 4.2: Parametric model used for the sweep of the aluminium top-electrode thickness; b) admittance of the resonator for various thicknesses, c) Phase velocity vs metal over piezoelectric thicknesses; d) data-set of calibration curves for different materials.

It is stressed that the gathering of data from previous processed devices and materials is a crucial advantage of this approach. Indeed, once a systematic study has been performed, with FEM simulations or with experimental data, the new design can use directly the data, skipping new simulations. For example, Figure 4.2d reports the calibration curves related to the commonest materials used in the MEMS industry (Al, Ti, Copper (Cu), Ag, Mo, and Gold (Au)), obtained [19], [20].

4.1.2- Decision Core

The decision core is responsible for the design of the layers composing the stack starting from the specification of the resonance value and the materials.

- The solution provided by the decision core is a set of N resonators having different j-ratio, but the same resonance frequency determined as in Equation 4.1.

$$A = \{j_1, j_2, \dots, j_i, j_{i+1}, \dots, j_N\} \tag{4.1}$$

- The procedure starts from the materials specified by the user for guessing a set of possible phase velocities of the acoustic wave travelling back and forth the resonating area, see Equation 4.2.

$$V = \{v_1, v_2, \dots, v_i, v_{(i+1)}, \dots, v_N\} \tag{4.2}$$

- The optimal value of j_i is derived using the bisection method from the corresponding calibration curve.

- Parallelly, the thickness of the piezoelectric layer is evaluated by solving Equation 1.3 concerning d, where v_i and f_{ri} are given.

- The height of the metal comes directly from the definition of j_i, given by Equation 4.3.

$$h_i = j_i \, d_i \tag{4.3}$$

4.1.3- Random Perturbator

The random perturbator core estimates the P.D.F. of the resonant frequency value given the fabrication tolerances of the deposition processes using Monte Carlo simulations.

- For each $j_i \in A$ the thicknesses of the piezoelectric and top-electrode layers are varied accordingly to Equation 4.4.

$$(j_i)^- = (h_i + \Delta h)/(d_i + \Delta d) \tag{4.4}$$

where Δh and Δd are aleatoric variables following uniform distributions between the specified values of the fabrication tolerances.

- The resonant frequency of each $(j_i)^-$ is estimated by taking the value of the phase velocity from the corresponding calibration curve and using Equation 1.3.

- The first two operations are repeated until the convergence of the P.D.F. occurs; in our case, the algorithm is repeated 50,000 times.

- The P.D.F. of the resonance value is obtained.

4.2- Design of an FBAR

In this section, we report the validation of our algorithm through the design and fabrication of an airgap FBAR resonator designed at a working frequency of 2.55 GHz. The frequency has been chosen in an unlicensed band to avoid interference with laboratory instruments or telecommunication infrastructures [91]. Figure 4.3a shows a schematic breakdown of the resonator constituted by the silicon substrate, an AlN of 135 nm, a Molybdenum bottom electrode of 220 nm, a piezoelectric Aluminium Nitride layer, and an Aluminium top electrode. Figure 4.3b reports all the possible solutions the decision algorithm provides. It is underlined that the total computational time of the algorithm has been shorter than one minute providing 21 configurations of the resonator having piezoelectric thicknesses comprised between 1.35 μm and 1.5 μm. We chose a piezoelectric thickness of 1.36 μm having a 180 nm-thick Aluminium top electrode (see Figure 4.3c). Because the thinner piezoelectric layer reduces the deposition times, the use of a thicker top electrode decreases the electrical losses increasing the performance of the resonator.

Figure 4.3d shows the P.D.F. returned by the random perturbator, where the thicknesses of the layers vary with a maximum error of 5%. The 95%-confidence interval of the resonance frequency is equal to 2546 MHz ± 23.5 MHz. In this case, also the computational time has been less than one minute.
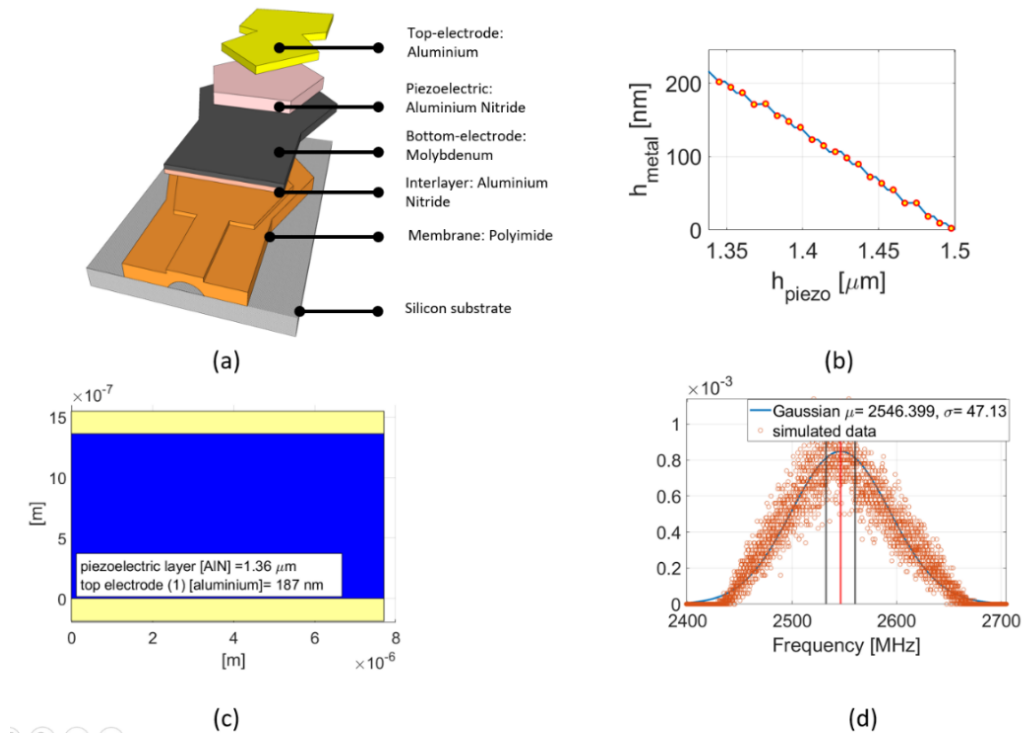
Figure 4.3: Design of the FBAR, a) breakdown of the device, b) family of solutions, c) single solution, d) P.D.F. of the resonant position.

4.3- Fabrication Protocol

The resonator has been fabricated using four lithographic steps: the sacrificial layer, the bottom electrode, the piezoelectric layer, and the top electrode, respectively. The fabrication steps are summarised in Figure 4.4. The microfabrication processing for the proposed resonator exploits an organic sacrificial layer made of LOR coated with a PI protection layer.

As a first step, an n-doped high-resistive silicon wafer has been coated with the LOR sacrificial material. A spin-coated photosensitive resist layer on the wafer has been patterned using optical lithography. During the development stage, the pattern has been transferred from the photosensitive material to the sacrificial layer (Figure 4.4a). After that, the resist has been stripped by dipping the sample in acetone. The sacrificial layer has been covered with a protective layer made of 2.5 μm-thick Polyimide (Figure 4.4b). The role of the polymeric layer is two-fold: on one side prevents the dissolution of the sacrificial layer during the following steps: and on the other side, the use of a flexible support layer avoids the cracking of the membrane and the collapsing of the structure. The FBAR stack has been fabricated

as follows: a 186 nm thick Aluminium Nitride interlayer has been deposited followed by the 220-nm thick Molybdenum bottom electrode. The metal and the interlayer have been patterned using direct lithography and BCl_3-based Inductively Coupled Plasma (ICP) etching (Figure 4.4c).

It is worth underlining that the role of the interlayer is important for three main reason: i) to ensure a good adhesion of the molybdenum on the polymeric substrate, ii) to enhance the piezoelectric crystal orientation, iii)to compensate the deformation stresses introduced by the deposition of the piezoelectric layer, preventing compressive stresses and formation of cracks.

The piezoelectric layer has been fabricated depositing a 1.36 μm-thick layer of Aluminium Nitride through DC-pulsed sputtering and patterned with the same approach as the previous interlayer/electrode layers (Figure 4.4d). The top electrode has been realized with negative optical lithography, followed by the deposition of a 180 nm thick Aluminium layer and the following lift-off step in acetone (Figure 4.4e). Finally, the PI protective layer has been etched by an O_2-based ICP etching. The sacrificial material has been dissolved by dipping the sample in PG-Removal for 2 hours (Figure 4.4f).
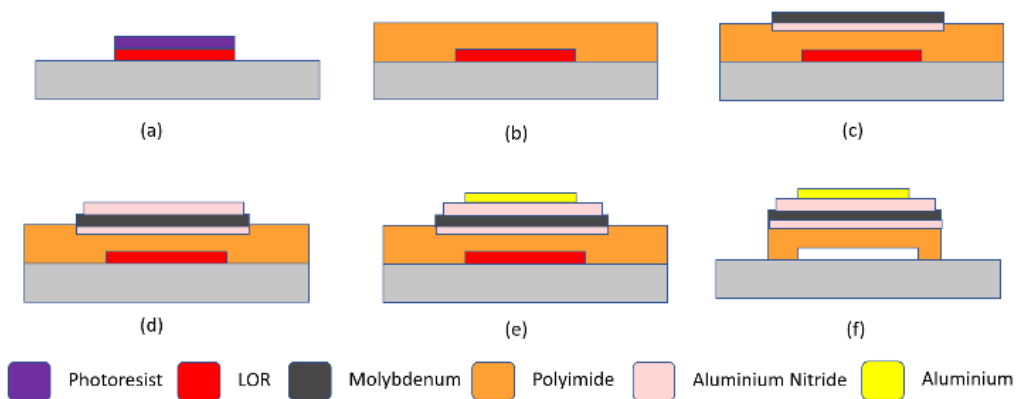
Figure 4.4: Fabrication protocol of the FBAR on the flexible membrane using an organic LOR sacrificial layer. a) Patterning of the sacrificial layer, b) covering with the protection layer, c) patterning of the bottom electrode, d) patterning of the piezoelectric.

4.4- Characterisation

Figure 4.5 details the fabricated resonator and its characterization. Figure 4.5a reports an optical microscope top-view of the fabricated device. The resonator structure has been analysed through its Scanning Electron Microscope (SEM) cross-section (Figure 4.5b).

The SEM microscope is an image acquisition system used to analyse structures with resolutions under 200-250 nm. With difference to a light microscope, SEM performs the acquisition exploiting electron beams. The electrons are generated by an electron source and pass through a system of lenses which focuses the particles on an electron beam centred on the sample. The interaction between the atoms of the sample and the emitted electrons produces back-scattering electrons, secondary electrons, and characteristics X-rays. All these signals are collected by detectors in the SEM chamber and are used to produce the acquisition. The dimensions of the electrons are much smaller than the wavelength of light sources, therefore with this system the resolution can reach very low values from 1 to 20 nanometres. Thanks to this system the internal structure of the resonator could have been analysed with a very high precision.

From Figure 4.5a it can be noted that the release of the membrane has been successfully obtained without affecting the other materials of the stack. Figure 4.5b illustrates the cross-section of the stack. The measured thicknesses of the layers are equal to 185 nm for the interlayer, 226 nm for the Molybdenum, 1.4 μm for the Aluminium Nitride, and 190 nm for the Aluminium. These values fall inside the maximum error range according to the Monte Carlo assumptions (maximum error equal to 5%).

The device has two ports in correspondence to the top and bottom electrodes and has been characterized using a Vector Network Analyzer (VNA, Anritsu MS46122B) and Ground Signal Ground (GSG) probes. Figure 4.4c shows the modulus and the phase of the impedance of the resonator. As it can be noted, the working frequency is equal to 2.545 GHz, belonging to the confidence interval estimated by the Monte Carlo simulation in Section 4.1.

Table 4.1 reports the comparison between the design parameters, the output of the algorithm and the experimental results.

	Design Requirements	The output of the Algorithm	Experimental Results
Piezoelectric thickness (d)	1.35 µm -1.5 µm	1.36 ± 0.07 µm	1.40 µm
Top electrode thickness (h)	-	180 ± 9.35 nm	190 nm
h/d	-	0.138	0.135
Resonant Frequency	2.550 GHz	2.550 ± 0.047 GHz	2.545 GHz

In terms of obtained thicknesses of the piezoelectric and top electrode layers, the measurements are in line with the design requirements and the output of the algorithm, which considered the fabrication tolerances. The resonant frequency falls into the 95% confidence interval evaluated by the design tool with an error of 0.02% for the design requirements.

From the antiresonance frequency at 2.601 GHz and using Equation 1.5 it is possible to measure the k^2_{eff} value equal to 4.7%, in line with the state of art. The Q-factor of the resonator has been evaluated using the Equation 1.6 reporting values of 1426 and 1467 for the resonance and antiresonance frequencies, respectively.
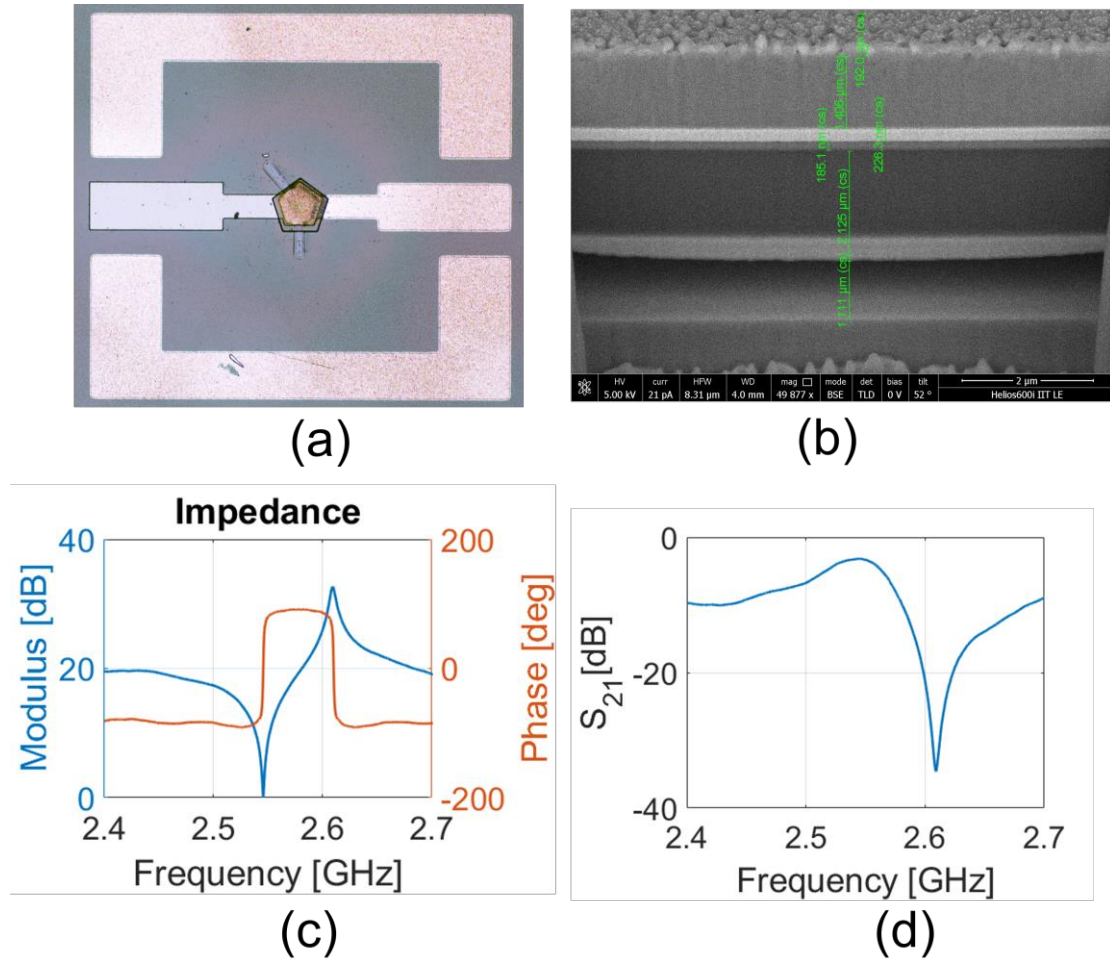
Figure 4.5: Characterization of the air-gap resonator. (a) Optical microscope top-view of the resonator, (b) SEM cross-section of the stack, (c) Measured Impedance of the resonator, (d) Scattering parameter S_{21}.

Table 4.2 reports a comparison between the design tool with the method already present in the literature. In addition, it reports a comparison of the proposed resonator to the state of the art in terms of different parameters: Quality factor (Q), Electromechanical coupling factor (k_{eff}^2), and Figure of Merit (FoM).

Table 4.2: Comparison between this work (T.W.) and the state of the art

Ref.	Design	Computational cost	Relative Error [%]	Scalability	Fabrication Tolerances	Q	k_{eff}^2	FoM $Q \cdot k_{eff}^2$
[86]	FEM	HIGH	N.A.	LOW	N.A.	1548	1	1548
[85]	FEM and ECA	VERY HIGH	N.A.	LOW	N.A.	2507	2.12	5314

[87]	FEM	VERY HIGH	0.2	MEDIUM	N.A.	59.8	4.1	245.18
[88]	FEM and deep learning	HIGH	0.2-0.3	HIGH	N.A.	N.A.	N.A.	N.A.
T.W.	Calibration Curves	LOW	0.2	HIGH	Yes	1467	4.7	6895

It results that the computational costs have been drastically reduced without affecting the relative error with this approach. Indeed, differently from the other design processes based on FEM models, the use of material calibration curves ensures faster and more lightweight simulation processes despite a contained relative error. The use of this approach makes the method highly scalable as new information can be easily added in form of curves. In addition to the state of the art, the very low computational cost allows the inclusion of fabrication tolerances exploiting Monte Carlo Simulations. Finally, thanks to the proposed fabrication protocol the FBARs can be obtained with a very fast and straightforward process with the highest product between Q-factor and k^2_{eff}.

Chapter 5- Filter Design Tool

A ladder structure is commonly adopted in thin-film bulk acoustic resonator or FBAR-based pass-band filters, because of its simplicity at the design and fabrication level. A ladder filter is composed of N resonators, connected in L-sections, which are formed by a series (labelled as "s") and a shunt (labelled as "p") resonator (see Figure 5.1a) [92].

(a)

(b)
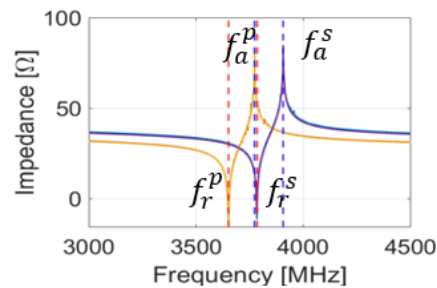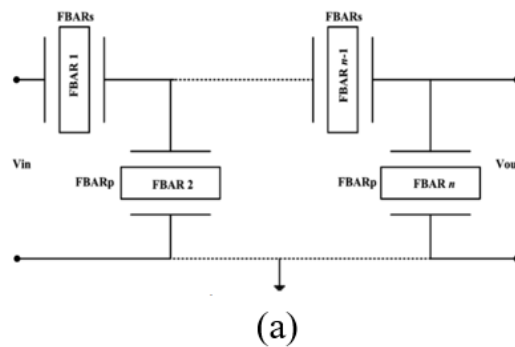
Figure 5.1: (a) Sketch of an N-order ladder filter. (b) Impedances of the series and shunt resonators of the single stage.

The working principle of a pass-band ladder-type filter consists of setting the resonant frequency of the series (f_r^s) near the antiresonant frequency of the shunt resonator (f_a^p) (see Figure 5.1b). The two resonators are matched to a specified load Z_0, typically equals 50 Ω. The higher the precision of the determination of the two resonant positions, the flatter is the pass-band response of the filter. The tuning of the resonators is extremely difficult, especially in the case of realistic stacks formed by stacked electrodes.

In this chapter, the design-tool introduced in the previous chapter has been applied for the fine-tuning of the series and the shunt resonators. The impedance matching

has been obtained using the closed form of the single-stage resonator static capacitances, reported in Reference [92], with optimal results. The procedure has been validated by the reverse engineering of the filter reported in [63] and then the effectivity of the method has been highlighted through the design of a new filter for sub-6GHz 5G filter, working at 3.77 GHz with a bandwidth of 200 MHz.

5.1- Main Algorithm

The filter design tool can be synthesized following the flowchart reported in Figure 5.2.
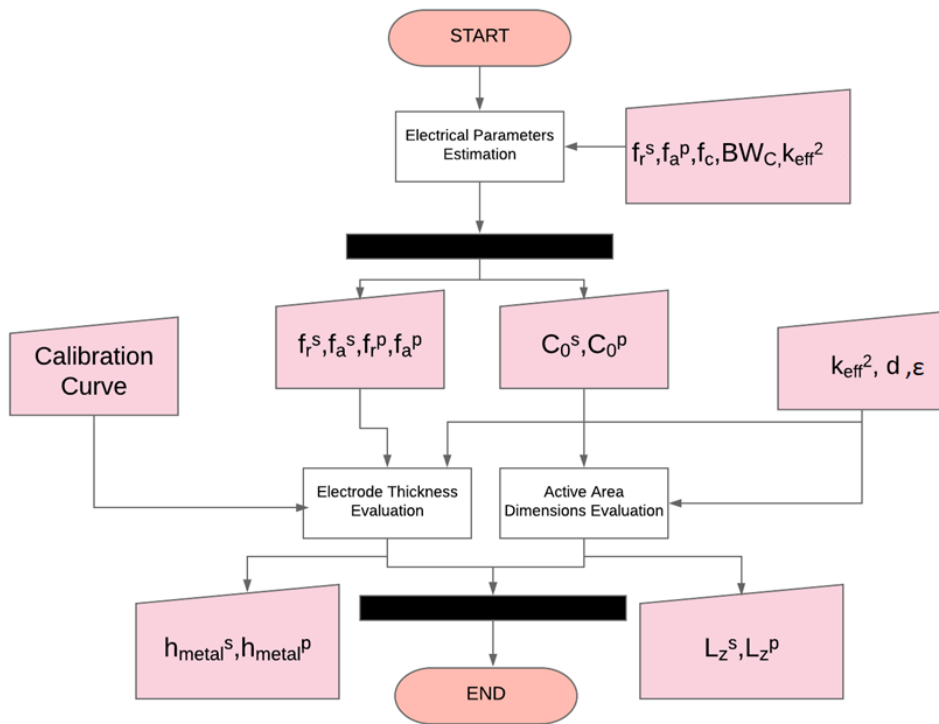
Figure 5.2: Flow-Chart of the ladder filter design tool.

The algorithm consists of the following steps:

Initialization: Specification of the functional requirements. The positions of upper and lower transmission zeros (f_r^p and f_a^s), the Out Of Band (OOB)-rejection level, the bandwidth (BW), the electromechanical coupling factor (k_{eff}^2) and the central frequency (f_c) is expressed,

Step 1: Estimation of the electrical parameters. This step is carried out by exploiting the method reported in Reference [93]. The frequencies f_a^s, f_r^p are evaluated starting from the positions of the transmission zeros (f_r^s, f_a^p) and Equation 1.3 for a given electromechanical coupling coefficient (k_{eff}^2); while the static capacitances (C_0^s, C_0^p) are obtained by solving Equation 5.1.

$$\begin{cases} C_0^s C_0^p = \dfrac{1}{(2 \cdot \pi f_c R)^2} \\[2mm] \dfrac{C_0^s}{C_0^p} = \dfrac{-f_i^4 + f_i^2 f_a^{p2} \quad + f_i^2 f_r^{s2} \quad - f_r^{s2} f_a^{p2}}{f_i^4 + f_i^2 f_a^{s2} \quad - f_i^2 f_r^{p2} \quad + f_a^{s2} f_r^{p2}} \end{cases} \tag{5.1}$$

where $f_i = f_c - \dfrac{BW_c}{2}$.

Step 2a: Evaluation of the metal electrode thickness.

The procedure starts from a guess of possible phase velocities which are used by the series resonator. The phase velocity of the series resonators is higher than the resonance of the shunts f_r^p and fixes the thickness of the piezoelectric layer, d, for both the single-stage resonators. The amount of metal in the shunt resonator is then determined so that the resonance of all the stack is at f_r^p.

This condition is satisfied by imposing a phase velocity v_p^p equals to:

$$v_p^p = 2d f_r^p \tag{5.2}$$

Therefore, the design algorithm provides the thickness through the calibration curve of the material forming the layer by finding the value of h/d corresponding to v_p as already explained in Section 4.1.

Step 2b: Estimation of the active area. The area (A) of the top electrode can be obtained by using Equation 5.3, for a given piezoelectric material with a specific dielectric constant (ε_r) and thickness (d).

$$C_0 = \frac{\varepsilon_r A}{d}; \tag{5.3}$$

5.2- Validation of the filter design procedure

We tested the proposed filter design tool through the design of an FBAR filter, where the input parameters have been obtained from the information detailed by the authors in Reference [63].

In particular, a bandwidth of 110 MHz, a 1.1 μm thick AlN layer and molybdenum for the piezoelectric material and electrodes respectively, have been imposed accordingly to the fabricated device.

The corresponding values for the electrodes reported by the decision core are 200 nm-thick molybdenum series mass-loaded with 30 nm of molybdenum, on the shunt resonators.

The N-order filter can be simulated with very high precision using a simulation utility that returns the filter response in terms of scattering parameters S_{21} and S_{11} through two steps: determination of the impedances of the L-section resonators and the analysis of the N-order filter by the transmission matrix method.

The steps constituting the simulation utility are synthesized in Figure 5.3.
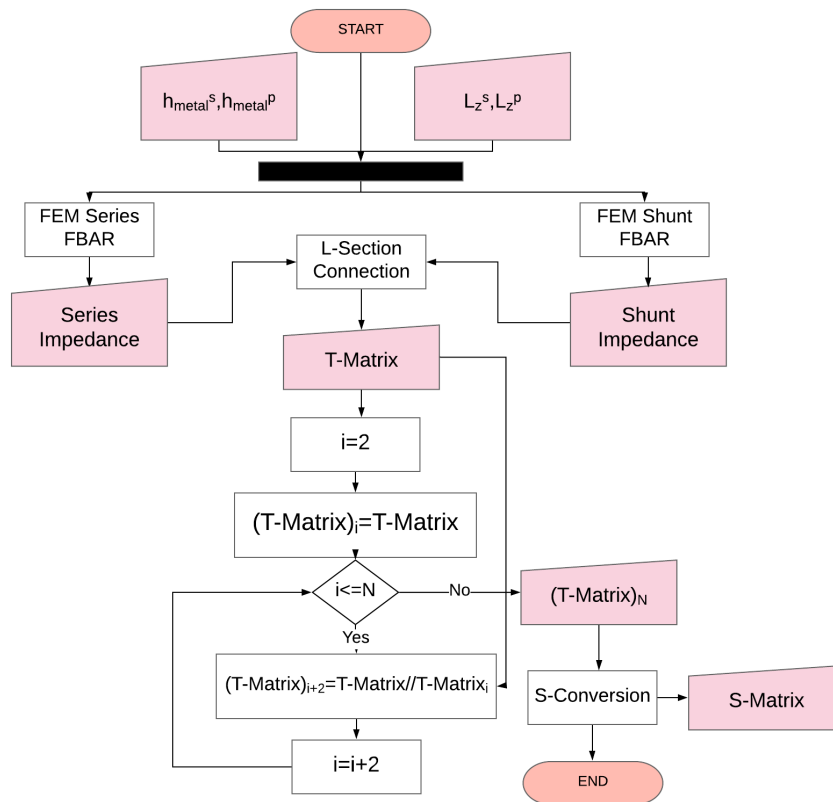
Figure 5.3: Flowchart of the Simulation Utility.

Single-stage Impedances. The geometrical parameters derived by the FBAR design tool have been used to build two FEM models of the single-stage resonators. In particular, we considered an attenuation factor for the AlN layer equal to 0.0002, a Rayleigh mechanical damping having α=68.8 s and β=2.82 × 10^{-14} 1/s whose values can be found in the literature [94]. We defined the molybdenum electrodes by using the following properties for the material: acoustic impedance= 64.16g/cm²s, density ρ= 10200 kg/m³, Young's modulus E= 3.12 × 10^{11} Pa, Poisson ratio ν=0.31. The edges of the geometry are terminated with fixed boundaries surrounded by Perfect Matched Layers (PMLs) [95]. The entire model is supposed to be a cross-section of the 3D device, with an out-of-2D plane extension equal to L_z. The simulated impedances of the two resonators are used to calculate the single-stage T-matrix utilizing the relations in Equation 5.4, where $Z_0 = 50\ \Omega$ and Z_1, Z_2 are the impedances of the series and the shunt resonators, respectively.

$$
\begin{cases}
T_{11} = \left(\dfrac{1}{2D}\right)(-Z_0^2 + QZ_0 - D), \\[2mm]
T_{12} = \left(\dfrac{1}{2D}\right)(-Z_0^2 + Z_1Z_0 + D), \\[4mm]
T_{21} = \left(\dfrac{1}{2D}\right)(Z_0^2 + Z_1Z_0 - D), \\[1mm]
T_{22} = (1/2D)(Z_0^2 + QZ_0 + D), \\
\quad\quad Q = (Z_1 + 2Z_2), \\
\quad\quad\quad D = (Z_1Z_2).
\end{cases}
\tag{5.4}
$$

Cascading and Conversion of T-Matrices. The order-N filter has been obtained by cascading N/2 single-stage T-matrices [96]:

Conversion in S-matrix. The N-order filter T-matrix is converted into the corresponding S-matrix [96] allowing to evaluate so the filter response S_{21} and the S_{11}.

The filter response and the impedances of the single-stage FBARs simulated by the simulation utility are presented in Figures 5.4a and 5.4b, respectively.

From Figure 5.4a it results a filter having a bandwidth of about 110 MHz and an insertion loss of -1.24 dB. The results are in-line with the Reference [63] (IL of -1.14 dB and a bandwidth of 107 MHz). In addition, two different configurations

with improved performances have been tested. The first is characterized by four FBARs and exhibits a lower insertion loss and a lower OOB-rejection level; while the second configuration is obtained by cascading six FBARs: achieving a higher OOB-rejection level than the one detailed by the authors [63].
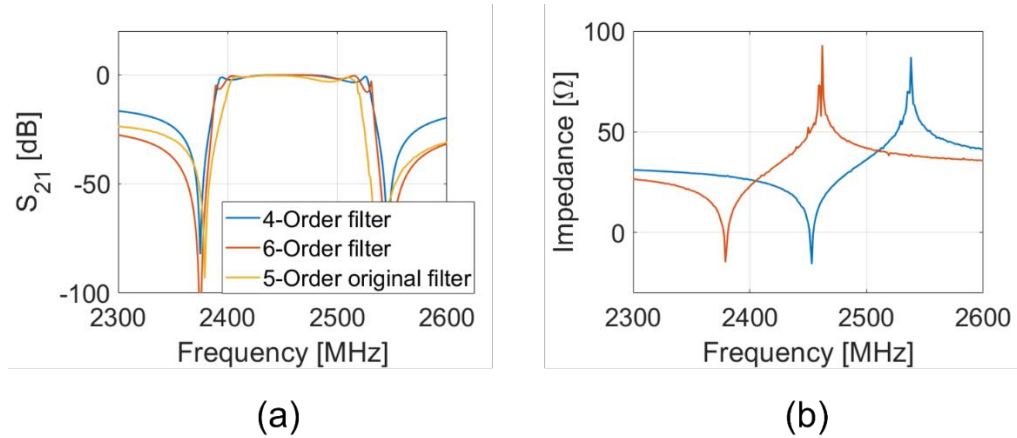
Figure 5.4 a) Scattering parameter S_{21} of the 5-order filter obtained employing the simulation utility, b) simulated impedances of the L-section FBARs, c) Inverse Design of the filter.

5.3- Design of the Flexible 5G Pass-Band Ladder FBAR Filter

In this section, the design of a filter having a central frequency located at 3775 MHz and a bandwidth of 190 MHz is reported. The input data to the filter design tool (Initialization) are: $f_a^s = 3900$ MHz, $f_r^p = 3650$ MHz, with a bandwidth of 200 MHz; while the chosen materials are aluminium for the electrodes and aluminium nitride as the piezoelectric layer ($\varepsilon_r = 9, k_{eff}^2 = 0.0758$).

The algorithm gave eight possible solutions reported in Table 5.1 and synthesized in Figure 5.5 which reports the values of the thicknesses of the piezoelectric layers versus the amount of metal for both shunt and series FBARs (Figure 5.5a.) and the height of the piezoelectric layer versus the longitudinal dimension of the electrodes, L_z (Figure 5.5b.).

As can be seen from Figure 5.5a, the range of the thicknesses of the aluminium varies between 150 nm to 220 nm to allow the possibility for the designer to choose the best set of geometrical parameters considering the technological constraint.

Table 5.1: Family of solutions of the pass-band filter.

N°	h_{piezo} [μm]	$h^s_{metal,1}$ [nm]	L^s_z [μm]	$h^p_{metal,1}$ [nm]	L^p_z μm
1	0.860	199	13.1	210	25.1
2	0.890	190	13.5	205	25.9
3	0.913	185	13.9	200	26.7
4	0.939	175	14.3	190	27.4
5	0.965	170	14.7	185	28.2
6	0.992	160	15.2	175	29.0
7	1.018	155	15.6	170	29.8
8	1.044	150	16.0	160	30.5

(a)   (b)
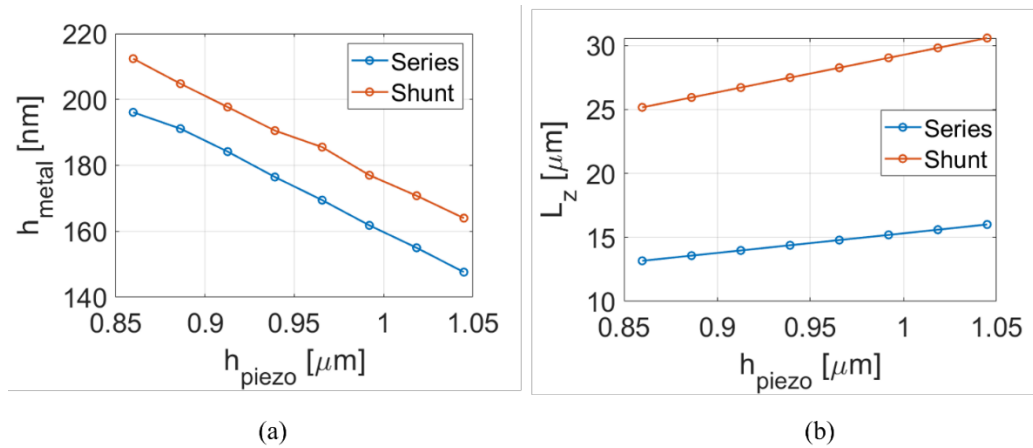
Figure 5.5: a) Electrodes thicknesses vs piezoelectric thickness, b) piezoelectric thickness vs the length of the electrodes.

The sixth solution has been chosen since it is easier to be fabricated because of the difference between the thicknesses of the electrodes (15 nm).

The FEM models of the L-Section FBARs consider the geometrical parameters reported in Table 5.2.

Table 5.2: Values of the geometrical parameters of the 2D FBAR model.

Parameter	Series resonator	Shunt resonator
h_{sub}	125 μm	125 μm

L	1000 μm	1000 μm
L_{top}	500 μm	500 μm
L_z	16.008 μm	30.580 μm
h_{top}	160 nm	175 nm
h_{piezo}	0.99 μm	0.99 μm
L_{PML}	50 μm	50 μm
h_{PML}	50 μm	50 μm

The resonators have been simulated simultaneously by exploiting a processor Intel i9-9900K and 64 GB of RAM. The total time required for the simulation process has been of about 7 minutes with a required RAM of 1.6 GB.

Figure 5.6a reports the impedances of the series (blue curve) and the shunt (red curve) resonators.

The resonant frequency of the series is at 3690 MHz and the anti-resonant frequency is at 3780 MHz.

The shunt resonator shows a resonant frequency of 3778 MHz and an anti-resonant frequency of 3868 MHz.

The impedances of the filter have been obtained as stated in Section 5.2 considering a various number of stages from 1 (N=1) to 4 (N=8).

Figure 5.6b shows the OOB-rejection level for different numbers of FBARs. It can be noted that all the configurations are characterized by a frequency response characterized of 195 MHz at 3775 MHz, hence perfectly suitable in our band of interest (the sub-6 GHz band in the 5G spectrum) and that the OOB level increases with the number of stages.

Figure 5.6c and Figure 5.6d. detail the scattering parameter S_{21} of the two extremes of the OOB levels, the 2-order filter (single-stage) and the 8-order filter, respectively.

The single-stage filter (Figure 5.6c.) presents an OOB-rejection level of less than -20 dB, while in Figure 4.6d the scattering parameter S_{21} of the 8-order filter, can

boast an OOB-rejection level of about -80 dB. The 8-order filter represents the best choice, due to the trade-off between a high OOB-rejection level and a contained number of resonators.
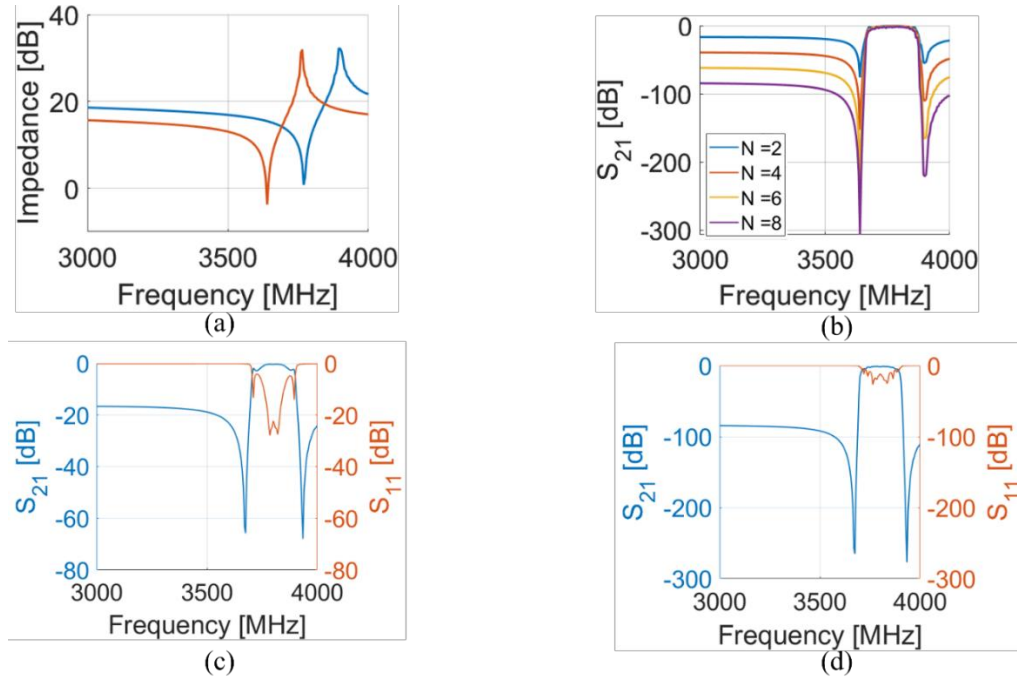
Figure 5.6: a) Impedances of the single-stage resonators, b) Scattering parameter S_{21} of filters having different order N, c) Scattering parameter S_{21} of the filter of a single-stage (N=2) filter, d) Scattering parameter S_{21} of the 8-order filter.

Table 5.3 compares the obtained values with the functional requirements.

Table 5.3: Comparison between Functional Requirements and output of the simulation utility.

	f_r^s [MHz]	f_a^p [MHz]	f_c [MHz]	$B.W.$ [MHz]
Input of the Algorithm	3690	3900	3775	190
Output of the simulation Utility	3690	3868	3779	190
Error [%]	0	0.8	0.9	0

The single-stage resonators designed thorough the algorithm present performance in-line with the initial requirements with an error of 0.8% on the resonant frequency of the shunt resonator. However, the response of the filter is perfectly in accord with

the initial requirements showing a 3dB bandwidth of 190 MHz and an error of 0.1% on the central frequency.

Chapter 6- FBAR on a Polymeric Substrate

In the literature, several works demonstrate the feasibility of AlN-based gravimetric sensing platforms. Indeed, thanks to their very high mass sensitivities, these resonators can be exploited for the development of a huge variety of sensors for antigen detection [97], [98], sweat analysis [31], or humidity [56]. In this scenario, the fabrication of flexible FBARs allows the development of highly sensitive sensing platforms for wearable and ingestible applications.

Reference [90] proposes the fabrication of FBAR on thin and flexible silicon substrates; however, the presence of air membranes under the active regions makes the structures fragile and the bendability of the thin silicon is not optimal for wearables. Another solution that speed-up the fabrication process is reported in [25] where the resonator is fabricated directly on a thick polyimide layer acting as a reflecting surface, eliminating the presence of membranes. The resonators present a good trade-off between performance and costs, but it has been fabricated using ZnO which is not suitable for UHFs.

In this chapter, we present the design and fabrication of AlN-based FBARs on a PI substrate and its use as a gravimetric sensor. In particular, the stack designed in the Chapter 4 has been applied for the fabrication of a flexible FBAR on a polymeric substrate.

The peculiarity of this device is the absence of an empty space under the resonating membrane through the use of a polyimide/molybdenum reflecting surface. Since the structure is not suspended, it differs from the initial assumptions of the design algorithm, therefore a supplementary study based on a FEM model has been performed, in addition to the design algorithm.

The fabrication has been performed using three lithographic processes obtaining optimal Q and electromechanical coupling factors. The sensitivity to the mass-loading has been proven by analysing the response of the device after the deposition of different layers of Polymethylmethacrylate (PMMA) with thicknesses from 250 nm to 650 nm.

6.1- Design of the resonator

Figure 6.1 details the design step of the resonator. The breakdown of the device components is detailed in Figure 6.1a.
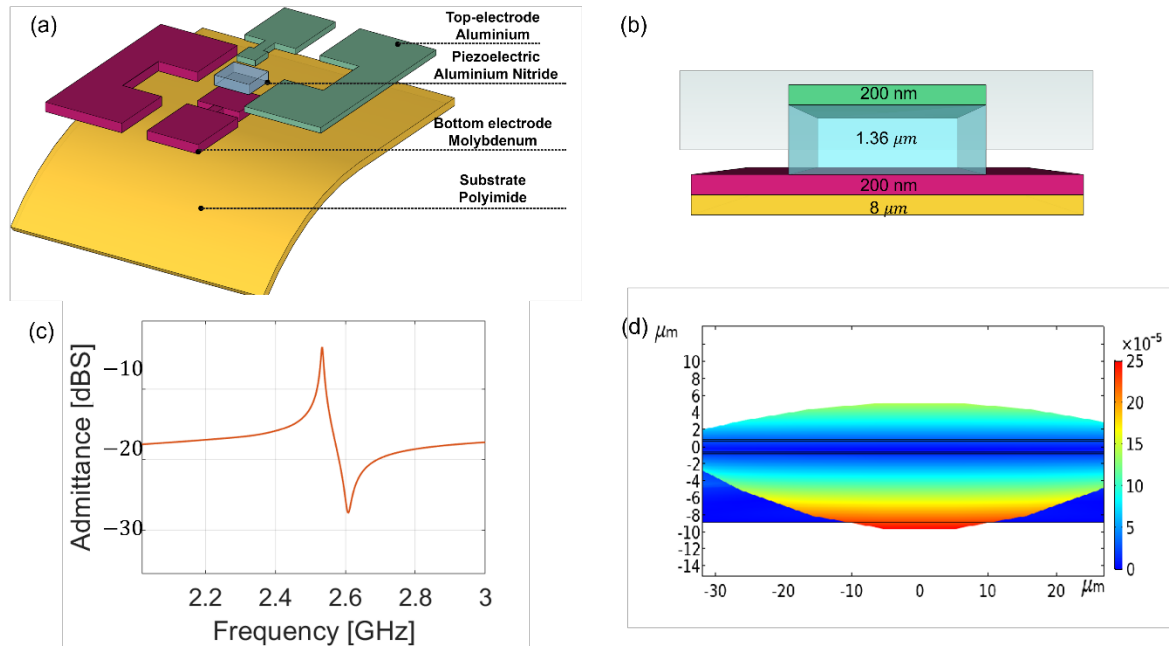
Figure 6.1: Numerical results: a) breakdown and b) cross-section of the resonator, c) simulated modal shape of the mechanical wave confined in the piezoelectric region, d) Simulated admittance versus frequency.

The resonator is formed by an AlN layer, an aluminium top electrode, and a molybdenum ground terminal. The thicknesses of the stack layers are reported in Figure 6.1b. The forming layers are an 8 µm thick polymeric substrate, 220 nm of Molybdenum for the bottom electrode, 1.36 µm of AlN for the piezoelectric layer, and 187 nm of Aluminium for the top electrode.

The presence of a polymeric substrate can have influences on the resonance of the device, shifting the resonant frequency designed through the algorithm. Therefore, a fine-tuning of the structure using a FEM model has been performed, accounts for the polymeric substrate. The signal of input has been applied to the top electrode while the ground is at the bottom. The domain has been truncated using perfectly matched layers surrounding the structure [58]. The geometry has been discretized using a mapped mesh with a minimum size equal to $\lambda/20$, where λ is the acoustic resonant wavelength. Finally, the mechanical and electrical responses of the

resonator have been evaluated using a frequency domain solver and Figures 6.1c. and 6.1d. detail the results of this study.

Figure 6.1c reports the admittance of the resonator in the range of interest. The device presents a clear resonance at the frequency of 2.55 GHz and an antiresonance at the frequency of 2.62 GHz. The modal shape corresponding to the resonant frequency is plotted in figure 6.1d. expressing the displacement of the piezoelectric material in the cross-section plane. As it can be observed, the mechanical deformation follows a longitudinal direction with a maximum at the top and bottom edges. A phase velocity of 6800 m/s can be estimated for the fundamental longitudinal mode, by using Equation 1.3.

6.2- Fabrication protocol

The fabrication process of the flexible FBAR is detailed in Figure 6.2.
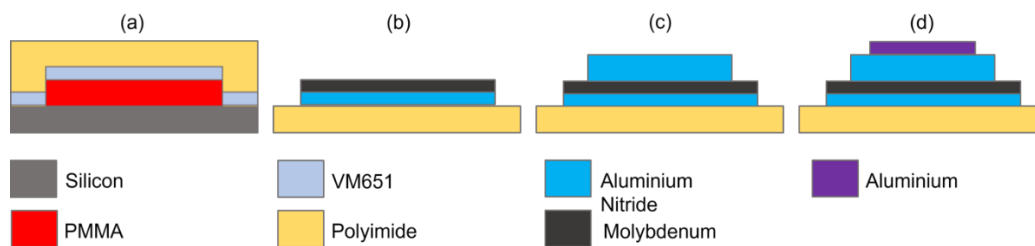
Figure 6.2: Fabrication Steps of the resonator.

As a first step, a PMMA sacrificial layer has been spin-coated on a donor silicon wafer. The role of the sacrificial is to allow the detachment of the polyimide substrate at the end of the process. The edges of the wafer have been cleaned from PMMA and an adhesion promoter (VM651) has been spin-coated and cured to reinforce the chemical bonding between polyimide and silicon. This step enables the formation of a barrier protecting the PMMA from solvent penetration between the PI substrate and the silicon wafer (see Figure 6.2a). Then, the polyimide has been spin-coated and cured. The recipes for the fabrication of the flexible substrate are fully detailed in Table 6.1.

	PMMA	PI
Spin Velocity [RPM]	1500	1500
1st Curing Temperature [°C]	180	130
1st Curing Time	2'	1h
2nd Curing Temperature	-	200
2nd Curing Time	-	2h

6.2.1- Interlayer, bottom electrode, and Piezoelectric layer

Figure 6.2b sketches the formation of the bottom electrode patterned using a top-down approach. More in specific, two sputtering depositions of a 185 nm thick AlN interlayer and 220 nm of molybdenum have been performed. After the deposition, the metal and the interlayer have been patterned by optical lithography and an ICP-RIE BCl$_3$-based.

The piezoelectric layer has been obtained using the same approach as the bottom layer. A 1.36 µm-thick AlN layer has been deposited through DC-pulsed sputtering deposition. Then, a positive mask has been obtained through optical positive lithography. The etching has been performed using ICP-RIE with gas concentrations of 45 sccm of BCl$_3$ and 20 sccm of Argon; and the resist has been stripped using Acetone, IPA and 5' of plasma oxygen (see Figure 5.2c).

6.2.2- Top-electrode and releasing of the structure

The top electrode has been fabricated using a bottom-up approach. Therefore, the structuring has not been obtained via the etching of the surface, but by the selective deposition of the material at sites which are not protected by a resist mask. In this case, the mask has been obtained using, inverse lithography. A 187 nm thick Aluminium layer has been deposited on the patterned resist mask. In the end, the metal attached to the resist has been delaminated by dipping the sample in a resist stripper, acetone in this case (see Figure 6.2d). The recipes for the deposition and the pattering of the stack of the resonator are reported in Table 6.2.

	Interlayer	Bottom	Piezo	Top
Sputter Deposition				
Base Pressure [mBar]	10^{-8}	10^{-8}	10^{-8}	10^{-8}
Power [W]	1000	200	1250	400
Time	8'30''	27'	46'	7'20''
Optical Lithography				
Spin Velocity [rpm]	-	2000	2000	2000
Temperature of Pre-Exposure Bake [°C]	-	110	110	110
Time of Pre-Exposure Bake	-	1'	1'	1'
1st exposure [mJ/cm^2]	-	140	140	100
Temperature of Post Exposure Bake [°C]	-	-	-	120
Flood Exposure [mJ/cm^2]	-	-	-	700
Developing Time	-	1'30''	1'30''	30''
ICP Etching				
Gas Concentrations [sccm]: BCl$_3$[1], Ar[2]	100[1], 25[2]	45[1], 20[2]	100[1], 25[2]	-
Time	5'	5'	25'	-

At the end of the fabrication process, the barrier around the PMMA layer has been removed by cutting the edges of the sacrificial layer with a blade; and the sample has been dipped in acetone until the complete detachment of the substrate.
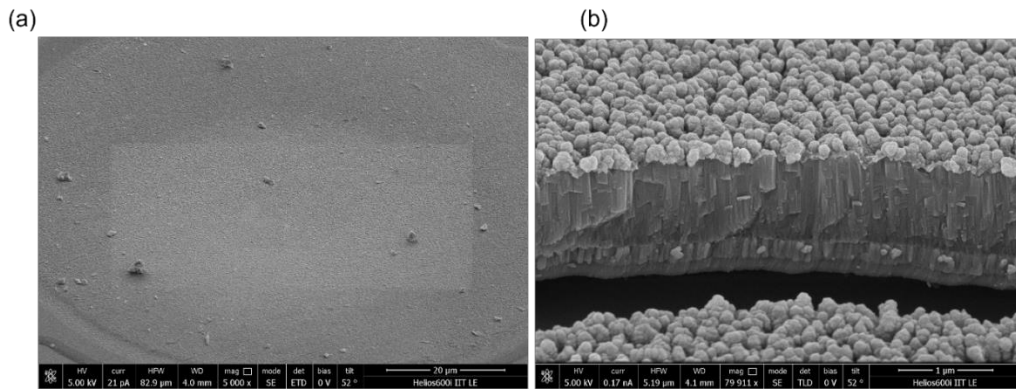
Figure 6.3: SEM Acquisition of the device, a) Top-view of the resonator, b) cross-section of the stack.

Figure 6.3 illustrates two Scanning Electron Microscope (SEM) acquisitions of the device. In particular, Figure 6.3a reports the top-view of the resonator. The stack has been patterned effectively as the surface shows a clean profile without any inhomogeneities. The cross-section of the stack is shown in Figure 6.3b. As it can be noted, the top-electrode surface is clean and without any discontinuity. The structuring of the stack has been effectively achieved as no additional materials between the layers, i.e., organic compounds or resist residuals, are present.

6.3- Characterization of the device

Figure 6.4 details an optical characterisation of the resonator. Figure 6.4a reports acquisition of the whole wafer with a zoom on a single resonator; as it is possible to note, the surface is flat despite a minimum residual tensile stress due to deposition and patterning processes. The footprint of the FBAR is about 950 μm x 700 μm considering the resonating area and the feeding lines. The fabrication process has been demonstrated to be very effective. The resonator shows bright aluminium and molybdenum metals without any oxidised areas. The substrate has withstood all the fabrication steps. The three lithography processes have been performed correctly as no alignment errors are evident.
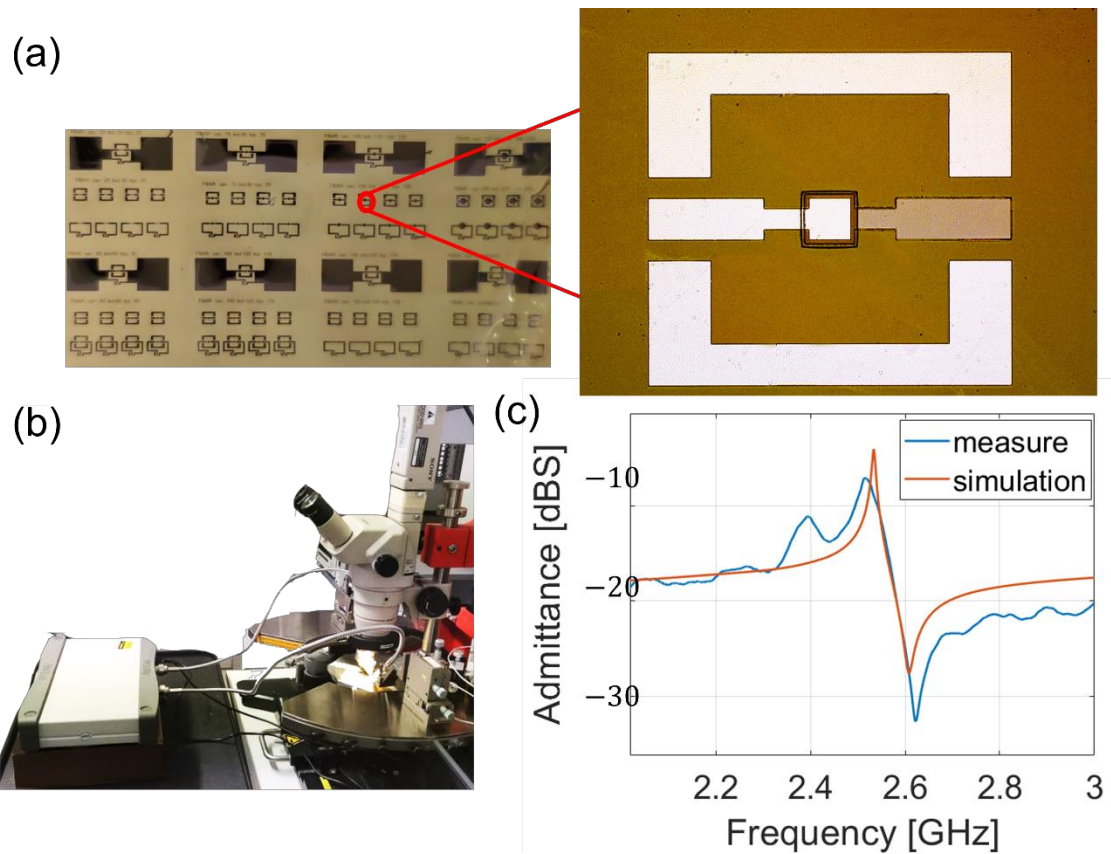
Figure 6.4: Characterization of the FBAR. a) detached wafer and zoom on a resonator, b) characterization set-up, c) comparison between the simulated (red curve) and the measured (blue curve) admittance of the resonator.

The FBAR has been electrically characterised in terms of admittance using a VNA and GSG probes (see figure 6.4b). The resonator has been treated as a two-port device, where the input port is the top, and the output port is the bottom electrode. The probes have been aligned to the feeding lines using a probe station with an optical microscope and connected to the VNA ports using SubMiniature version A (SMA) cables. The results are reported in figure 6.4c. There is a maximum of admittance at 2.55 GHz corresponding to the resonance, while the anti-resonance dip is placed at the frequency of 2.62 GHz. As it can be noted there is an optimal agreement with the FEM simulation although with a minimum error of 10 MHz between the resonance positions. The maximum and the minimum values of the admittance are higher in the simulated case because of losses introduced by the contact resistance. Moreover, the measure presents small oscillations which can be due to the bending of the cables when connecting the probes with the VNA. The resonators present a maximum quality factor (Q) and electromechanical coupling

factor (k_{eff}^2) of 218 and 6.0% respectively, evaluated as detailed in Equations 1.1. and 1.4. respectively.

Table 6.3 explain the advantages of this device with respect of the state of the art.

Table 6.3: Comparison of flexible FBARs.

	k_{eff}^2 [%]	Fabrication steps	Membrane	Substrate Material
[90]	3.1	8	Yes	Thin Silicon
[99]	3.1	5	No	Polyimide
[56]	5.1	8	Yes	PET
T.W.	6.0	5	No	Polyimide

As can be seen, the proposed resonator presents the highest electromechanical coupling factor combined with the lowest number of fabrication steps. In addition, the device is not suspended on membranes, therefore has a high robustness.

6.4- Mass Sensitivity

After the device characterization, the mass sensitivity of the resonator has been proven. Figure 6.5a shows the results of resonance frequency tuning in a range between 200 nm and 650 nm of PMMA spin-coated on the top of the FBAR. The more mass is deposited on the top electrode, the lower becomes the working frequency because of the mass-loading effect. Moreover, the addition of PMMA increases the dielectric losses of the resonator flattening the dip of the S_{21} and decreasing the electromechanical coupling factor.

Figure 6.5b reports the trend of the k_{eff}^2 in the function of the mass amount (m). The fitting of the anti-resonance frequency shift in the function of the PMMA mass amount has been evaluated in Equation 6.1.
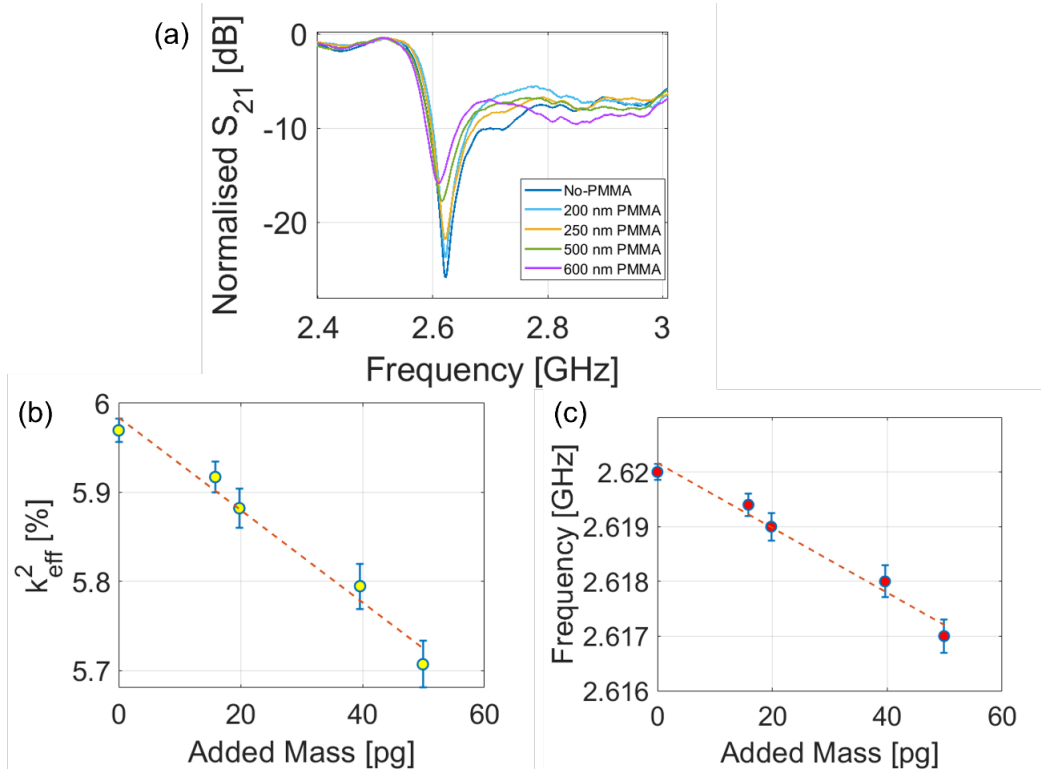
Figure 6.5: Mass-sensitivity of the FBAR. a) S_{21} for different PMMA amounts, b) k_{eff}^2 versus added PMMA mass, c) Frequency shift versus PMMA mass.

The comparison between the measurements and the polynomial fit is reported in Figure 6.5c.

$$f(m) = 2.62 - 23.31m \left[\frac{ppm}{pg}\right] \qquad (6.1)$$

The resonant frequency of the device presents a linear dependence with the added mass. This result is in accordance with theoretical expectations, indeed the adding of supplementary mass on the active area slows down the phase velocity of the mechanical wave travelling into the piezoelectric, because of the mass-loading effect and decreases the resonant frequency. The suitability of the device as gravimetric sensor with a sensitivity of 23.31 ppm/pg has been proved.

Chapter 7- FBARs on Polymeric air membranes

The main issue regarding the fabrication of FBARs on PI substrates is the maintaining of optimal performance. The presence of air under the electrodes enhances the reflectivity at the bottom interface and increases the Figure of Merit (FoM) of the resonators. A further strategy is the integration of several resonators working in parallel at the same frequency in the same device. In this chapter, the fabrication of flexible longitudinal mode FBARs based on polymeric membranes is treated. The resonators have been fabricated using the same dimensions as the previous chapters, but on a 50 μm-thick Kapton substrate and suspended on polymeric air membranes. In the first part, the fabrication of a single resonator is reported. Circular and hexagonal shapes have been analysed in terms of S_{21} scattering parameters.

7.1- Fabrication protocol

The resonator is composed of a 50 μm-thick Kapton substrate, a membrane support layer of polyimide having a thickness of about 2 μm, a 185 nm-thick AlN interlayer, a bottom electrode of 220 nm of molybdenum, a piezoelectric layer of 1.36 μm of AlN, and 200 nm of aluminium for the top electrode.

7.1.1- Sacrificial Layer

The Kapton substrate has been bonded to a silicon donor wafer through PDMS. This material is a two-part polymer formed of a base elastomer and a curing agent. The standard ratio is 1:10 and modifications of this ratio change the mechanical and chemical properties of the material [100]. The PDMS has been spin-coated on the silicon substrate at 1000 rpm for 60'. Subsequently, the Kapton substrate has been attached to the silicon substrate and kept under a strong vacuum for 30'. Then, the substrate has been cured for 1' at the temperature of 100°C. After, a PMMA layer has been spin-coated at 1000 rpm for 40'' and cured on a hot plate for 5' at the temperature of 180°C. The obtained thickness of the sacrificial layer has been

characterised using a profilometer. The results of this analysis are illustrated in Figure 7.1.
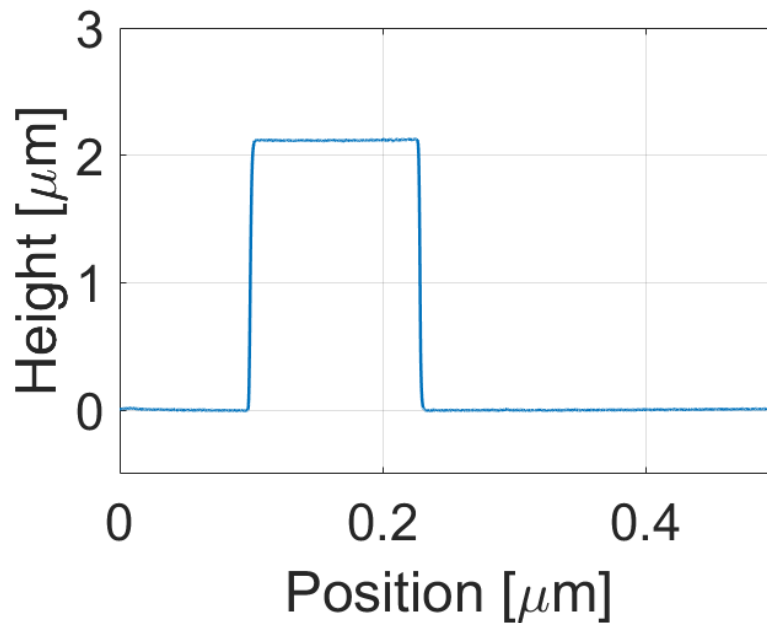
Figure 7.1: Vertical profile of the sacrificial layer.

It can be noted a flat surface of the sacrificial and a thickness of around 2 μm. The sacrificial layer has been covered using 2 μm of PI (PI-2555) protection layer. The PI has been spin-coated at 2000 rpm for 40''. The role of the PI is to protect the sacrificial layer from dissolution during the fabrication steps and to withstand the flexible structure after the releasing. A first curing process, to evaporate the solvents in solution with the polyimide, has been performed at 130°C for 1h30'. A second curing closes the chemical bonds of the polymeric layer and is performed at a higher temperature of 200°C for 1h.

7.1.2- Interlayer and Bottom electrode

The interlayer and the bottom electrode have been patterned using a top-down approach. In particular, 185 nm of AlN and 200 nm of Molybdenum have been obtained through sputtering deposition using the recipe detailed in the previous chapter. Then, a positive resist mask has been obtained by optical lithography.

Finally, the layers have been patterned using ICP-RIE and the resist has been stripped by dipping the sample in acetone, IPA and a plasma oxygen of 5'.

7.1.3- Piezoelectric layer

The piezoelectric region has been obtained using an approach similar to the bottom electrode. The deposition of 1.36 μm of AlN has been performed using sputtering deposition, then the surface has been covered with a positive resist mask and etched using ICP-RIE. The mask resist has been removed at the end of the process by dipping the sample in acetone and IPA and using a plasma oxygen of 10'.

7.1.4- Top-electrode

The top electrode has been fabricated using a lift-off procedure. A negative resist mask has been obtained through optical lithography. The deposition of 200 nm of aluminium has been performed using a sputtering deposition. Finally, the top-electrode has been obtained by removing the negative mask by dipping the sample in acetone.

7.1.5- Releasing

At the end of the patterning of the stack, the polyimide protection layer has been patterned using a negative resist mask in order to open some holes as inlets of a microfluidic channel localised underneath the resonators for the etching of the PMMA sacrificial layer and achieve the empty space for vibrations. The polyimide layer has been etched by ICP-RIE O_2-based for 2' and the sacrificial has been dissolved by dipping the sample in acetone. The combined device and the single resonator are illustrated in Figures 7.2a and 7.2b, respectively.
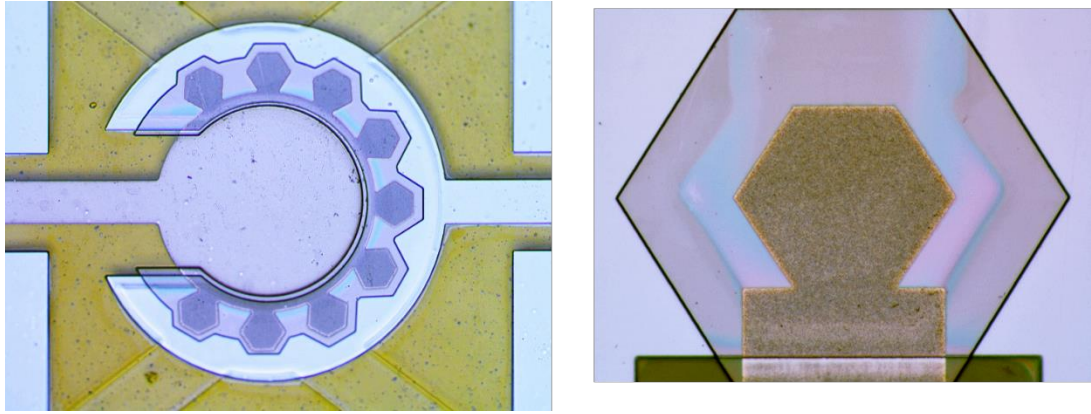
Figure 7.2: Flexible FBARs on polymeric air membranes, a) combined device, b) single resonator.

7.2- Low-Frequency Characterisation

The device has been characterised at low-frequencies in terms of conductivity of the metal trace and static capacitance using an LCR- meter. In particular, the wafer has been placed on a probe-station and the electrical capacitance and the Q-factor have been evaluated by placing two-needle probes on the top and the bottom electrode using an optical microscope. The probes have been connected to the LCR meter using Bayonet Neill–Concelman (BNC) connectors. The same analysis has been performed both for a single resonator and the combined device. Table 6.1 reports the values:

Table 7.1: Low-frequency characterization of the resonators.

Device	C_s	Q-factor
Single Resonator	1.07 pF	11.53
Combined Device	10.05 pF	222

As it can be observed, the single resonator shows a static capacitance that is approximately close to one nineth of the combined device, perfectly in line with expectations. It is possible to conclude that all the resonators integrated into the combined device have been connected correctly. Moreover, the Q-factor of the devices demonstrates an optimal conductivity of the electrodes as a very low value of series resistance is observed in both configurations, where the single resonator

has a value of 0.09 pΩ and the combined combination has a lower value of 0.045 pΩ.

The resistance of the device is given by the sum of the contribution of the single resonators and the areas of the exciting common electrodes. The circuit is formed of nine capacitors in parallel with nine resistors.

The total capacitance is given by the sum of the single contributions of the capacitors and the equivalent resistance is given by equation 7.1.

$$R = \frac{1}{\frac{1}{R_1} + \frac{1}{R_2} + \cdots + \frac{1}{R_9}} = \frac{\frac{1}{9}}{R} = \frac{R}{9}$$

(7.1)

The effect of the exciting common electrode is to increase the resistance of the system and can be evaluated considering Equation 6.2.

$$R_c = A\rho$$

(7.2)

The area of the common electrode is about three times larger than the one of the single devices (51000 μm² vs 155000 μm²). Therefore, the resistance of the combined system can be approximated as in Equation 7.3.

$$R = R_i + R_c = \frac{R}{9} + 3R \cong 3R$$

(7.3)

In conclusion, while a slightly higher resistance value for the combined systems has been measured, the capacitance is exactly nine times the one of the single resonators. As a consequence, the combined configuration enhances the Q-factor by about 20 times concerning the single device. By reducing the dimension of the common electrodes this result can be even improved.

7.3- High-Frequency characterization

The resonators have been characterised in terms of the S_{21} scattering parameter using a VNA, GSG probes and a probe station. The probes have been aligned with the pads using micrometric screws and an optical microscope.

The results are illustrated in Figure 7.3.
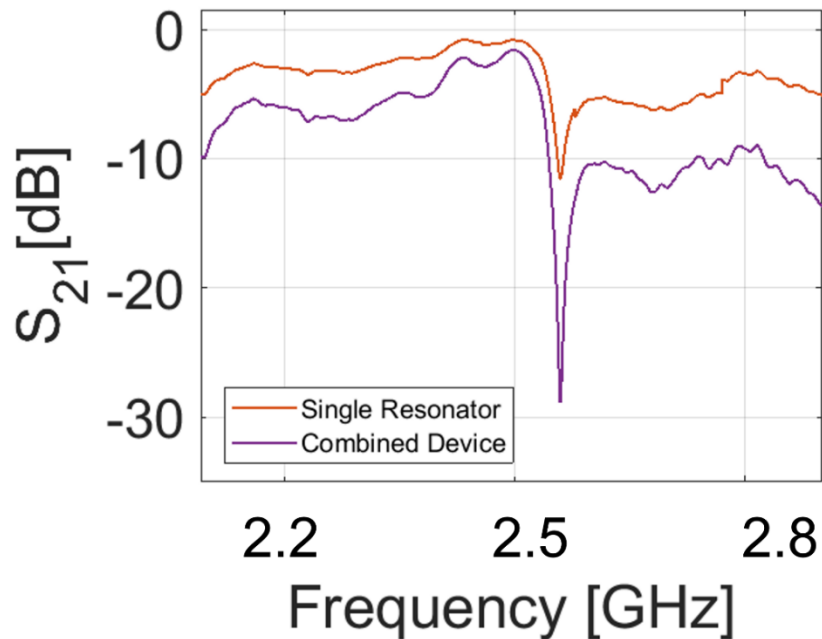
Figure 7.3: Scattering parameters of the single resonators and the Combined Device.

As it can be noted the resonant frequency of the devices is at the same value of 2.500 GHz and the antiresonance is at 2.565 GHz.

The electromechanical coupling factors of the single and the combined devices are equal to 6.0%. Moreover, as was expected from the low-frequency analysis, the Q-factor of the combined device is significatively higher than the single resonator reporting values of 742 and 260 respectively.

Chapter 8- Flexible Complementary Split Ring Resonator

CSRRs offer an optimal trade-off between performance, footprints and costs [101]–[103]. Their integration with Radio Frequency Identification (RFID) can open the door to a new generation of high-sensitive RFID sensors. However, their low sensitivities, related to low Quality-factors (Q-factors), when in contact with fluids are an extremely important issue to solve.

Reference [104] details a CSRR applied for the analysis of fluids; however, the sensor is not submersible as the liquids flow in a capillary tube. Moreover, the Q-factor of the device has a very low value of 35. Another example is reported in [17] where the sensor is implemented using a CSRR on the ground plane of a microstrip and the sensitivity of the device to the liquid under test is incremented using a PDMS coil-shape microfluidic channel. Even if the reported value of sensitivity is extremely promising (0.98%); the sensor is neither flexible nor submersible, therefore is not suitable for wearables. Moreover, the fabrication of the PDMS channels requires additional steps for the patterning and the alignment of the microfluidic to the CSRR. In reference [16], a device having a higher Q-factor has been designed by combining two resonators; however, also in this case, the sensor is not suitable to be immersed. In Reference [18], two M-CSRRs are used. In this case, the Q-factor in the air is 937, however, after the dipping in fluids, the value becomes very low as the magnitude of the S11 dip becomes lower than 10 dB and the sensitivity of the sensor has not been evaluated when submersed. Furthermore, the sensor is extremely sensitive to the height of the fluid as even 1 mm of variation of this parameter affects enormously the resonant position. In addition, none of these works is based on planar geometries and cannot be easily adapted to flexible substrates.

The use of planar geometries speeds up the fabrication processes, as only one single metallic stripe is necessary, without the need of realignment. In contrast, grounded microstrips imply thicker stacks and ground metallic bottom layers reducing the flexibility of the substrate [105]. An alternative solution is proposed in [106] where the sensor is formed of a ring resonator coupled with a coplanar microstrip line, but the position of the liquid needs to be carefully controlled as the sensing principle is

based on the capacitance change of the gap between the resonator and the microstrip. Therefore, the sensor cannot be dipped in fluids. Moreover, the device presents very low Q-factors and sensitivities of 42 and 0.27%, respectively; and a large footprint of 40 x 8 mm^2. Furthermore, the sensor is not suitable for wearable applications as is formed of a rigid substrate with a suspended microfluidic channel. A flexible planar resonator is proposed in Reference [107], where a CSRR on a 125 μm-thick PEN is presented. However, the device reports a very low Q-factor of 35.1 and it has not been applied for fluid analysis. Finally, reference [108] details a chipless RFID tag based on CSRRs; however, the footprint is very large (almost 50 x50 mm^2 at 1 GHz). In addition, misalignment and fabrication tolerances have introduced errors in the response of the device; and the operation in submersed environments has not been proven.

In this chapter, we propose an innovative sensor based on two CSRR excited with a coplanar microstrip line, based on a 200 μm-thick Kapton substrate and fabricated using a multi-material 3D printer. The use of a 3D printer has allowed a very precise fabrication process in the field of coplanar microstrip line with a minimum shift between simulations and measurements. Moreover, the process is characterised by the high repeatability of the devices and by a very big yield of a maximum of 48 resonators printed in less than 2 hours.

Differently from the state of the art, this device works efficiently in the 800 MHz RFID band in water and at 4.6 GHz (suitable for the Internet of Things [109] or sub-6GHz 5G [110], [83]) when in air. The performance of the resonator demonstrates its suitability for wearable or ingestible scenarios. Indeed, the sensor in the air presents a Q-Factor of 702 and good sensitivity to water droplets with a value of 0.33% μl^{-1}. In the water, the device reports the highest Q-factors in liquids (501) and extremely high sensitivities to temperature (0.5% $\circ C^{-1}$) and dielectric variation (1.5%). The flexibility combined with a very compact footprint of 24 x 18 mm^2 (0.06 λ x0.05 λ, where λ is the electrical wavelength at the frequency of 800 MHz); makes this device an optimal choice for ingestible and wearable applications.

8.1- Design process

Figure 8.1.a sketches the geometry of the sensor. In particular, the device is composed of a two-sections coplanar microstrip line with two CSRRs placed in its centre (Figure 8.1a). The widths of the microstrips (w_{m1}, w_{m2}), are constrained by the footprint of the connector and the diameter of the CSRRs, while the gaps g_{m1} and g_{m2} have been designed to achieve an input impedance of 50 Ω.

The CSRR has been treated as an LC-circuit having a resonant frequency determined using Equation 8.1.

$$f_r = \frac{1}{2\pi\sqrt{L_0 C_c}} \qquad\qquad (8.1)$$

where L_0 and C_c are the inductance and capacitance of the resonator, respectively. The radius and the gap of the CSRRs (r_{csrr}, g_{csrr}) have been chosen to obtain a resonant frequency at 850 MHz when dipped in water.

Then, the second CSRR has been designed at the same frequency to enhance the Q-Factor of the device.

Figure 8.1b sketches the vertical cross-section. The substrate is a 200 μm-thick Kapton (h_k) with a dielectric constant of 3.8 and a loss-tangent equal to 0.002. On the top of the flexible substrate, there is a thin dielectric adhesion layer with a thickness equal to h_d having a dielectric constant of 2.9 and loss-tangent of 0.002 and a metallic layer of 35 μm (h_m). The corresponding values of the geometrical parameters are detailed in Table 8.1.

Table 8.1: Geometrical parameters of the sensor.

Parameter	Value
w_{m1}	*5.00*
w_s	*0.75*
l_s	*23.70*
g_{m1}	*0.5*
g_{m2}	*0.3*

w_{m2}	8.40
l_{m2}	15.3
r_{csrr}	3.70
g_{csrr}	0.3
l_x	7.40
h_m	0.035
h_d	0.003
h_k	0.2
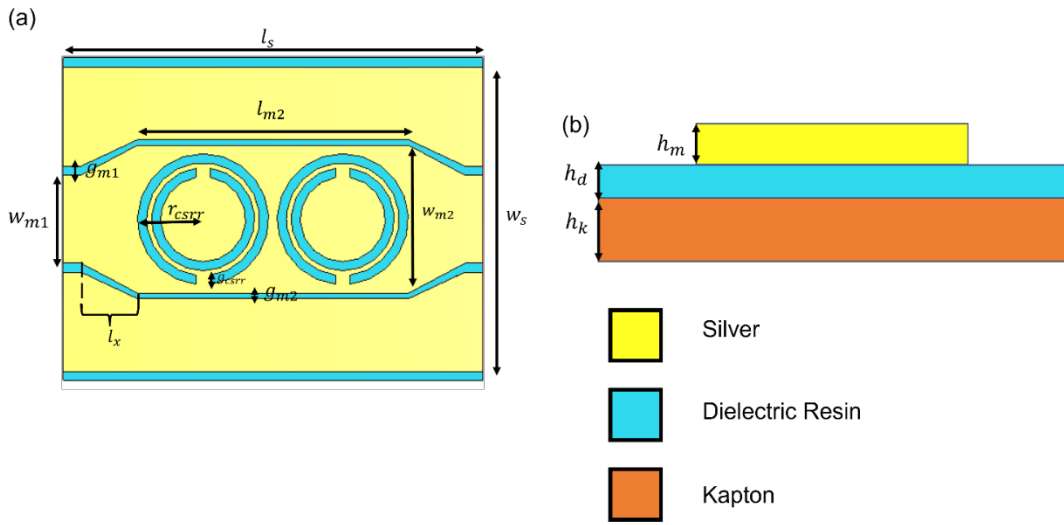
Figure 8.1: Geometry of the sensor: a) top view with respective geometrical parameters, b) front view with geometrical parameters.

The response of the sensor has been simulated by solving the Maxwell's equations in the time domain through a FDTD-based commercial software. The surrounding medium of the device has been supposed having the dielectric properties of deionised water at various temperatures and the relative dielectric constants have been obtained varied using Equation 8.2. [111]:

$$\varepsilon_r = 78 \left(1 - 0.00461(t - 25) + 1.55(t - 25)^2 \cdot 10^{-5}\right) \tag{8.2}$$

The simulated scattering parameter S_{11} has been evaluated and the result is detailed in Figure 8.2.
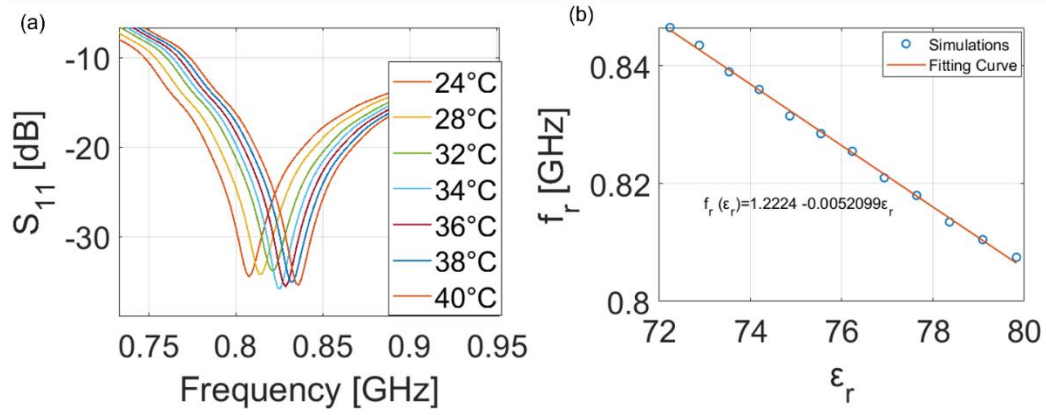
Figure 8.2: Design of the M-CSRR: a) Scattering parameter S_{11} evaluated for different water temperatures, b) trend of the resonant frequency versus the dielectric constant of the water.

The higher the temperature, the higher the working frequency of the resonators and the resonant position of the sensor is always contained in the 800 MHz RFID band for all the temperatures under test (24°C – 45°C). The trend of the resonant frequency (f_r) versus the value of the dielectric constant (ε_r) is reported in Figure 8.2b. The simulated values have been interpolated using a polynomial function of degree one having expression in Equation 8.3.

$$f_r = 1.224 - 0.0046\varepsilon_r \tag{8.3}$$

The sensitivity of the sensor (S) can be evaluated as reported in Equation 8.4.

$$S = \frac{df}{d\varepsilon_r}\left(\frac{1}{f_0}\right) \cdot 100 = \frac{0.0046}{0.8} \cdot 100 = 0.56\% \tag{8.4}$$

Figure 8.3 shows the response of the resonators when in air, in terms of scattering parameter S_{11} and impedance.
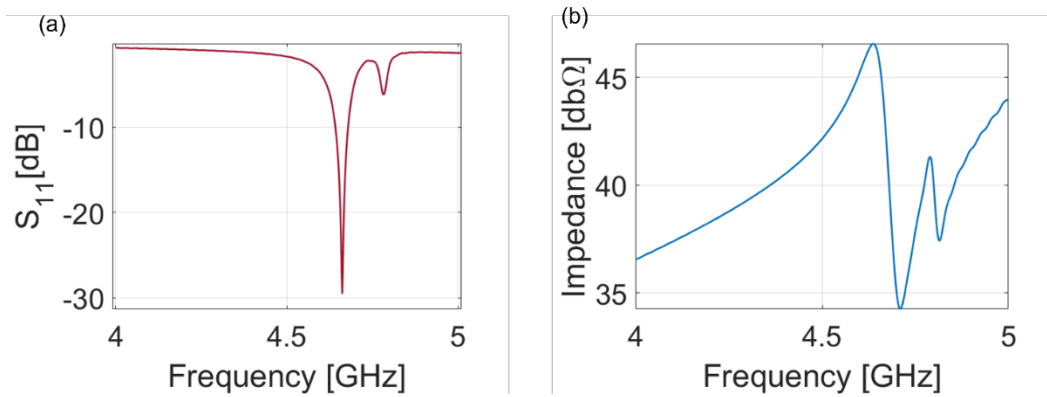
Figure 8.3: Simulated frequency response of the M-CSRR when in air condition.

As it can be noted the device works properly at a frequency of 4.64 GHz with a dip of about -30 dB.

The impedance reports a clear maximum at the resonance and a minimum at the antiresonant frequency of 4.71 GHz.

8.2- Fabrication

The device has been fabricated using silver nanoparticle-based ink deposited using a multi-material 3D printer (Nano dimensions Dragonfly) where a dielectric interlayer of 35 μm has been deposited on the Kapton substrate to reinforce the adhesion with the metal.

The planar geometry of the resonator is ideal for a rapid printing process; a process yield of nine resonators printed in less than 2 hours has been obtained. In general, the total printing area of the machine is 50x50 cm^2 therefore a maximum of 48 resonators can be achieved. The resonator has been cut, connectorized and passivated using 1.02 gr. of parylene-C deposited using CVD (corresponding to a layer of a thickness of 1 μm). The printed sheet containing 9 devices and the obtained sensor, are shown in Figures 8.4a and 8.4b, respectively.

The resonators have been characterised in terms of scattering parameter S_{11} using a VNA and an SMA rigid cable. Figure 8.4c. compares the measured S_{11} with the simulated values. The sensor works properly at the frequency of 4.66 GHz and presents a dip of the S_{11} equal to about -25 dB. As it can be noted there is an optimal agreement with the simulated model with a minimum shift of a few Megahertz due

to fabrication tolerances; the dielectric interlayer has not influenced the flexibility of the substrate.

It is possible to also note a lower magnitude of the scattering parameter S_{11} dip in the measurements, due to the effect of the soldering and a lower conductivity of the metal because of the presence of solvent mixed with the silver nanoparticles.
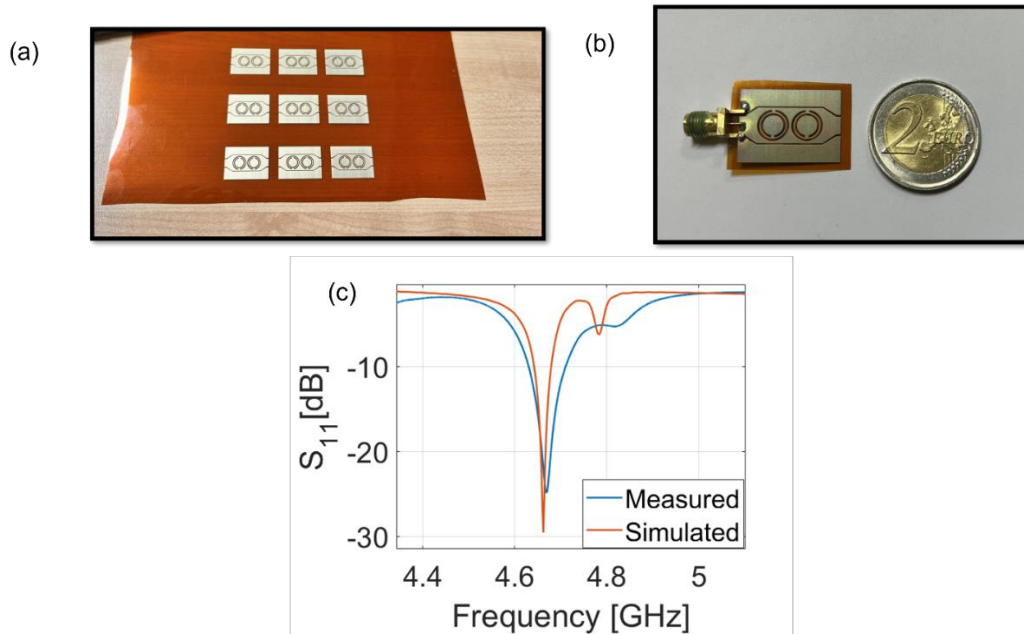
Figure 8.4: Fabrication and characterisation; a) Result of the printing process, b) Single resonator, c) comparison between the simulated and measured scattering parameter S_{11}.

8.3- Air sensitivity

The device has been developed to work in humid air environments, such as the skin and liquid environment, i.e., the inner of the human body. To prove the effectiveness of the device in two cases, the sensitivity to water droplets has been analysed in the air, while, in water, the influence of the temperature on the frequency response has been exploited.

When attached to the skin, the sensor is constantly exposed to sweat droplets which influence the frequency response and can be analysed to extract important information. The sensitivity of the sensor to the water droplets has been tested by measuring the scattering parameter S_{11} after the deposition of volumes of deionised water ranging from 0.3 µl to 9.6 µL. The results are reported in Figure 8.5.

The sensor has been connected to a VNA in a self-standing configuration as shown in Figure 8.5a the droplets have been aligned at the centre of the left CSRR using a microliter pipette.
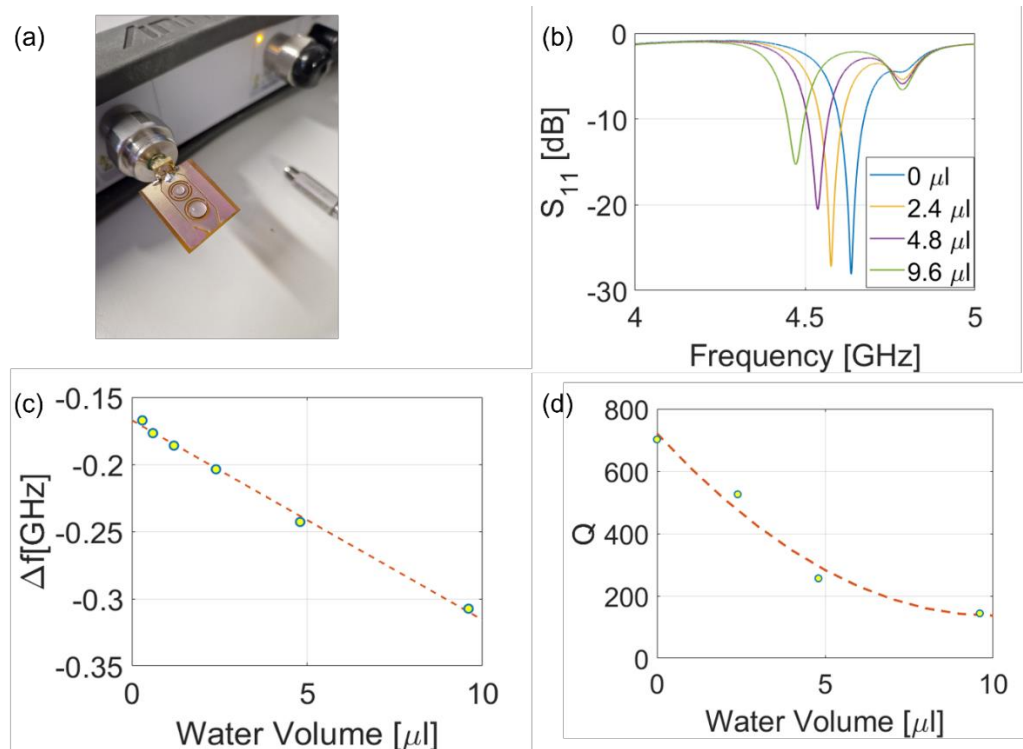
Figure 8.5: Water Droplet sensing mechanism a) Characterization set-up, b) Scattering parameter S_{11} measured for different water droplets having variable volumes, c) Resonant frequency versus water volume, d) Q-factor versus water volume.

As can be seen from Figure 8.5b, the sensor shows two resonant dips, one at 4.7 GHz and a second varying with the amount of water placed on the first CSRR leaving the right resonator unexposed to exploit the sensor in differential mode. It can be noted that the more the water volume, the higher becomes the distance between the dips, the lower the Q-factor of the first dip. The trend of the distance between the resonant dips versus the volume of deionised water is reported in Figure 8.5c. It is worth stressing that the relationship between the water volume (V) expressed in Microliters (μL) and the differential frequency (Δf) is linear.

The experimental points have been interpolated using a fit curve having the expression in Equation 8.5.

$$\Delta f(V) = -0.16718 - 0.014861 \cdot V \qquad (8.5)$$

The sensitivity of the device has been derived using equation 8.6.

$$S = \frac{\frac{d\Delta(f(V))}{dV}}{f_0} \cdot 100 = 0.3\% \, \mu l^{-1} \qquad (8.6)$$

As can be observed from Equation 8.6, the size of the droplets not only affects the resonant position but also the Q-factor. Indeed, there is an inverse relationship between the Q-factor and the sizes of the water droplets because of an increase in dielectric losses.

The relation between Q and the water volume has been evaluated using a fitting curve having expression reported in Equation 8.7.

$$Q(V) = 721.3124 - 116.877V + 5.8434V^2 \qquad (8.7)$$

8.4- In-Water Sensitivity

The human body is made of 60% of water, therefore an ingestible sensor needs to work properly when dipped in liquids. The characterization in water has been performed using a VNA and a PET container filled with deionised water.

The sensor has been dipped in water and connected to the VNA with an SMA rigid cable; the temperature of the water has been varied using a hot plate set at a fixed temperature of 100°C.

The scattering parameter S_{11} of the sensor has been recorded periodically and referenced to a specific temperature using a thermometer.

Figure 8.6 reports the results of this study. In Figure 8.6a. the comparison between the simulations and the S_{11} of the device when dipped in the water at 36°C is reported. There is an optimal agreement between measures and simulated data with a resonance dip at 840 MHz. The baseline of the measure is slightly lower than in the simulations because of the bending of the cable and a higher value of the dielectric losses of the water. Figure 8.6b illustrates the result of the analysis performed for all the temperature ranges. As it can be noted, the resonant frequency

increases with the increase in temperature. Figure 8.6c illustrates the trend of the resonant position versus the temperature (T. The points have been fitted using a two-degrees polynomial function whose expression is reported in Equation 8.8.

$$f_r(T) = 0.82538 + 0.0028486T + 8.3348 \cdot 10^{-5}T^2 \qquad (8.8)$$

It is worth stressing that increasing the temperature reduces the dielectric losses of the water, sharpening the dips of the S_{11} and increasing the Q-factor of the resonator.
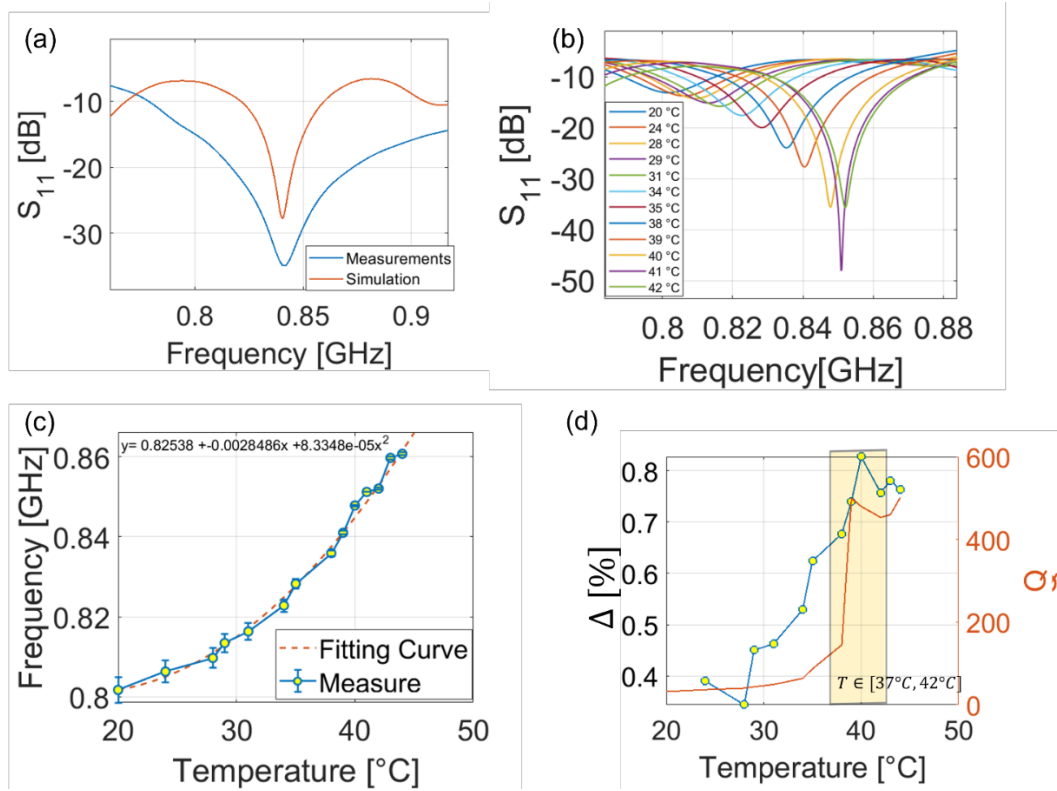

Figure 8.6: In water Temperature sensor, a) comparison between simulations and measurements, b) Scattering parameter S_{11} for different water temperatures, c) Frequency versus water temperature, d) Sensitivity and Q-factor versus water temperature.

The sensitivity of the sensor has been evaluated in all the temperature ranges to analyse the influence of the Q-factor on the response of the device. The percentage variation of the resonant frequency ($\Delta(T)$) has been obtained for each temperature as in Equations 8.9,8.10,8.11.

$$\Delta(T) = \frac{\Delta f(T)}{f_0} \cdot \frac{1}{\Delta \varepsilon_r(T)} \cdot 100 \qquad 8.9$$

$$\Delta f(T) = f_r(T) - f_0 \qquad 8.10$$

$$\Delta \varepsilon_r(T) = \varepsilon_r(T) - \varepsilon_r(20°) \qquad\qquad 8.11$$

where f_0 is the resonant frequency when the water temperature is at 20°C and $\varepsilon_r(t)$ has been evaluated using Equation 8.2.

The trend of Δ and Q concerning the temperature have been compared in Figure 8.6d. The trends of Q and Δ are fully in accord and two separate regions of the sensors can be distinguished where the human-body temperature range reports higher sensitivities. The mathematical expressions of the calibration curves are reported in the system of Equations 8.12.

$$f(t) \qquad\qquad (8.12)$$
$$= \begin{cases} 0.8 + 0.18T, & 20°C \leq T < 35°C \\ 0.823 + 0.5T, & 35°C \leq T < 42°C \end{cases}$$
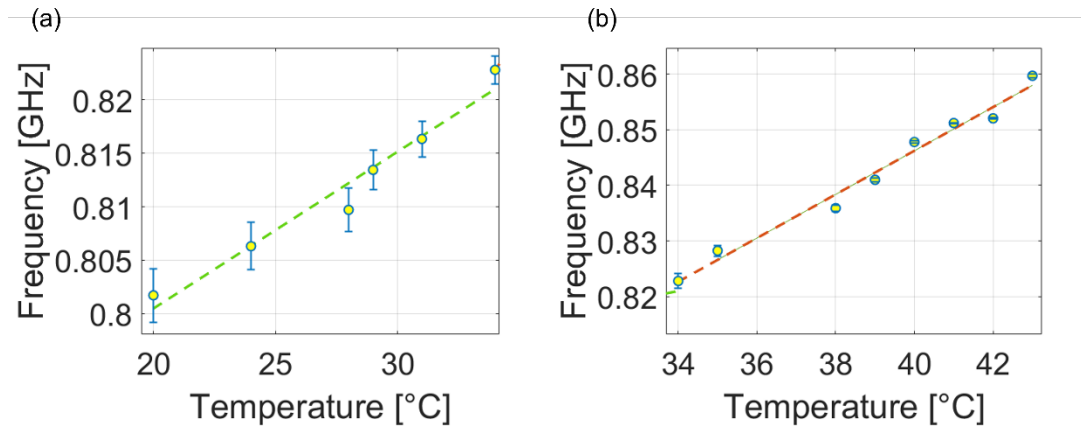
Figure 8.7: Calibration curves: a) Lower-sensitive region outside the body temperature range; b) higher-sensitive region inside the body-temperature region.

Finally, the performances in the water of the sensor have been compared with the state of the art in Table 8.2.

The footprint of the resonator is more than 8 times smaller than the others if compared with electrical lengths. Secondly, this sensor is the only one suitable for RFID applications as works in the 800 MHz band with the highest Q-factor and the best sensitivity in liquid environments. Thirdly, this device is the only flexible and is characterised by a planar geometry, very lightweight and straightforward to be produced in roll-2-roll processes.

Table 8.2: Comparison between the proposed M-CSRR and the state of the art.

	[107]	[18]	[17]	T.W.
Footprint [mm^2]	40x8	15x25	35x20	24x18
Frequency [GHz]	2.6	7.6	2.26	0.8
Submersible	No	Yes	No	Yes
Q-Factor (air)	42	937	-	702
Q-Factor (sub.sed)	-	-	-	600
Diel. Sensitivity [%]	0.27	-	0.98	1.5
Drop. Sensitivity [μl^{-1}]	-	-	-	0.3
Temp. Sensitivity [°C^{-1}]	-	-	-	0.5
Planar	Yes	No	No	Yes
Flexible	No	No	No	Yes

Chapter 9- Flexible Antennas

Antennas represents one of the main building blocks of any wireless transmission system. The role of the antenna is to convert electromagnetic fields travelling through the air into signals guided through transmission lines.

In a radio frequency sensor scenario, these devices play a crucial role as collect the interrogation signal, produce the excitation for the sensing element, and allow the retransmission of the corresponding response to the reader part. In order to perform this operation efficiently antennas have to face several challenges. Firstly, the compactness of the footprint. Secondly, the flexibility of the substrate to come to the rescue of the majority of non-invasive and wearable systems. Thirdly, optimal radiation properties, including high gains combined with low Specific Absorption Rate (SAR) minimise the risks on the human body application.

In this chapter, several antennas addressing these requirements are exposed. The first is a patch antenna whose footprint has been minimised exploiting a genetic algorithm. The radiation property of the antenna has been enhanced using a SRR metamaterial between the top radiative area and the ground. The two parts have been fabricated on PEN substrates and bonded together through a PDMS adhesion layer. Secondly, a PIFA is presented. The antenna is characterised by a planar geometry which requires the deposition of a single metallic path on the substrate. Consequently, the fabrication process is simpler and allows the realisation of the device on the PEN substrate.

9.1- Evolved Patch antenna

Figure 9.1 illustrates the structure of the proposed device. In detail, the stack is composed by two dielectric layers made of Polyethilene Naphtalate (PEN) and three metallic ones. The first layer (i.e., the radiative one) is optimized by employing a Genetic algorithm to miniaturize the geometry; the second metallic layer is a metamaterial based on an SRR, used to improve the radiation properties of the device. Finally, there is a ground plane for protecting the body from backside radiation.

The substrate is a 250 μm-thick PEN dielectric layer, with a relative dielectric constant equal to 2.9 and a loss tangent equal to 0.005. The choice of this substrate is due to the good trade-off between flexibility and minimal dielectric losses. The evolved antenna works at 4 GHz, in the sub-6GHz band of 5G spectrum.
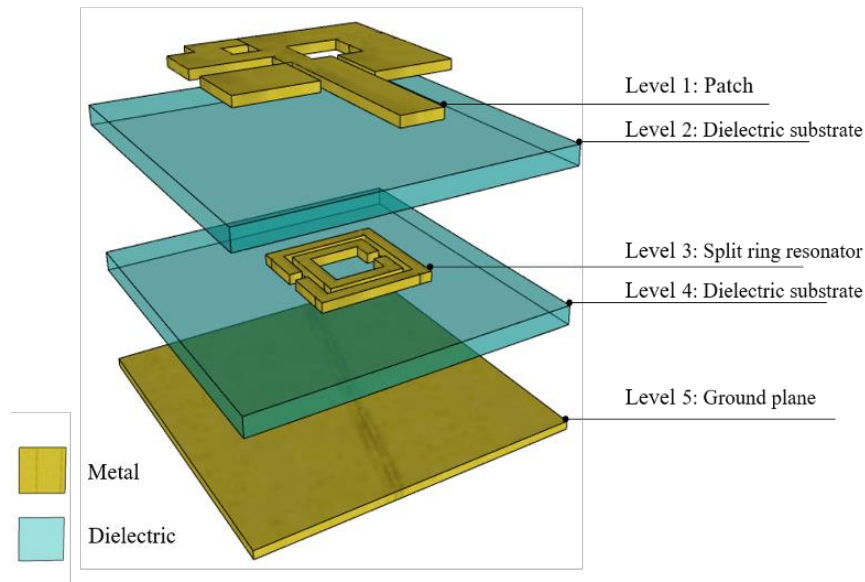

Figure 9.1: Breakdown of the evolved patch antenna.

9.1.1- Genetic Algorithm

The Genetic Algorithm (GA) is one of the most suitable optimization algorithms for threating problems which can be coded in binary form. This algorithm is based on Darwinian's laws. The workflow starts from an initial binary population representing the parents that evolve iteratively, and step by step minimises more and more a given cost function.

The steps of the GA can be synthesized as in Figure 9.2, reporting the flow-chart of the algorithm.
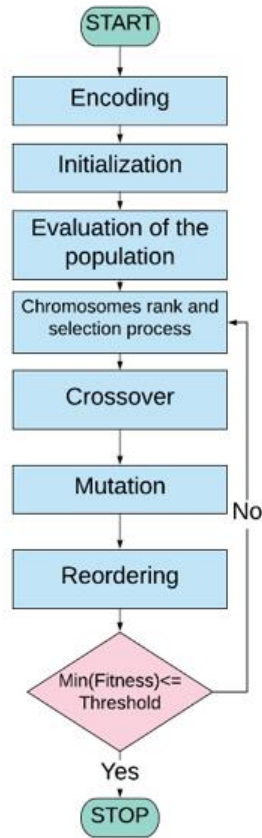
Figure 9.2: Flow-chart of the Genetic Algorithm.

The starting point for the design of the evolved radiative element is a classical patch antenna placed on a 250-μm thick PEN substrate with a footprint of 17 x 14 mm^2 (0.34 λ x 0.28 λ). The working frequency is at 6 GHz; with a bandwidth of 50 MHz and a realized gain which equals 5.8 dBi.

The geometrical parameters used for the simulations are listed in Table 9.1.

Table 9.1-Geometrical parameter of the considered patch antenna.

Parameter	Value [mm]
W	16.88
L	13.77
F_i	5.26
Wf	3.19
W_g	32

L_g	32

1) Encoding: the patch antenna is subdivided into 32 pixels with a square form of 2 μm; each of them represents a gene and assumes a value equals to 1 if the pixel is made of metal or 0 if it is made of vacuum.

2) Initialization: members of the population are randomly generated. It is very important to fix the number of the population according to the field of the application of the GA: if the number of the population is high, the result is very precise with the drawbacks of a higher computational time. On the other side, when a small population is considered, the process is almost fast but could be stacked in local minima. For this application, the radiating area has to be big enough to guarantee optimal radiation properties, so at least the 60% of metal has been imposed.

3) Evaluation of the population: each element of the population gets a score accordingly to the fitness function $C(f_R)$ expressed as in Equation 9.1.

$$C(f_R) = \begin{cases} |50 - Re\{Z(f_R)\}|e^{\frac{-(f_c - f_R)}{f_c}} & f_c - \delta < f_R < f_c + \delta \\ 1000 & otherwhise \end{cases} \qquad (9.1)$$

In particular, the resonant frequency (f_R) and the value of the impedance ($Z(f_R)$) at the resonant frequency are estimated by means of a finite difference time domain solver. The objective frequency (f_c) is at 4 GHz and δ is the tolerance error.

All the combinations of the gene which compose antennas having the real part of the impedance far from 50 Ω have been discarded.

4) Chromosomes rank and selection process: the chromosomes mate following a roulette selection process. Each element has associated a probability of selection, π_i which follows a Boltzmann distribution, as in Equation:

$$\pi_i = e^{-\beta c_i} \qquad (9.2)$$

C_i is the value of the cost function of the i-th element of the population and β is a normalization factor equal to $\beta = \frac{1}{N}\sum_{i=1}^{N} c_i$.

5) Crossover: the couples associated in the previous step generate new offspring by a single-point crossover.

6) Mutation: a random variation is applied to a single gene on an element of the population with a probability equals to 1%.

7) Reordering: as in step 3, the fitness function is evaluated for each device of the new population. Then, elements are rearranged in ascendent order for the value of their fitness function: the ones characterized by a high-cost function are discarded.

8) Loop statement: The value of the cost function of the elements is compared with the threshold value of the algorithm: if the convergence is reached the process is completed, otherwise it restarts from step 3.

The algorithm converged after 12 iterations and has turned out a patch antenna with a footprint of 14 x 17 mm^2 working at 4 GHz with an S_{11} dip equal to -24.47 dB and a bandwidth of 14 MHz. The realized gain of the device at the resonant frequency is equals to -0.647 dBi.

9.1.2- Metamaterials: Split Ring Resonator

One of the drawbacks of the miniaturization step is a degradation of the radiation properties of the antenna. To improve this aspect a μ-negative split ring resonator is added between the top and ground plane.

In detail, the geometry is a Square SRR (S-SRR) (Figure 9.3a) composed of two concentric split rings with the aperture placed in opposite directions and separated by a gap.

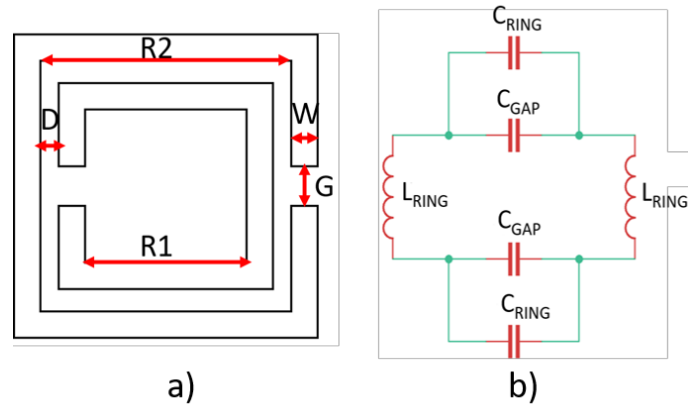The SRR can be treated as an LC circuit as reported in Figure 9.3b.

*Figure 9.3: CSRR a) geometry, b) equivalent circuit.*

The geometry of the square split ring resonator has been properly designed to increase the gain at the working frequency of the antenna.

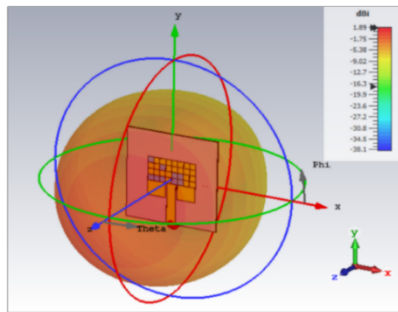The geometrical dimensions of the S-SRR are listed in Table 9.2.

Table 9.2-Geometrical parameters of the square SRR

Parameter	Value [mm]
R1	4.5
R2	3
W	1
D	0.5

The effects of the integration between the patch and the SRR has been considered exploiting a FDTD model of the multilayer stack, whose results are shown in Figure 9.4.
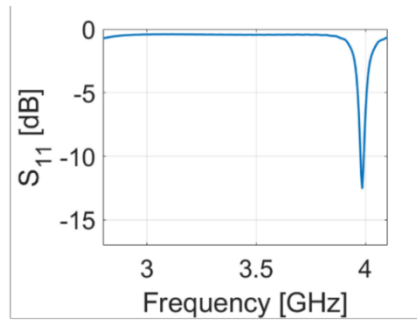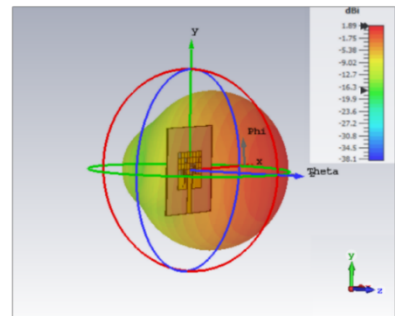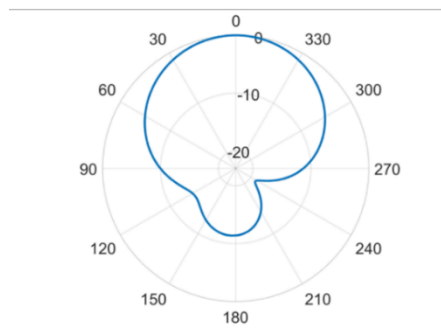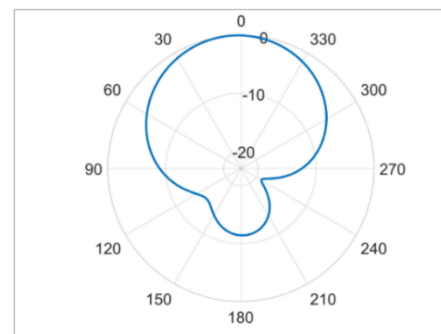
Figure 9.4: Simulations of the multilayer stack, a) Scattering parameter S_{11} of the device, b) top-view and c) side-view of the 3D radiation pattern, d) E-plane, e) H-plane polar plots of the radiation pattern.

In Figure 9.4a the trend of the S_{11} parameter is shown; there is a dip of -14.2 dB at 4 GHz with a bandwidth of about 15 MHz.

In Figures 9.4b and 9.4c two different perspectives of the 3D realized gain of the patch antenna at the resonant frequency are reported; the corresponding maximum value is equal to 1.89 dBi.

In Figures 9.4d and 9.4e the radiation pattern in the E-plane and H-plane are reported, respectively. In particular, the E-plane ($\phi = 0°$) presents a magnitude of

the main lobe equals to 1.89 dBi, with a direction of 3.0°, and an angular width (3 dB) of 93.2°. Whereas in the H-plane ($\phi = 90°$) the main lobe magnitude is equal to 1.88 dBi and the main lobe direction is equal to 0 deg with an angular width (3 dB) equals to 92°. The simulated directivity is 6.48 dBi at 4 GHz.

The results of the miniaturization process are summarized in Table 9.3.

Table 9.3- Comparison between a classical and the evolved patch antenna.

	Classical Patch antenna	Evolved Patch antenna
Working Frequency	6 GHz	3.96 GHz
Electrical Length	$0.34\lambda \; x \; 0.28\lambda$	$0.22\lambda \; x \; 0.18\lambda$
Bandwidth	50 MHz	15 MHz
Gain	5.8 dBi	1.89 dBi
Physical dimensions	$17 \; x \; 14 \; mm^2$	$17 \; x \; 14 \; mm^2$

An increase of 1.24 dBi of the gain without increasing the footprint of the device can be observed. The final device is having a footprint of 14 x 17 mm² at 4 GHz: in comparison with a classical patch antenna working at 6 GHz a size reduction of the 60% has been achieved. Although the antenna presents a slight degradation of gain and efficiency due to the minimization process, the simulated values suggest its use for wireless communications.

9.1.3- Fabrication Process

The device has been fabricated using the nano dimensions dragonfly multimaterial 3D printed with two PEN substrates. The PEN material has been treated for 15 minutes with a plasma-oxygen generated using a power of 150 W for both cases.

The first printed layer has been the radiative part of the evolved patch and markers for the alignment on X- and Y- axis. Then, the substrate has been flipped, the printing position has been corrected and then the process has gone on with the printing of both SRR, and the ground plane (see Figure 9.5b). All these radiating elements are printed with a thickness of 35 μm (the declared minimum thickness to obtain a good conductivity is 17 μm).
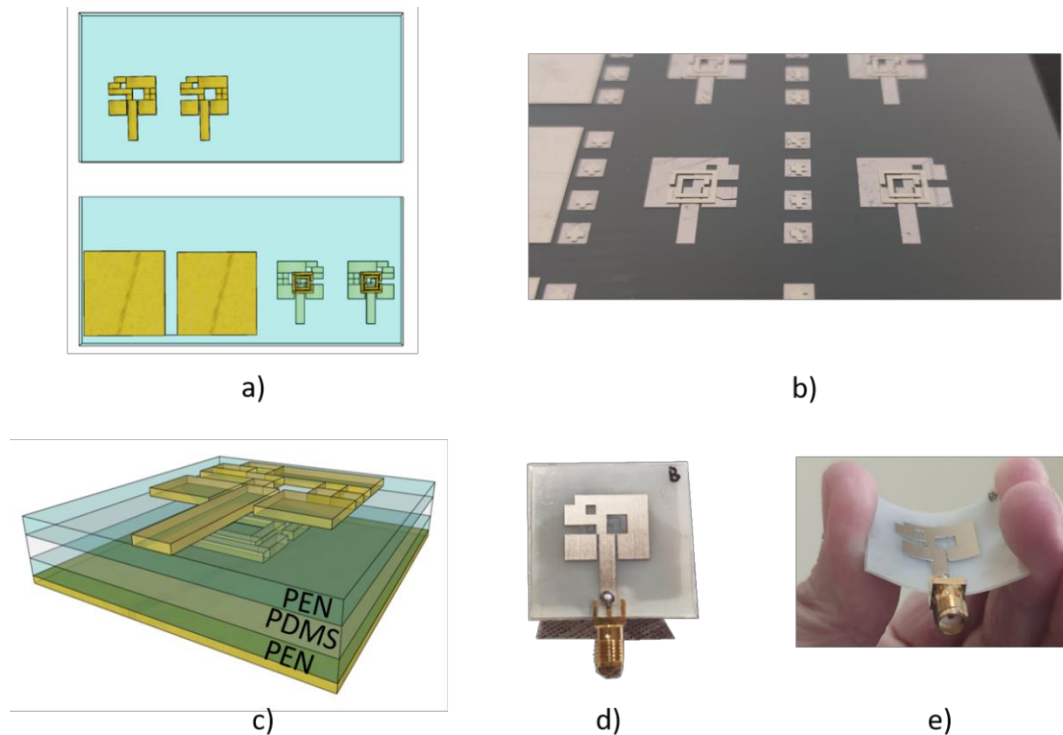

Figure 9.5: Fabrication process of the patch antenna, a) sketched top view of the two substrates, b) printed patch antennas and CSRRs, c) breakdown of the device, d) fabricated antenna, e) antenna after bending.

After the printing, the layer containing the patch together with the SRR and one containing the ground plane have been cut by means of a laser-cutter (Universal Laser System vls2.30). The Laser cutter is an economical and compact platform characterized by a working area of 12,585 cm^3 and a CO_2 laser of 10.6 μm. Different parameters have to be fixed before the cut: the power of the laser (in the range of 10-30W), the velocity of the tip, the distance between the tip and the sample and the Pulse Per Inch (PPI), driving the precision of the cut.

The two layers are bonded together by means of an adhesive interlayer made of Polydimethylsiloxane PDMS (Sylgard 184, Dowsil) mixed in a ratio of 1:10 with its curing agent.

9.1.4- Characterisation

The device has been characterized in terms of the S_{11} parameter, using a VNA (Anritsu MS46122B), 3D radiation pattern and polar plots. The results are shown in Figure 9.6.
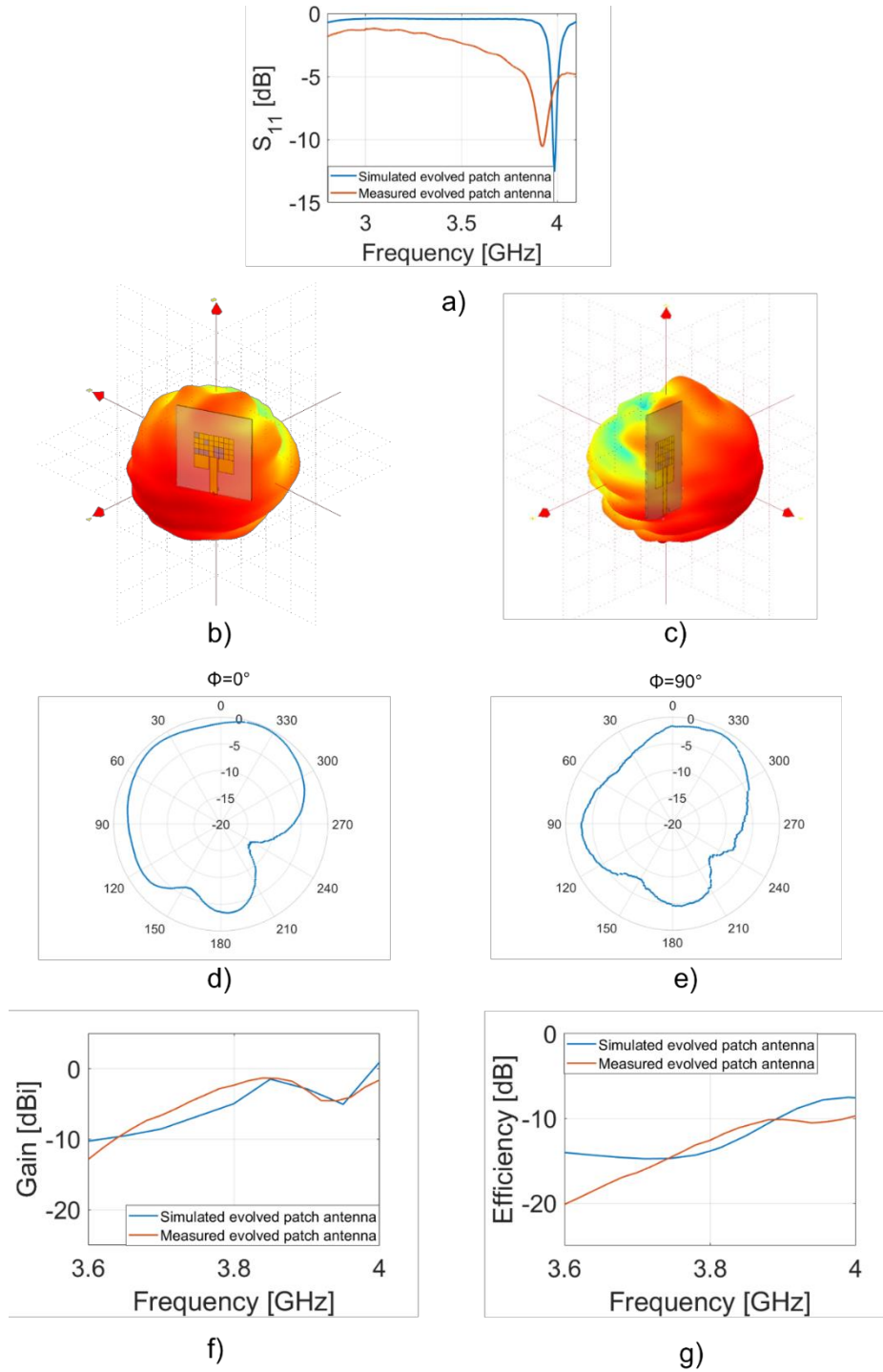

Figure 9.6: Characterisation of the device, a) comparison between the simulated and the measured scattering parameter S_{11}, b) front and) side views of the 3D radiation pattern, d) E-plane and e)H-plane polar plots of the radiation pattern, f) comparison between the simulated and the measured maximum value of the gain, g) simulated and measured radiation efficiencies.

Figure 9.6a shows a comparison between the trends of the simulated (blue curve) and the measured (red curve) scattering parameters S_{11}.

It is possible to observe a shift of a few MHz between simulations and measurements (e.g. –14.2 dB at 3.984 GHz and -13.41 dB at 3.962 GHz for the simulated and the measured evolved patch antenna, respectively). The presence of a coaxial connector causes the presence of a static capacitance, so it increases the electrical length of the device. The 3D radiation patterns are reported in Figure 9.6b and 9.6c. At the resonant frequency of about 4 GHz, the simulated realized gain is equal to -0.8 dBi by considering, while the measured one is equal to -1.5 dBi. The measurements are performed by means of an anechoic chamber (StarLab from Satimo), working in a frequency range between 800 MHz and 18 GHz. The working principle of the chamber provides the results in a few minutes by using Huygens's principle, thanks to which it is possible to reconstruct the far field (FF) starting from the indirect measurements of the Near Field (NF).

Measured 2D polar plots for E-plane ($\phi=0°$) and H-plane ($\phi=90°$) are presented in Figure 9.6d and 9.6e: for both planes. As in the previous case, there is a good agreement between simulations and measurements. Figure 9.6f reports the comparison between the trend of the simulated (blue curve) and simulated (red curve) realized gain near to the resonant frequency; also in this case, the experimental results follow the numerical ones. Finally, in Figure 9.6g, the trend of the efficiency is shown: the simulated value (blue curve) is higher than the measured one (red curve) at 4 GHz. This phenomenon may be caused by different factors: the soldering of SMA connector, the presence of the solvent mixed with Ag-based ink used during the printing process of the radiating elements and the losses of the PEN substrate that are reported in the datasheet until the frequency equal to 1 GHz.

9.2- Planar Inverted-F Antennas

The geometry of a PIFA is very straightforward as is formed by a monopole shorted with the ground plane. The radiation pattern is omnidirectional, and the footprint is very lightweight and compact, as the presence of the shorting-ping decreases the dimensions of the antenna. The feed is placed between the transmission line and the short-cutted end. Varying the position of the feeding impedance can be adapted

without the use of external components. From a microwave point of view, the shorting pin acts as a parallel inductance, indeed the more the feeding is near to the shorting pin the higher the impedance of the antenna. Another interesting property of PIFAs is the planar geometry which allows rapid and low costs fabrications.

In this scenario, the integration of PIFA on flexible substrates can be very interesting combining their interesting peculiarities with bendability and wearability. The sketch of the proposed antenna is shown in Figure 9.7, in which the red portion represents the metallic areas, while the light blue section is the dielectric substrate. All the optimised geometrical parameters are listed in Table 9.4.
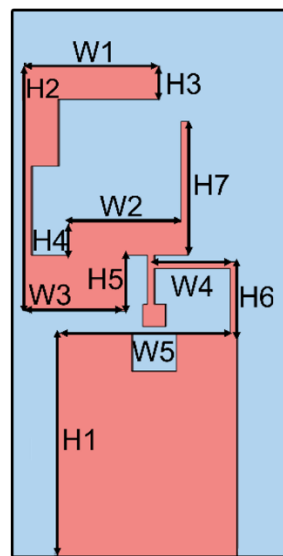

Figure 9.7: Geometry of the PEN-based PIFA antenna.

Table 9.4: Geometrical parameter of the PEN-based PIFA antenna.

	W1	W2	W3	W4	W5	H1	H2	H3	H4	H5	H6	H7	W	H
PIFA	6	5	4.5	4	8	9	11	1.5	1.5	2.5	3	6	10	24

The antenna is placed on a PEN substrate with a thickness of 250 μm, a relative dielectric permittivity of 2.9 and a loss tangent of 0.005.

It is a compact, flexible and dual-band device that resonates at 3.8 GHz and 6.1 GHz. Both of these frequencies are in the sub-6GHz band of 5G spectrum and are licensed in Europe (3.8 GHz) and USA (6.1 GHz). The PIFA configuration is composed of two different L-shaped regions: W1xH1 is responsible of the impedance matching at the lower frequency, 3.8 GHz, while W2xH2 is used for

achieving the impedance matching at the higher one, 6.1 GHz. The intermediate part of the antenna is used as a feeding point for placing the U.FL connector. The total footprint of the device is 10x24 mm^2.

PIFA is very sensitive to geometrical variations; the slightest modification could cause impedance mismatching and variation in the resonant frequency. To achieve a good impedance matching at the two resonant frequencies, some parametrical sweeps have been performed. As example, the trend of the S_{11} parameter by varying H2 and H7 has been reported in Figure 9.8.
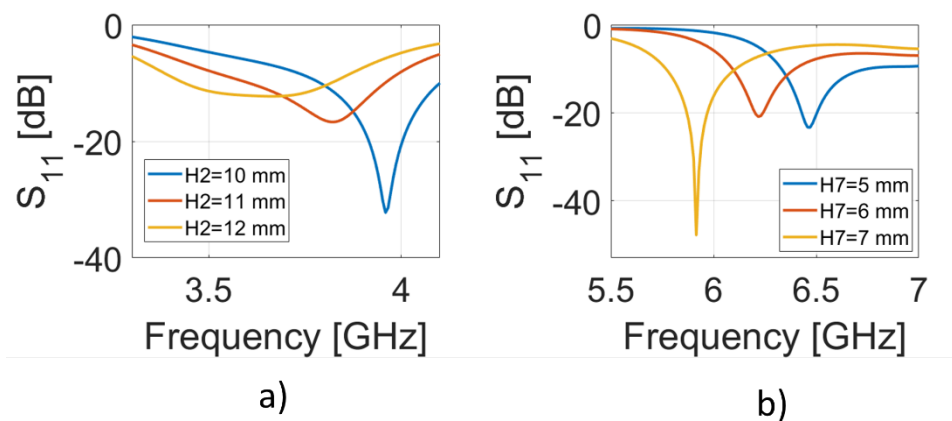

Figure 9.8-Effects of PIFA's parameters on return loss at a) around 3.81 GHz and b) 6.22 GHz

From Figure 9.8a it is possible to note that the resonant frequency decreases by increasing the value of H2 parameter. The optimal value is H2 for equal to 11mm since the resonance is in the band of interest (3.6 - 3.8 GHz).

As regards the parameter H7, in Figure 9.8b), the dip of the S_{11} moves to a lower frequency when the value of H7 increases and when H7 is equal to 6 mm the working frequency is in the band of interest.

It is worth stressing that H2 does not cause any variation in the higher band of the antenna and vice versa for H7.

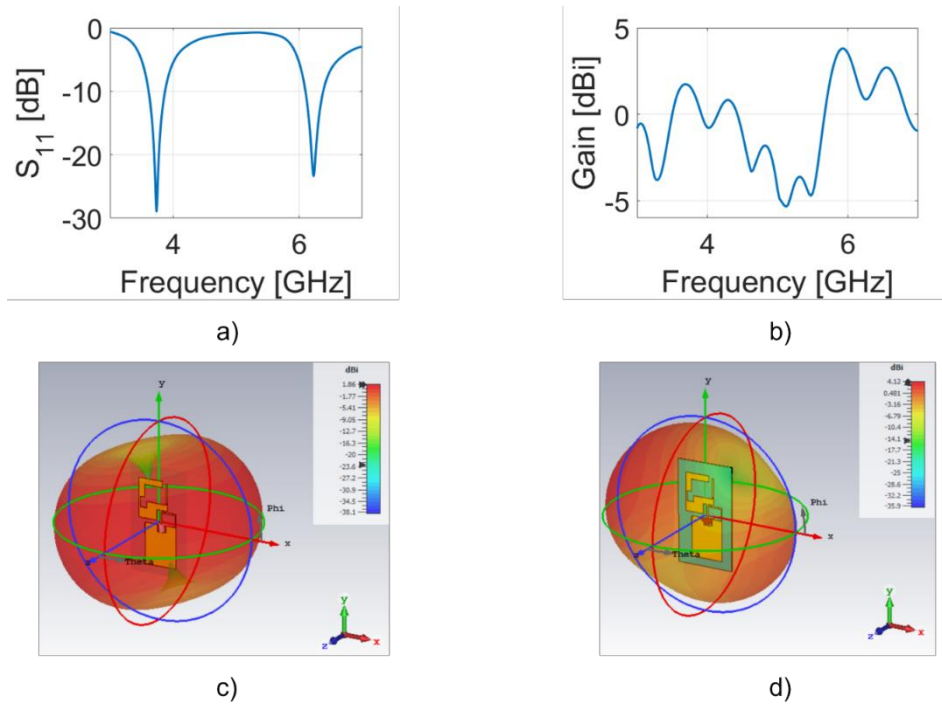In Figure 9.9, the simulation results of the optimized antenna are shown.

Figure 9.9- Simulations of the PEN-based PIFA antenna a) Scattering parameters of the PIFA antenna, b) Gain vs Frequency of the antenna, c) top view and d) side-view of the 3D radiation pattern.

In Figure 9.9a the trend of the S_{11} parameter is reported. There is a first dip of -30 dB at 3.8 GHz and the second one of -22 dB is at 6.1 GHz. In figure 9.9c 9.9d radiation patterns for realized gain are shown. The maximum value of the is equal to 1.86 at 3.8 GHz and to 4.12 at 6.1 GHz.

9.2.2- Fabrication and characterization

The device has been fabricated directly on the PEN substrate employing a multi-material 3D printer, Nano Dimension's DragonFly LDMTM System, after a preliminary Plasma Oxygen treatment. In this case, approximately 40 μm of metal have been deposited and a total of 50 antennas have been fabricated in a couple of hours on a printing area of about 18x18 cm^2.

An array of 3x3 fabricated antennas and some prototypes are shown in Figure 9.10. It is possible to note that some grid lines of a few micrometres thickness have been printed to cut the devices with the laser cutter in a fast and precise way.
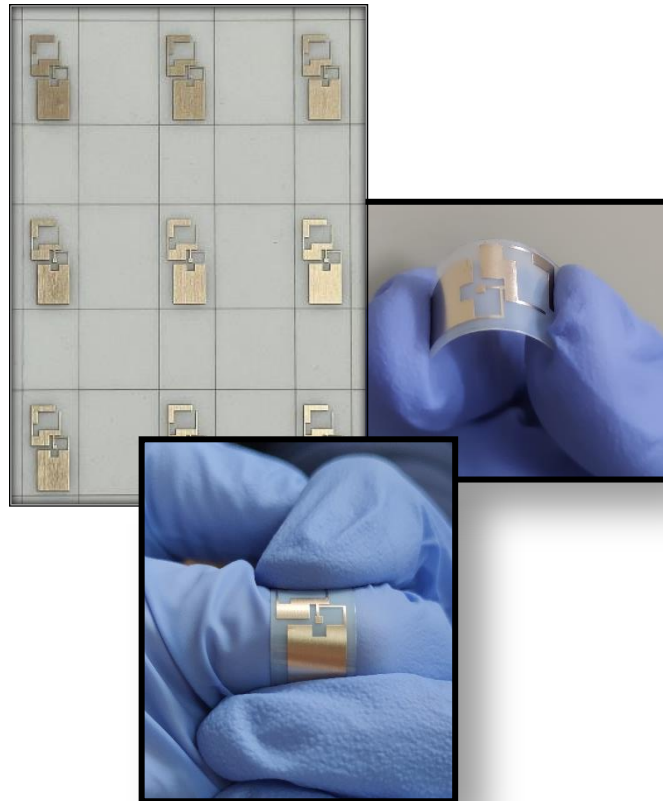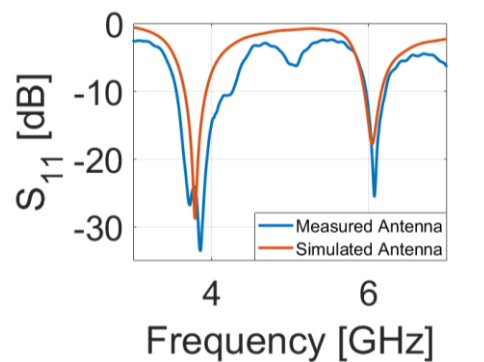
Figure 9.10: Fabricated PEN-based PIFA.

The antenna has been connectorized with a U.Fl connector soldered between the top and the ground plane and characterized through a VNA.

a)   b)

Figure 9.11: Characterisation of the device, a) antenna connected to the VNA using a self-standing configuration, b) Measured vs Simulated scattering parameter S_{11}.

The fabricated PIFA (red curve) resonates a 3.86 GHz with a bandwidth of 700 MHz. It is larger than the simulated one (blue curve) due to the electromagnetic losses introduced by soldering the connector and by the presence of an amount of

solvent mixed with the conductive ink. As regards the second resonance, at 6.1 GHz, there is a good agreement between simulations (red curve) and measurements (blue curve) also in terms of bandwidth. The measured gain is equal to 0.9 dBi and 1.1 dBi for 3.8 GHz and 6.1 GHz, respectively. For the lower frequency, the obtained value is very close to the simulated one; while for the higher frequency, the value is lower than the simulated one. This is probably due to the presence of the RF cable on the radiating part of the antenna, reducing its radiation efficiency.

Conclusions

Flexible microwave sensors offer big advantages for classical bulk and low-frequency technologies. The use of flexible materials allows the devices to adapt their shape to curve surfaces enhancing the wearability on the human body. Moreover, with the use of microwave frequencies, cables and connectors can be avoided minimizing the impact of the sensors. In this scenario, the design and fabrication of sensors able to work in water take interesting new perspectives, especially in sweat monitoring or edible sensors. Although their exceptional properties these resonators present challenges to overcome.

In the quest for a rapid and accurate design process of FBARs, the inclusion of material specifications and fabrication tolerances is a crucial point. In chapter 2 and 3 of this thesis work, the addressing of several issues regarding the design and the fabrication of MEMS and microstrip resonators has been performed.

In chapter 4, a novel design algorithm able to simulate the response of FBARs with a very small computational cost has been presented. The tool is based on material calibration curves which can be obtained by FEM simulations or fabrications, including material specifications in a very specific way. Moreover, the structure of the algorithm is highly scalable, calibration curves can be rearranged, and new materials can be included without any modification to its code. The very low computational costs of our approach allow the inclusion of fabrication tolerances through Monte Carlo simulations. The piezoelectric and metal thicknesses can be varied accordingly to the status of the equipment and technological requirements and the Probability Density Function (PDF) of the resonant position can be easily obtained. The calibration curves are reusable and arranged into a modular library that can be easily enriched with new materials even starting from experimental data. Moreover, the algorithm includes the possibility to consider fabrication tolerances and bridging the gap between the simulations and the experimental devices.

In chapter 5, the high accuracy of the design algorithm can be applied to the design of FBAR pass-band ladder filters, estimating with high precision the thickness of the mass loads on the shunt resonators to obtain a flat pass-band response. This

capability has been demonstrated by the reverse engineering of an existing filter reported in Reference [63]. The design tool has been able to determine with very high precision the amount of mass-loading on the molybdenum shunt electrodes reporting results perfectly in-line with the one declared by the authors. A new simulation utility for the evaluation of the filter response has been used for the comparison between the output of the decision algorithm and the experimental results. Differently from commonly used simulation techniques with our approach the frequency response of pass-band ladder filters can be evaluated with high precision starting from the impedance of the single-stage resonators. The simulation utility returns a pass-band response perfectly following the measurements in Reference [63].

Besides their design, the fabrication of MEMS resonators on flexible substrates is a crucial challenge to overcome in the quest for wearable and wireless sensors. In chapter 6, the development of a gravimetric sensor based on a flexible AlN-based FBAR resonator has been presented. The device has been designed using the design approach discussed in chapter 4, together with a FEM model. The fabrication protocol has been demonstrated to be very effective as it has taken to an optimal quality resonator having a response perfectly in line with simulations. The resonator has shown optimal performance with a Q-factor of 218 and an electromechanical coupling factor of 6%. The device has been demonstrated to be very sensitive to mass variations and the dependence on the added mass is linear. The mass-responsivity of the resonator has been estimated by spinning several amounts of PMMA from 250 nm to 600 nm. The fitting curve interpolating the experimental points has been derived and the responsivity of the sensor has been proved to be 23.31 ppm/pg. We strongly believe that these results can pave the way for a new class of wearable MEMS biosensors exploiting Ultra High Frequency (UHF) transmissions. Although it's very promising properties the absence of a suspended structure limits the performance of the resonator.

In chapter 7 the fabrication and the characterisation of flexible FBARs based on polymeric membranes have been presented. The resonators have been also combined in a device formed of nine resonators. The fabrication protocol has been demonstrated effective as high-quality resonators have been obtained. The single resonator presents small electrical resistance and optimal radio frequency

performance. In particular, the resonator works at 2.54 GHz, with a quality factor of 260. The combined device presents the same working frequency but a higher Q-factor of 742.

The development of a flexible microstrip CSRR-based sensor on a flexible Kapton substrate has been proposed in chapter 8. The device has been fabricated using a 3D multi-material inkjet printing and coated with parylene C. The obtained process yield is high as 9 resonators have been obtained in less than 2 hours. It is underlined that the printing area has not been fully exploited as the maximum number of resonators is about 48. The device presents optimal performance with very high Q-factors of 702 and 501 when in air and water, respectively proving its suitability in healthcare applications. High sensitivity to water droplets when in the air has been proven suggesting its use in wearable sweat or humidity sensors. The sensitivity versus temperature in water has been tested, reporting optimal performances and overcoming the state of the art in terms of footprint, sensitivity and Q-factor. Moreover, the integration of our sensor with external antennas can pave the way to a passive and wireless water temperature sensor. The use of a multi-material 3D printer allows the fabrication of dielectric containers, microfluidic channels, or needles. This approach can reduce drastically the times for prototyping high-sensitive sensors on flexible substrates.

Finally, in chapter 9 the development of flexible antennas has been presented. A patch antenna and a PIFA have been fabricated on a PEN substate with optimal results.

A potential future development of this study could be the enhancing of the sensitivity of the resonators, through functionalization of their surfaces or with the fabrication of microfluidic channels to better control the influence of the LUT. Another possible expansion of this work may be the integration between the antennas with the previously cited resonators. The last could be an enormous step forward in the quest for wearable sensing platforms which overcome the use of cables and connectors.

Bibliography

[1]   J. Gubbi, R. Buyya, S. Marusic, and M. Palaniswami, "Internet of Things (IoT): A vision, architectural elements, and future directions," *Future Generation Computer Systems*, vol. 29, no. 7, 2013, doi: 10.1016/j.future.2013.01.010.

[2]   Y. Khan, A. Thielens, S. Muin, J. Ting, C. Baumbauer, and A. C. Arias, "A New Frontier of Printed Electronics: Flexible Hybrid Electronics," *Advanced Materials*, vol. 32, no. 15. 2020. doi: 10.1002/adma.201905279.

[3]   P. Wang *et al.*, "The Evolution of Flexible Electronics: From Nature, Beyond Nature, and To Nature," *Advanced Science*, vol. 7, no. 20. 2020. doi: 10.1002/advs.202001116.

[4]   Z. Wang, L. Sun, Y. Ni, L. Liu, and W. Xu, "Flexible Electronics and Healthcare Applications," *Frontiers in Nanotechnology*, vol. 3. 2021. doi: 10.3389/fnano.2021.625989.

[5]   Y. Chen *et al.*, "Skin-like biosensor system via electrochemical channels for noninvasive blood glucose monitoring," *Sci Adv*, vol. 3, no. 12, 2017, doi: 10.1126/sciadv.1701629.

[6]   J. Yang *et al.*, "Flexible, Tunable, and Ultrasensitive Capacitive Pressure Sensor with Microconformal Graphene Electrodes," *ACS Appl Mater Interfaces*, vol. 11, no. 16, 2019, doi: 10.1021/acsami.9b02049.

[7]   H. Zhang *et al.*, "Flexible and Stretchable Microwave Electronics: Past, Present, and Future Perspective," *Advanced Materials Technologies*, vol. 6, no. 1. 2021. doi: 10.1002/admt.202000759.

[8]   Z. Xie, R. Avila, Y. Huang, and J. A. Rogers, "Flexible and Stretchable Antennas for Biointegrated Electronics," *Advanced Materials*, vol. 32, no. 15. 2020. doi: 10.1002/adma.201902767.

[9]   W. Gao *et al.*, "Fully integrated wearable sensor arrays for multiplexed in situ perspiration analysis," *Nature*, vol. 529, no. 7587, pp. 509–514, Jan. 2016, doi: 10.1038/nature16521.

[10]   D. Pozar, *Microwave Engineering Fourth Edition*. 2005. doi: TK7876.P69 2011.

[11]   W. T. S. Chen and R. R. Mansour, "Miniature gas sensor and sensor array with single- and dual-mode RF dielectric resonators," in *IEEE Transactions on Microwave Theory and Techniques*, 2018, vol. 66, no. 8. doi: 10.1109/TMTT.2018.2854551.

[12]   Y. J. Mao, Y. J. Zhang, Z. R. Chen, and M. S. Tong, "A Noncontact Microwave Sensor Based on Cylindrical Resonator for Detecting Concentration of Liquid Solutions," *IEEE Sens J*, vol. 21, no. 2, 2021, doi: 10.1109/JSEN.2020.3016290.

[13]   M. G. Mayani, F. J. Herraiz-Martinez, J. M. Domingo, R. Giannetti, and C. R. M. Garcia, "A Novel Dielectric Resonator-Based Passive Sensor for Drop-Volume Binary Mixtures Classification," *IEEE Sens J*, vol. 21, no. 18, 2021, doi: 10.1109/JSEN.2021.3094904.

[14]   H. Huang, "Flexible wireless antenna sensor: A review," *IEEE Sensors Journal*, vol. 13, no. 10. 2013. doi: 10.1109/JSEN.2013.2242464.

[15]   Q. Xue, X. Tang, Y. Li, H. Liu, and X. Duan, "Contactless and Simultaneous Measurement of Water and Acid Contaminations in Oil Using a Flexible Microstrip Sensor," *ACS Sens*, vol. 5, no. 1, 2020, doi: 10.1021/acssensors.9b01965.

[16]   A. Buragohain, A. T. T. Mostako, and G. S. Das, "Low-Cost CSRR Based Sensor for Determination of Dielectric Constant of Liquid Samples," *IEEE Sens J*, vol. 21, no. 24, 2021, doi: 10.1109/JSEN.2021.3124329.

[17]   L. C. Fan, W. S. Zhao, D. W. Wang, Q. Liu, S. Chen, and G. Wang, "An Ultrahigh Sensitivity Microwave Sensor for Microfluidic Applications," *IEEE Microwave and Wireless Components Letters*, vol. 30, no. 12, 2020, doi: 10.1109/LMWC.2020.3029060.

[18]   X. Zhang, C. Ruan, W. Wang, and Y. Cao, "Submersible high sensitivity microwave sensor for edible oil detection and quality analysis," *IEEE Sens J*, vol. 21, no. 12, 2021, doi: 10.1109/JSEN.2021.3067933.

[19]   J. Iannacci, "RF-MEMS for high-performance and widely reconfigurable passive components – A review with focus on future telecommunications, Internet of Things (IoT) and 5G applications," *Journal of King Saud University - Science*, vol. 29, no. 4. 2017. doi: 10.1016/j.jksus.2017.06.011.

[20]   X. Le, Q. Shi, P. Vachon, E. J. Ng, and C. Lee, "Piezoelectric MEMS - Evolution from sensing technology to diversified applications in the 5G/Internet of Things (IoT) era," *Journal of Micromechanics and Microengineering*, vol. 32, no. 1, 2022, doi: 10.1088/1361-6439/ac3ab9.

[21]   K. Hashimoto, *Surface Acoustic Wave Devices in Telecommunications*. 2000. doi: 10.1007/978-3-662-04223-6.

[22]   R. Lu, Y. Yang, S. Link, and S. Gong, "A1 Resonators in 128° Y-cut Lithium Niobate with Electromechanical Coupling of 46.4%," *Journal of Microelectromechanical Systems*, 2020, doi: 10.1109/JMEMS.2020.2982775.

[23]   Y. Q. Fu *et al.*, "Recent developments on ZnO films for acoustic wave based bio-sensing and microfluidic applications: a review," *Sens Actuators B Chem*, 2010, doi: 10.1016/j.snb.2009.10.010.

[24]   J. Wu *et al.*, "Ultrathin Glass-Based Flexible, Transparent, and Ultrasensitive Surface Acoustic Wave Humidity Sensor with ZnO Nanowires and Graphene Quantum Dots," *ACS Appl Mater Interfaces*, vol. 12, no. 35, 2020, doi: 10.1021/acsami.0c09962.

[25] G. Chen *et al.*, "Film bulk acoustic resonators integrated on arbitrary substrates using a polymer support layer," *Sci Rep*, vol. 5, 2015, doi: 10.1038/srep09510.

[26] G. Pillai and S. S. Li, "Piezoelectric MEMS Resonators: A Review," *IEEE Sensors Journal*, vol. 21, no. 11. 2021. doi: 10.1109/JSEN.2020.3039052.

[27] Z. Hou *et al.*, "Inductively Coupled Plasma Etching of AlN Film for Fabrication of 5G Networks & Devices: A Methodological Study," *Zhenkong Kexue yu Jishu Xuebao/Journal of Vacuum Science and Technology*, vol. 40, no. 3, 2020, doi: 10.13922/j.cnki.cjovst.2020.03.07.

[28] F. Guido, A. Qualtieri, L. Algieri, E. D. Lemma, M. de Vittorio, and M. T. Todaro, "AlN-based flexible piezoelectric skin for energy harvesting from human motion," *Microelectron Eng*, vol. 159, 2016, doi: 10.1016/j.mee.2016.03.041.

[29] A. T. Tran, G. Pandraud, F. D. Tichelaar, M. D. Nguyen, H. Schellevis, and P. M. Sarro, "The extraordinary role of the AlN interlayer in growth of AlN sputtered on Ti electrodes," *Appl Phys Lett*, vol. 103, no. 22, 2013, doi: 10.1063/1.4835035.

[30] L. Natta *et al.*, "Conformable AlN Piezoelectric Sensors as a Non-invasive Approach for Swallowing Disorder Assessment," *ACS Sens*, vol. 6, no. 5, 2021, doi: 10.1021/acssensors.0c02339.

[31] E. Scarpa *et al.*, "Wearable piezoelectric mass sensor based on pH sensitive hydrogels for sweat pH monitoring," *Sci Rep*, vol. 10, no. 1, 2020, doi: 10.1038/s41598-020-67706-y.

[32] P. Delsing *et al.*, "The 2019 surface acoustic waves roadmap," *Journal of Physics D: Applied Physics*, vol. 52, no. 35. 2019. doi: 10.1088/1361-6463/ab1b04.

[33] M. Abd Allah, R. Thalhammer, J. Kaitila, T. Herzog, W. Weber, and D. Schmitt-Landsiedel, "Solidly mounted BAW resonators with layer-transferred AlN using sacrificial Si surfaces," in *Solid-State Electronics*, 2010, vol. 54, no. 9. doi: 10.1016/j.sse.2010.04.031.

[34] M. Kadota, Y. Suzuki, and Y. Ito, "FBAR using LiNbO3 thin film deposited by CVD," in *Proceedings - IEEE Ultrasonics Symposium*, 2010. doi: 10.1109/ULTSYM.2010.5935491.

[35] L. Khine, L. Y. L. Wong, J. B. W. Soon, and J. M. Tsai, "FBAR resonators with sufficient high Q for RF filter implementation," in *Advanced Materials Research*, 2011, vol. 254. doi: 10.4028/www.scientific.net/AMR.254.70.

[36] G. Wingqvist, L. Arapan, V. Yantchev, and I. Katardjiev, "A micromachined thermally compensated thin film Lamb wave resonator for frequency control and sensing applications," *Journal of Micromechanics*

and Microengineering, vol. 19, no. 3, 2009, doi: 10.1088/0960-1317/19/3/035018.

[37]   G. Niro, I. Marasco, F. Rizzi, A. D'Orazio, M. de Vittorio, and M. Grande, "Design of a surface acoustic wave resonator for sensing platforms," in *IEEE Medical Measurements and Applications, MeMeA 2020 - Conference Proceedings*, 2020. doi: 10.1109/MeMeA49120.2020.9137116.

[38]   Y. Huang, P. K. Das, and V. R. Bhethanabotla, "Surface acoustic waves in biosensing applications," *Sensors and Actuators Reports*, vol. 3, 2021, doi: 10.1016/j.snr.2021.100041.

[39]   S. Maramizonouz *et al.*, "Flexible and bendable acoustofluidics for particle and cell patterning," *Int J Mech Sci*, vol. 202–203, 2021, doi: 10.1016/j.ijmecsci.2021.106536.

[40]   K. Li *et al.*, "Microstructure and bending piezoelectric characteristics of AlN film for high-frequency flexible SAW devices," *Journal of Materials Science: Materials in Electronics*, vol. 32, no. 10, 2021, doi: 10.1007/s10854-021-05830-9.

[41]   L. Lamanna, F. Rizzi, F. Giudo, and M. de Vittorio, "Flexible Dual-Wave Mode AlN-Based Surface Acoustic Wave Device on Polymeric Substrate," *IEEE Electron Device Letters*, vol. 41, no. 11, 2020, doi: 10.1109/LED.2020.3025607.

[42]   A. Pohl, "A review of wireless SAW sensors," *IEEE Trans Ultrason Ferroelectr Freq Control*, vol. 47, no. 2, 2000, doi: 10.1109/58.827416.

[43]   L. Zou, C. McLeod, and M. R. Bahmanyar, "Wireless Interrogation of Implantable SAW Sensors," *IEEE Trans Biomed Eng*, vol. 67, no. 5, 2020, doi: 10.1109/TBME.2019.2937224.

[44]   S. Taniguchi, T. Yokoyama, M. Iwaki, T. Nishihara, M. Ueda, and Y. Satoh, "An air-gap type FBAR filter fabricated using a thin sacrificed layer on a flat substrate," in *Proceedings - IEEE Ultrasonics Symposium*, 2007. doi: 10.1109/ULTSYM.2007.156.

[45]   M. Ueda *et al.*, "Development of an X-band filter using air-gap-type film bulk acoustic resonators," *Jpn J Appl Phys*, vol. 47, no. 5 PART 2, 2008, doi: 10.1143/JJAP.47.4007.

[46]   Y. Liu *et al.*, "An Air-Gap Thin Film Bulk Acoustic Resonator Filter with Laminated Film Bare Die," *Yadian Yu Shengguang/Piezoelectrics and Acoustooptics*, vol. 43, no. 3, 2021, doi: 10.11977/j.issn.1004-2474.2021.03.001.

[47]   X. L. He *et al.*, "Film bulk acoustic resonator pressure sensor with self-temperature reference," *Journal of Micromechanics and Microengineering*, vol. 22, no. 12, 2012, doi: 10.1088/0960-1317/22/12/125005.

[48]   C. Gu *et al.*, "Temperature calibrated on-chip dual-mode film bulk acoustic resonator pressure sensor with a sealed back-trench cavity," *Journal of*

Micromechanics and Microengineering, vol. 28, no. 7, 2018, doi: 10.1088/1361-6439/aab935.

[49] R. Patel, M. S. Adhikari, and D. Boolchandani, "Active area optimisation of film bulk acoustic resonator for improving performance parameters," *Electron Lett*, vol. 56, no. 22, 2020, doi: 10.1049/el.2020.1901.

[50] F. L. Duan *et al.*, "Process optimization and device variation of Mg-doped ZnO FBARs," *Solid State Electron*, vol. 151, 2019, doi: 10.1016/j.sse.2018.10.015.

[51] A. A. Mansour and T. S. Kalkur, "High-quality-factor and low-temperature-dependence SMR FBAR based on BST using MOD method," *IEEE Trans Ultrason Ferroelectr Freq Control*, vol. 64, no. 2, 2017, doi: 10.1109/TUFFC.2016.2630690.

[52] M. Dubois, "Thin film bulk acoustic wave resonators: a technology overview," *Memswave*, 2003.

[53] K. Länge, "Bulk and surface acoustic wave sensor arrays for multi-analyte detection: A review," *Sensors (Switzerland)*, vol. 19, no. 24, 2019, doi: 10.3390/s19245382.

[54] H. Zu, H. Wu, and Q. M. Wang, "High-Temperature Piezoelectric Crystals for Acoustic Wave Sensor Applications," *IEEE Trans Ultrason Ferroelectr Freq Control*, vol. 63, no. 3, 2016, doi: 10.1109/TUFFC.2016.2527599.

[55] W. Ren *et al.*, "Design and Optimization of a BAW Magnetic Sensor Based on Magnetoelectric Coupling," *Micromachines (Basel)*, vol. 13, no. 2, 2022, doi: 10.3390/mi13020206.

[56] J. Liu, Z. Zhao, Z. Fang, Z. Liu, Y. Zhu, and L. Du, "High-performance FBAR humidity sensor based on the PI film as the multifunctional layer," *Sens Actuators B Chem*, vol. 308, p. 127694, Apr. 2020, doi: 10.1016/J.SNB.2020.127694.

[57] I. S. Uzunov, M. D. Terzieva, B. M. Nikolova, and D. G. Gaydazhiev, "Extraction of modified butterworth - Van Dyke model of FBAR based on FEM analysis," in *2017 26th International Scientific Conference Electronics, ET 2017 - Proceedings*, 2017. doi: 10.1109/ET.2017.8124394.

[58] R. K. Thalhammer and J. D. Larson, "Finite-Element Analysis of Bulk-Acoustic-Wave Devices: A Review of Model Setup and Applications," *IEEE Transactions on Ultrasonics, Ferroelectrics, and Frequency Control*. 2016. doi: 10.1109/TUFFC.2016.2555306.

[59] A. Mujahid, A. Afzal, and F. L. Dickert, "An overview of high frequency acoustic sensors—QCMs, SAWs and FBARs—chemical and biochemical applications," *Sensors (Switzerland)*. 2019. doi: 10.3390/s19204395.

[60] T. Makkonen, A. Holappa, J. Ellä, and M. M. Salomaa, "Finite element simulations of thin-film composite BAW resonators," *IEEE Transactions*

on Ultrasonics, Ferroelectrics, and Frequency Control. 2001. doi: 10.1109/58.949733.

[61] N. N. Hu, X. L. He, X. L. Bian, G. H. Chen, S. R. Dong, and J. K. Luo, "Novel flexible FBAR on PET substrate," in *2014 IEEE International Conference on Electron Devices and Solid-State Circuits, EDSSC 2014*, 2014. doi: 10.1109/EDSSC.2014.7061215.

[62] Y. Jiang, M. Zhang, X. Duan, H. Zhang, and W. Pang, "A flexible, gigahertz, and free-standing thin film piezoelectric MEMS resonator with high figure of merit," *Appl Phys Lett*, vol. 111, no. 2, 2017, doi: 10.1063/1.4993901.

[63] Y. Jiang *et al.*, "Flexible Film Bulk Acoustic Wave Filters toward Radiofrequency Wireless Communication," *Small*, vol. 14, no. 20, 2018, doi: 10.1002/smll.201703644.

[64] Y. Xue, C. Zhou, X. Y. Zhang, and M. Chan, "A flexible high quality-factor bulk acoustic resonator enabled with transferred single-crystal piezoelectric thin film for sensing applications," *Sens Actuators A Phys*, vol. 326, p. 112721, Aug. 2021, doi: 10.1016/J.SNA.2021.112721.

[65] A. Erturk and D. J. Inman, "Appendix A: Piezoelectric Constitutive Equations," in *Piezoelectric Energy Harvesting*, 2011. doi: 10.1002/9781119991151.app1.

[66] A. Erturk and D. J. Inman, "Introduction to Piezoelectric Energy Harvesting," in *Piezoelectric Energy Harvesting*, 2011. doi: 10.1002/9781119991151.ch1.

[67] R. Streich, "3D finite-difference frequency-domain modeling of controlled-source electromagnetic data: Direct solution and optimization for high accuracy," in *Geophysics*, 2009, vol. 74, no. 5. doi: 10.1190/1.3196241.

[68] A. F. Oskooi, D. Roundy, M. Ibanescu, P. Bermel, J. D. Joannopoulos, and S. G. Johnson, "Meep: A flexible free-software package for electromagnetic simulations by the FDTD method," *Comput Phys Commun*, vol. 181, no. 3, 2010, doi: 10.1016/j.cpc.2009.11.008.

[69] K. Fujii *et al.*, "Study on the transmission mechanism for wearable device using the human body as a transmission channel," in *IEICE Transactions on Communications*, 2005, vol. E88-B, no. 6. doi: 10.1093/ietcom/e88-b.6.2401.

[70] A. Sani, Y. Zhao, Y. Hao, A. Alomainy, and C. Parini, "An efficient FDTD algorithm based on the equivalence principle for analyzing onbody antenna performance," *IEEE Trans Antennas Propag*, vol. 57, no. 4 PART. 1, 2009, doi: 10.1109/TAP.2009.2014581.

[71] F. Yang and Y. Rahmat-Samii, *Electromagnetic band gap structures in antenna engineering*, vol. 9780521889919. 2008. doi: 10.1017/CBO9780511754531.

[72] D. M. Sheen, S. M. Ali, M. D. Abouzahra, and J. A. Kong, "Application of the Three-Dimensional Finite-Difference Time-Domain Method to the Analysis of Planar Microstrip Circuits," *IEEE Trans Microw Theory Tech*, vol. 38, no. 7, 1990, doi: 10.1109/22.55775.

[73] H. Mosallaei and K. Sarabandi, "Antenna miniaturization and bandwidth enhancement using a reactive impedance substrate," *IEEE Trans Antennas Propag*, vol. 52, no. 9, 2004, doi: 10.1109/TAP.2004.834135.

[74] J. Kim and Y. Rahmat-Samii, "Implanted antennas inside a human body: Simulations, designs, and characterizations," *IEEE Trans Microw Theory Tech*, vol. 52, no. 8 II, 2004, doi: 10.1109/TMTT.2004.832018.

[75] K. S. Yee, D. Ingham, and K. Shlager, "Time-Domain Extrapolation to the Far Field Based on FDTD Calculations," *IEEE Trans Antennas Propag*, vol. 39, no. 3, 1991, doi: 10.1109/8.76342.

[76] S. D. Gedney, "An anisotropie perfectly matched layer-absorbing medium for the truncation of FDTD lattices," *IEEE Trans Antennas Propag*, vol. 44, no. 12, 1996, doi: 10.1109/8.546249.

[77] M. N. Ruiz-Cabello, M. Abaļenkovs, L. M. Diaz Angulo, C. C. Sanchez, F. Moglie, and S. G. Garcia, "Performance of parallel FDTD method for shared- And distributed-memory architectures: Application tobioelectromagnetics," *PLoS One*, vol. 15, no. 9 September, 2020, doi: 10.1371/journal.pone.0238115.

[78] W. Yu, R. Mittra, X. Yang, Y. Liu, Q. Rao, and A. Muto, "High-performance conformal FDTD techniques," *IEEE Microw Mag*, vol. 11, no. 4, pp. 42–55, Jun. 2010, doi: 10.1109/MMM.2010.936496.

[79] W. K. Liu, K. W. Tay, S. C. Kuo, and M. J. Wu, "Fabrication of piezoelectric AlN thin film for FBARs," *Science in China, Series G: Physics, Mechanics and Astronomy*, vol. 52, no. 2, 2009, doi: 10.1007/s11433-009-0021-5.

[80] R. K. Choudhary, P. Mishra, A. Biswas, and A. C. Bidaye, "Structural and Optical Properties of Aluminum Nitride Thin Films Deposited by Pulsed DC Magnetron Sputtering," *ISRN Materials Science*, vol. 2013, 2013, doi: 10.1155/2013/759462.

[81] I. Marasco *et al.*, "A compact evolved antenna for 5G communications," *Sci Rep*, vol. 12, no. 1, Dec. 2022, doi: 10.1038/s41598-022-14447-9.

[82] I. Marasco *et al.*, "Design and fabrication of a plastic-free antenna on a sustainable chitosan substrate," *IEEE Electron Device Letters*, 2022, doi: 10.1109/LED.2022.3232986.

[83] I. Marasco, G. Niro, F. Rizzi, M. de Vittorio, A. D'Orazio, and M. Grande, "Design of a PEN-Based flexible PIFA antenna operating in the sub-6GHz Band for 5G applications," in *International Conference on Transparent*

Optical Networks, 2020, vol. 2020-July. doi: 10.1109/ICTON51198.2020.9203160.

[84] Y. C. Chen, "Modeling of thin film bulk acoustic wave resonators and ladder-type filter design," *Journal of Optoelectronics and Advanced Materials*, vol. 12, no. 9, 2010, doi: 10.1142/9789812770165_0037.

[85] G. Pillai, A. A. Zope, J. M. L. Tsai, and S. S. Li, "Design and Optimization of SHF Composite FBAR Resonators," *IEEE Trans Ultrason Ferroelectr Freq Control*, vol. 64, no. 12, 2017, doi: 10.1109/TUFFC.2017.2759811.

[86] N. Ashraf, Y. Mesbah, A. Emad, and H. Mostafa, "Enabling the 5G: Modelling and design of high Q film bulk acoustic wave resonator (FBAR) for high frequency applications," in *Proceedings - IEEE International Symposium on Circuits and Systems*, 2020, vol. 2020-October. doi: 10.1109/iscas45731.2020.9180652.

[87] R. Y. Vidana Morales, S. Ortega Cisneros, J. R. Camacho Perez, F. Sandoval Ibarra, and R. Casas Carrillo, "3D simulation-based acoustic wave resonator analysis and validation using novel finite element method software," *Sensors*, vol. 21, no. 8, 2021, doi: 10.3390/s21082715.

[88] J. le An, T. T. Liu, and Y. Gao, "FBAR filter structural parameters optimizing with deep-learning approach," in *Proceedings of the 2020 15th Symposium on Piezoelectricity, Acoustic Waves and Device Applications, SPAWDA 2020*, 2021. doi: 10.1109/SPAWDA51471.2021.9445561.

[89] L. García-Gancedo *et al.*, "Direct comparison of the gravimetric responsivities of ZnO-based FBARs and SMRs," *Sens Actuators B Chem*, 2013, doi: 10.1016/j.snb.2013.03.085.

[90] Y. R. Kang, S. C. Kang, K. K. Paek, Y. K. Kim, S. W. Kim, and B. K. Ju, "Air-gap type film bulk acoustic resonator using flexible thin substrate," *Sens Actuators A Phys*, vol. 117, no. 1, 2005, doi: 10.1016/j.sna.2004.05.035.

[91] G. Naik, J. M. Park, J. Ashdown, and W. Lehr, "Next Generation Wi-Fi and 5G NR-U in the 6 GHz Bands: Opportunities and Challenges," *IEEE Access*, vol. 8, 2020, doi: 10.1109/ACCESS.2020.3016036.

[92] Ó. Menéndez, P. de Paco, R. Villarino, and J. Parrón, "Closed-form expressions for the design of ladder-type FBAR filters," *IEEE Microwave and Wireless Components Letters*, vol. 16, no. 12, 2006, doi: 10.1109/LMWC.2006.885610.

[93] Ó. Menéndez, P. De Paco, R. Villarino, and J. Parrón, "Closed-form expressions for the design of ladder-type FBAR filters," *IEEE Microwave and Wireless Components Letters*, 2006, doi: 10.1109/LMWC.2006.885610.

[94] N. I. M. Nor, N. Khalid, R. A. M. Osman, and Z. Sauli, "Estimation of material damping coefficients of aln for film bulk acoustic wave resonator,"

in *Materials Science Forum*, 2015. doi: 10.4028/www.scientific.net/MSF.819.209.

[95] R. K. Thalhammer and J. D. Larson, "Finite-Element Analysis of Bulk-Acoustic-Wave Devices: A Review of Model Setup and Applications," *IEEE Transactions on Ultrasonics, Ferroelectrics, and Frequency Control*. 2016. doi: 10.1109/TUFFC.2016.2555306.

[96] D. M. Pozar, *Microwave Engineering, 4th Edition*. 2012.

[97] T. Y. Lee and J. T. Song, "Detection of carcinoembryonic antigen using AlN FBAR," in *Thin Solid Films*, 2010, vol. 518, no. 22. doi: 10.1016/j.tsf.2010.03.060.

[98] D. Zheng, J. Xiong, P. Guo, S. Wang, and H. Gu, "AlN-based film buck acoustic resonator operated in shear mode for detection of carcinoembryonic antigens," *RSC Adv*, vol. 6, no. 6, 2016, doi: 10.1039/c5ra21900k.

[99] C. Zhou *et al.*, "Flexible structured high-frequency film bulk acoustic resonator for flexible wireless electronics," *Journal of Micromechanics and Microengineering*, vol. 25, no. 5, 2015, doi: 10.1088/0960-1317/25/5/055003.

[100] H. Kou, Q. Tan, Y. Wang, G. Zhang, S. Shujing, and J. Xiong, "A microwave SIW sensor loaded with CSRR for wireless pressure detection in high-temperature environments," *J Phys D Appl Phys*, vol. 53, no. 8, 2020, doi: 10.1088/1361-6463/ab58f2.

[101] T. Yun and S. Lim, "High-Q and miniaturized complementary split ring resonator-loaded substrate integrated waveguide microwave sensor for crack detection in metallic materials," *Sens Actuators A Phys*, vol. 214, 2014, doi: 10.1016/j.sna.2014.04.006.

[102] J. G. D. Oliveira, E. N. M. G. Pinto, V. P. S. Neto, and A. G. D'assunção, "CSRR-based microwave sensor for dielectric materials characterization applied to soil water content determination," *Sensors (Switzerland)*, vol. 20, no. 1, 2020, doi: 10.3390/s20010255.

[103] A. Javed, A. Arif, M. Zubair, M. Q. Mehmood, and K. Riaz, "A Low-Cost Multiple Complementary Split-Ring Resonator-Based Microwave Sensor for Contactless Dielectric Characterization of Liquids," *IEEE Sens J*, vol. 20, no. 19, 2020, doi: 10.1109/JSEN.2020.2998004.

[104] J. Muñoz-Enano, P. Vélez, M. Gil, and F. Martín, "Planar microwave resonant sensors: A review and recent developments," *Applied Sciences (Switzerland)*, vol. 10, no. 7, 2020, doi: 10.3390/app10072615.

[105] M. Abdolrazzaghi, M. Daneshmand, and A. K. Iyer, "Strongly Enhanced Sensitivity in Planar Microwave Sensors Based on Metamaterial Coupling," *IEEE Trans Microw Theory Tech*, vol. 66, no. 4, 2018, doi: 10.1109/TMTT.2018.2791942.

[106] Y. M. Wei, X. G. Guo, L. Chen, and Y. M. Zhu, "A novel coplanar waveguide resonator on flexible substrate," *Optik (Stuttg)*, vol. 127, no. 20, 2016, doi: 10.1016/j.ijleo.2016.07.095.

[107] M. E. B. Jalil *et al.*, "High Capacity and Miniaturized Flexible Chipless RFID Tag Using Modified Complementary Split Ring Resonator," *IEEE Access*, vol. 9, 2021, doi: 10.1109/ACCESS.2021.3061792.

[108] L. Atzori, A. Iera, and G. Morabito, "The Internet of Things: A survey," *Computer Networks*, vol. 54, no. 15, 2010, doi: 10.1016/j.comnet.2010.05.010.

[109] J. G. Andrews *et al.*, "What will 5G be?," *IEEE Journal on Selected Areas in Communications*, vol. 32, no. 6, pp. 1065–1082, 2014, doi: 10.1109/JSAC.2014.2328098.

[110] T. Meissner and F. J. Wentz, "The complex dielectric constant of pure and sea water from microwave satellite observations," *IEEE Transactions on Geoscience and Remote Sensing*, vol. 42, no. 9, 2004, doi: 10.1109/TGRS.2004.831888.